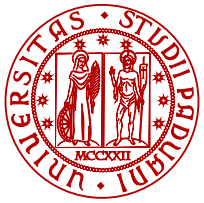

UNIVERSITÀ
DEGLI STUDI
DI PADOVA

Sede amministrativa: Università degli Studi di Padova

Dipartimento di Tecnica e Gestione dei Sistemi Industriali

---

SCUOLA DI DOTTORATO DI RICERCA IN INGEGNERIA MECCATRONICA E DELL'INNOVAZIONE MECCANICA DEL PRODOTTO
CICLO XXVIII

# STATE ESTIMATION IN MULTIBODY SYSTEMS WITH RIGID OR FLEXIBLE LINKS

**Direttore della scuola:** Ch.mo Prof. Alessandro Persona

**Supervisore:** Ch.mo Prof. Alberto Trevisani

**Dottoranda:** Ilaria Palomba

## Sommario

Nello studio e nella progettazione di meccanismi e manipolatori (comunemente detti sistemi multibody MB) la sintesi di stimatori dello stato diviene un requisito indispensabile in molteplici applicazioni avanzate, quali ad esempio la fault detection, l'identificazione dei parametri, la sintesi di controllori, o il controllo attivo delle vibrazioni. Gli stimatori dello stato sono progettati per ottenere delle accurate stime di variabili non misurabili o non misurate. Le prestazioni di uno stimatore dipendono tanto dalla scelta di un opportuno algoritmo di stima, che deve essere capace di fronteggiare le nonlinearità dei sistemi MB, quanto dalla modellazione adottata per i sistemi stessi. In particolare, quest'ultima deve essere adatta al processo di stima, nel senso che deve fornire una descrizione accurata del sistema fisico ma al contempo essere efficiente computazionalmente.

Al fine di ottimizzare le prestazioni degli stimatori sono stati sviluppati degli approcci di stima diversificati per i sistemi MB a membri rigidi ed a membri flessibili.

In riferimento ai sistemi MB a membri rigidi è stato sviluppato un approccio di stima che rafforza significativamente il ruolo delle equazioni di chiusura cinematiche. Infatti esse, rispetto ai modelli dinamici sino ad ora ampiamente utilizzati, presentano alcuni vantaggi tra cui la minore complessità ed incertezza. Questo nuovo approccio permette non solo di ottenere stime dello stato più accurate ma anche di affrontare con successo il problema della stima delle forze incognite attraverso una formulazione del tutto innovativa, chiamata approccio a due stadi ("two-stage approach").

Per quanto concerne la modellazione dei sistemi MB a membri flessibili, essa presenta criticità alquanto diverse dal precedente ambito di indagine, tra cui la difficoltà di disaccoppiare l'analisi cinematica da quella dinamica, che impedisce l'adozione di un approccio cinematico per la stima delle variabili di stato, e le elevate dimensioni dei modelli che usualmente non permettono la sintesi di stimatori computazionalmente efficienti. Tali criticità hanno imposto preliminarmente lo sviluppo di una nuova strategia per la riduzione dei modelli dinamici non lineari configurazione-varianti dei sistemi MB a membri flessibili. Questa nuova strategia di riduzione permette di ottenere dei modelli dinamici di dimensioni significativamente ridotte, ma ugualmente capaci di descrivere accuratamente la dinamica dei sistemi MB a membri flessibili in un intervallo di frequenze d'interesse. La disponibilità di tali modelli ridotti ha reso possibile la successiva implementazione di più efficienti stimatori dello stato anche nonlineari.

Nel presente lavoro di tesi sono inoltre raccolti i numerosi risultati derivanti da test sia numerici che sperimentali condotti per dimostrare la validità degli sviluppi teorici discussi.

**Abstract**

In the multibody field the design of state observers proves useful for several tasks, ranging from the synthesis of control schemes and fault detection strategies, to the identification of uncertain parameters. State observers are designed to obtain accurate estimates of unmeasurable or unmeasured variables. Their accuracy and performance depend on both the estimation algorithms and the system models. Indeed, on the one hand the estimation algorithms should be able to cope with multibody system (MBS) nonlinearities. On the other, MB models should be suitable to state estimation, i.e. accurate and computationally efficient. In order to obtain the best results, it has been necessary to develop different approaches for rigid-link and flexible-link MBSs.

In the case of rigid-link MBSs, state observers based on nonlinear kinematic models (i.e. kinematic constraint equations) have been developed. When compared to dynamic models, kinematic models present some relevant advantages. In particular, they are less complex and much less affected by uncertainty. Additionally, though kinematics-based observers do not require force and torque measurements (often difficult to gather) as inputs, they can be successfully employed for estimating unknown forces: to this purpose a novel "two-stage approach" is proposed in this dissertation.

As far as modeling flexible-link MBSs is concerned, it is more complicated and makes the implementation of kinematics-based observers impossible, since it is not possible to decouple kinematics from dynamics easily. Furthermore, the so called "fine motion" of such systems is typically described through a large number of elastic coordinates, which in turns leads to high model dimensions, and to very inefficient, if not impossible to synthesize, state observers. In order to address this issue, firstly, a new strategy has been developed to keep model dimensions to a minimum. Such a strategy leads to a significant reduction in the size of the models, which, in turns, provide an appropriate representation of the system dynamics in a frequency range of interest. The availability of reduced-dimension but accurate models for flexible-link MBSs poses the way to the synthesis of more efficient observers provided that a suitable estimation algorithm is chosen.

This thesis also collects results from a large number of numerical and experimental tests carried out to validate the intermediate and final outcomes of the theoretical investigations.

**Aknowledgements**

Caius Titus said: “verba volant scripta manent”
I hope that my thanks reach all the people who contributed in some form to the achievement of such challenging but rewarding goal.

First of all I would like to thank the person who invited me to take up this path three years ago, my supervisor Professor Alberto Trevisani. Thanks for your time, patience, guidance, immense knowledge, but especially for allowing me to learn and to grow up daily, and sorry for all the trains you lost meanwhile. Similar, profound gratitude goes to Professor Dario Richiedei, who has provided me an inestimable academic and human support. I owe you more than some beers. I would also like to thank all the professors of the Doctoral School for providing a congenial and stimulating academic environment. I would like to extend thanks to Professor Javier Cuadrado, as well as the whole research team of the Laboratorio de Ingenieria Meccanica for the hospitality and the fruitful collaboration. Special mention goes to all my adventure/misadventure mates Davide, Fabio, Luca, Pask , Roberto, Roberto, Tony, Vivis, for the stimulating discussions and for all the fun we have had during these years. I would like to thank the rest of the people who surround me in Lab and all my wonderful friends (of whom there are simply too many to mention by name). Thanks go to mum, dad, Pamela e Manuel for encouragement, help and support. A huge thanks to Fabio, who makes me happy. Finally, I thank that this thesis is finished, now I can sleep!

# Contents

# Chapter 1

# Introduction

This chapter introduces the motivations that gave rise to this thesis. After this, a compact literature overview of state estimation in multibody ststems (MBSs) is given. Finally, the objectives of this dissertation as well as an overview of the thesis itself are provided.

## 1.1 Motivations

The state of a dynamic system is the smallest set of independent variables (called state variables) whose knowledge together with the knowledge of the system inputs completely determines the behavior of a system at any time. Therefore, the state variables allow knowing the future response of a system, given the present state, the inputs, and the equations describing the system dynamics.

In MBSs the state variables are represented by kinematic quantities, in particular by positions and velocities in a number equal to the system degrees of freedom (dofs). For example, the state of a slider crank mechanism, which is a single dof system, is formed by one position and one velocity as shown in Fig. 1.1.

Not only is the knowledge of the actual state of a MBS an essential requirement for assuring proper motion through advanced control schemes [1], but it is also useful in the implementation of techniques for fault detection [2, 3], virtual sensors [4] and of strategies for the identification of uncertain parameters [5–7].

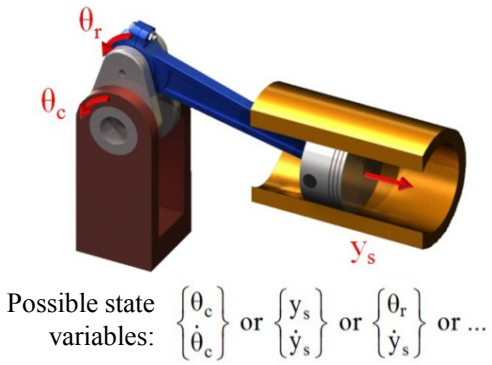


Figure 1.1: Example of state and state variables of a MBS

Unfortunately, the direct measurement of all the state variables is frequently unfeasible for technical or economical reasons. Therefore, the availability of efficient and effective techniques for the estimation of state variables in MBS is often necessary.

As a basic approach to state estimation, one could use the dynamic equations of motion of a MBS to estimate the missing state variables, once the external forces (i.e. the model inputs) are known, by means of a simulation of the system response to the input. Such an approach provides correct estimates just in the unusual case of exact model knowledge and absence of measurement errors. Conversely, it is strongly affected by uncertainty in the model parameters and it does not filter sensor noise either.

Great improvements of the estimates can be achieved by designing closed-loop state observers (estimators) [8], which are based on both prediction and correction phases. An observer reconstructs the missing state variables by means of a reliable system model and of measurements of both the system inputs and outputs. In particular, the inputs to the model are all the inputs acting on or driving the physical system (i.e. also disturbance inputs acting on the system that are only characterisable in some general way), while the outputs of the model are signals in the system that are accessible for measurements. The fusion of system model and sensor measurements allows tackling very effectively a wide class of issues. On the one hand, the closed-loop architecture of a state observer provides a means to compensate for model parameter errors, due to, for example, bad calibration, modeling er-

rors, unexpected parameter changes. On the other, the use of a model, albeit uncertain, allows filtering external noise and hence avoiding the considerable delay that causal low-pass filters would introduce. Therefore, an observer is a mathematical tool aiming at mediating between model uncertainties and measurement errors to reconstruct the system state as accurately as possible.

Before discussing the aims of this thesis it is essential to go through the state of the art on state estimation applied to MBSs. After such an overview, the need for a novel research effort will be become clear.

## 1.2 State estimation: state of the art

The synthesis of state observers requires to model a MBS in state space formulation, so the model is composed of two equations, the system equation $\boldsymbol{f}_c$ and the observation equation $\boldsymbol{g}$:

$$\begin{cases} \dot{\mathbf{x}}(t) &= \boldsymbol{f}_c(\mathbf{x}(t), \mathbf{u}(t), \boldsymbol{\delta}(t)) \\ \mathbf{y}(t) &= \boldsymbol{g}(\mathbf{x}(t)), \boldsymbol{\delta}^{\mathrm{y}}(t)) \end{cases} \tag{1.1}$$

The first one is a set of first-order Ordinary Differential Equations (ODEs) describing how the state $\mathbf{x}$ propagates in the presence of external inputs $\mathbf{u}$, and unknown disturbances $\boldsymbol{\delta}$. As far as the observation equation $\boldsymbol{g}$ is concerned, it expresses the algebraic relation between the state and the output variables $\mathbf{y}$. In Eq. (1.1) $\boldsymbol{\delta}^{\mathrm{y}}$ is the vector of the measurement noise due, for instance, to sensor noise, bad calibration or misalignment.

In the MB field the use of discrete-time filters based on difference equations is usually preferred to continuous-time filters. Therefore, both the system and the observation equation in Eq. (1.1) are modeled as discrete-time processes:

$$\begin{cases} \mathbf{x}_k &= \boldsymbol{f}(\mathbf{x}_{k-1}, \mathbf{u}_{k-1}, \boldsymbol{\delta}_{k-1})) \\ \mathbf{y}_k &= \boldsymbol{g}(\mathbf{x}_k, \boldsymbol{\delta}_k^{\mathrm{y}}) \end{cases} \tag{1.2}$$

In Eq. (1.2) $k \in \mathbb{N}^+$ is the time step index, and $\boldsymbol{f}$ is the discrete-time state equation, which depends on both its continuous expression $\boldsymbol{f}_c$ and on the discretization scheme adopted. Obviously, also in this case process $\boldsymbol{\delta}_{k-1}$ and measurement $\boldsymbol{\delta}_k^{\mathrm{y}}$ noises are included in the model.

The inherent uncertainties of both the model and the measured quantities lead to address the estimation problem in a probabilistic way. As a consequence, the state variables should be considered stochastic variables and the estimation problem is formulated as a Bayesian estimation problem [9].

In order to solve the Bayesian estimation problem, approximate solutions are usually employed. In particular, the most widespread simplification is to assume that noise terms $\boldsymbol{\delta}$ and $\boldsymbol{\delta}^y$ are uncorrelated, Gaussian and white with zero mean: $E(\boldsymbol{\delta}\boldsymbol{\delta}^{\mathrm{yT}}) = 0$, $\boldsymbol{\delta} \in N(0, \mathbf{Q})$, $\boldsymbol{\delta}^{\mathrm{y}} \in N(0, \mathbf{R})$, where $\mathbf{Q}$ and $\mathbf{R}$ are covariance matrices of, respectively, the model and the measurement noises. This is one of the basic assumptions of Kalman filter (KF) [8], the other one is that the system state-space model in Eq. 1.1 is linear. Under the aforementioned assumptions the KF provides an optimal and exact solution to the Bayesian estimation problem.

Basically, the KF consists into two main phases: the prediction and the correction. In the prediction phase, the KF operates by propagating the mean and covariance of the state through time. It requires a mathematical description of the dynamic system whose state is to be estimated. Such a model together with the noisy input measurements is used to propagate the state mean and covariance. In particular, the mean is the Kalman filter "a-priori" estimate of the state, while the covariance is the "a-priori" covariance of the Kalman filter state estimate. Then, when the next observation measurements are available, the "a-priori" estimates are corrected by means of the error between the measured and the estimated output variables, weighed through the filter gain. Therefore, the final estimates include both the prediction based on the system model, and the closed-loop correction based on measurements.

Since its publication in 1960, the KF has had great success and spread, due to its ease of implementation and modest computational cost.

In order to apply Kalman framework to nonlinear systems too, the extended Kalman filter (EKF) was developed [10–12]. Basically the EKF requires to make another approximation, i.e. the linearization around the estimated state trajectory of the nonlinear model equations.

Although the solution provided by the EKF is neither exact nor optimal, due to the approximations, the EKF is by far the most used algorithm in

nonlinear estimation. Indeed, it has been applied in many engineering fields ranging from state estimation [13–17], to parameter estimation [5, 18], and dual estimation [19].

However, in the case of highly nonlinear systems, as MBSs are, the linearization introduced by the EKF and the related computation of Jacobian matrices can cause significant errors and sometimes may lead to filter instability too.

The aforementioned shortcomings of the EKF have lead to the development of other filters suitable to nonlinear state estimation: the central difference filter [20], the divided difference filter [21], and the unscented Kalman fiter [22–27]. Basically, all these filters still consider a Gaussian distribution for the stochastic variables, but they use some deterministic sampling methods for the propagation of Gaussian stochastic variables through nonlinear systems and hence for computing the state estimates. Although the aforementioned filters have been developed by different groups, they can be viewed as different implementations of the same general deterministic sampling framework, and are called sigma-point Kalman filters (SPKFs) [28, 29]. In [30] and [31] the so-called square-root version of the SPKFs has been derived, such a new formulation has some advantages over the others from the computation view point, indeed it allows a more efficient and stable filter implementation. Finally, the SPKFs estimate the state of a dynamic system without the need of any linearization, and, for the same computational cost, outperform the EKF in terms of state estimation accuracy and estimate consistency.

Up to now, the use of such a family of filters in the MB field has only been investigated marginally [13]. In order to overcome the limitations displayed by the application of the EKF to nonlinear state estimation, in this thesis the use of SPKFs to state estimation in MBSs has been investigated. In particular, among the SPKFs available in literature, the Spherical Simplex Unscented Kalman Filter (SS-UKF) [27] has been implemented.

In Sections 1.2.1 and 1.2.2 the main features of the EKF and SS-UKF, i.e. the filter adopted in this thesis for synthesizing nonlinear observers, are briefly recalled to provide a clearer comprehension of the main issues related to state estimation. For a more detailed discussion, the interest reader is

referred to the quoted literature. However, it should be noticed that the theory proposed in this dissertation is general, and that any other nonlinear KF formulation can be used.

### 1.2.1 EKF algorithms

The EKF is the simplest extension of KF to nonlinear state estimation. The general recursive schemes of the EKF is sketched in Fig. 1.2. In the diagram and in the theory developed hereafter, the hat indicates an estimated variable, and the superscript "-" indicates a model-based a-priori estimate.

EKF relies on the nonlinear system equation $\boldsymbol{f}$ and the measurement equations $\boldsymbol{g}$ to perform the state $\hat{\mathbf{x}}_k^-$ and the observation $\hat{\mathbf{y}}_k$ predictions (a-priori estimates). In contrast, it replaces the nonlinear model with its Jacobian matrices $\mathbf{F}_{k-1}$ (the state transition matrix) and $\mathbf{H}_k$ (the observation matrix), computed about the estimated state trajectory, in order to propagate the covariance matrix $\mathbf{P}_k$ of the estimated state, which is employed to compute the gain $\mathbf{K}_k$ of the filter correction.

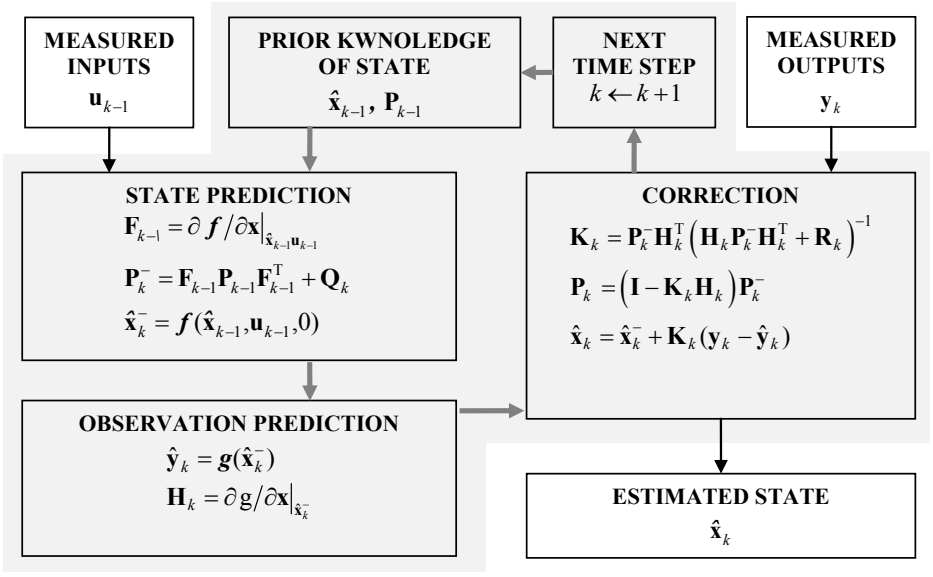


Figure 1.2: Discrete EKF recursive algorithm

Therefore, the EKF is not the optimal estimator for nonlinear systems, even in the presence of Gaussian noise, since it simply approximates the optimality of Bayes' rule through linearization. As a consequence, when model nonlinearities increase, the linearization may cause significant errors leading inaccurate estimates or even to filter instability.

### 1.2.2 SS-UKF algorithms

SS-UKF, and in general the SPKFs, calculate the statistics of a random variable undergoing a nonlinear transformation without the need of linearization.

As claimed in [22], the idea the SS-UKF is based on, is that it should be easier to approximate a Gaussian distribution than to approximate an arbitrary non linear function. In particular the Gaussian distribution of state

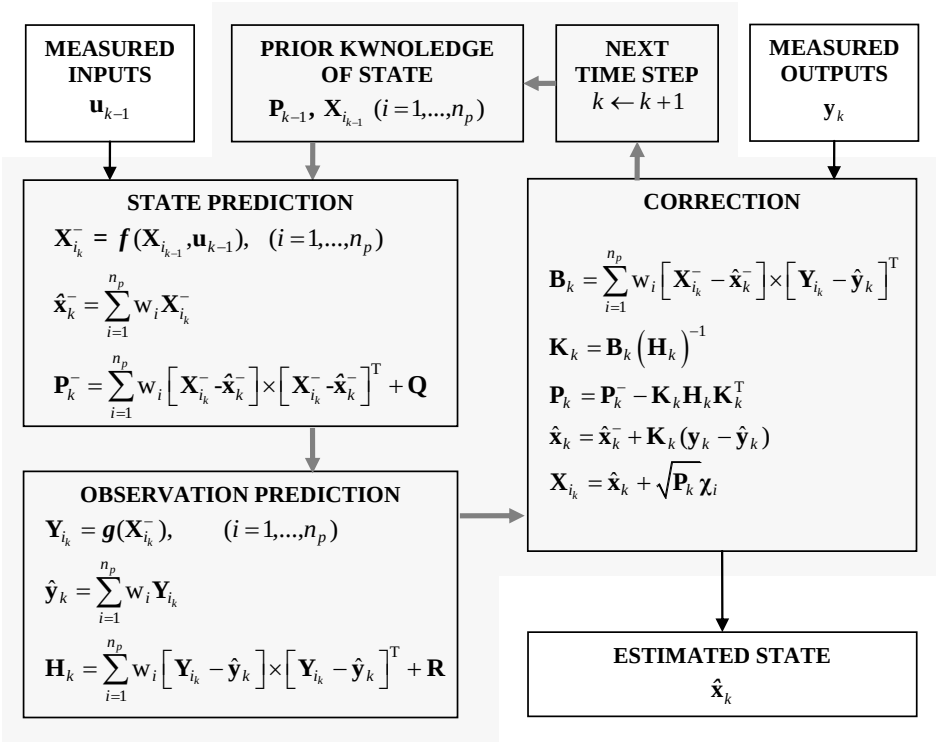


Figure 1.3: SS-UKF recursive algorithm

variables is approximated by means of a set of sample weighed points, called sigma points. These sigma points are chosen so as to capture completely the first two moments of a Gaussian distribution. In order to obtain the a-posteriori statistics of the random variables the sigma points are propagated through the actual nonlinear function; afterward, the transformed sigma points are used to approximate the desired Gaussian distribution with the same accuracy of, at least, the 3rd order Taylor' s series expansion (EKFs approximates the nonlinear system to the 1st order Taylor' s series expansion).

Any SPKF formulation starts by defining the matrix of the sigma points, in particular, with reference to the SS-UKF the sigma point matrix is defined as follows:

$$\mathbf{X}_i = \hat{\mathbf{x}} + \sqrt{\mathbf{P}}\boldsymbol{\chi}_i, \quad i = 1, \dots n+2 \tag{1.3}$$

where $\hat{\mathbf{x}}$ and $\mathbf{P}$ are respectively the mean and the covariance of the state, $n$ is the number of state variables and $\boldsymbol{\chi}_i$ is the $i^{\text{th}}$ column of the point selection matrix $\boldsymbol{\chi} \in \mathbb{R}^{n \text{x} n+2}$. The algorithm used by the SS-UKF for defining matrix $\boldsymbol{\chi}$ is the following one:

$$\text{for} \quad j = 2, \dots, n$$

$$\boldsymbol{\chi}_i^j = \begin{cases} \begin{bmatrix} \boldsymbol{\chi}_0^{j-1} \\ \mathbf{0} \end{bmatrix} & \text{for} \quad i = 0 \\ \begin{bmatrix} \boldsymbol{\chi}_i^{j-1} \\ -1/\sqrt{j(j+1)w_1} \end{bmatrix} & \text{for} \quad i = 1, \dots j \\ \begin{bmatrix} \mathbf{0}_{j-1} \\ 1/\sqrt{j(j+1)w_1} \end{bmatrix} & \text{for} \quad i = j+1 \end{cases} \tag{1.4}$$

where $w_1 = (1 - w_0)/(n+1)$ is the weight of all the sigma points except the zeroth sigma point, whose weight is $w_0$. Basically, $w_0$ is a user-defined parameter that affects the fourth and higher statistical moments of the sigma-point set ($0 \leq w_0 \leq 1$). The initial values to calculate the matrix in Eq. 1.4 are: $\boldsymbol{\chi}_0^1 = \mathbf{0}, \quad \boldsymbol{\chi}_1^1 = -1/\sqrt{2w_1}, \quad \boldsymbol{\chi}_2^1 = 1/\sqrt{2w_1}$. The SS-UKF computes the first

two moments (means $\hat{\mathbf{x}}_k^-, \hat{\mathbf{y}}_k$ and covariances $\mathbf{P}_k^-, \mathbf{H}_k$ ) of the a-priori estimates as the mean and the covariance of the weighed sigma points $\mathbf{X}_i$, which are propagated through the actual nonlinear state ($\mathbf{X}_{i_k}^- = \boldsymbol{f}(\mathbf{X}_{i_{k-1}}, \mathbf{u}_{i_{k-1}})$, $i = 1, \ldots, n_p$) and observation ($\mathbf{Y}_{i_k} = \boldsymbol{g}(\mathbf{X}_{i_k}^-)$, $i = 1, \ldots, n_p$) functions. Therefore, the SS-UKF calculates the statistics of random variables undergoing nonlinear transformations without the need of linearization. Such a feature makes the SS-UKF more suitable in case of significant nonlinearities.

The general recursive schemes of the SS-UKF is sketched in Fig. 1.3.

A comparison between the block diagrams of the two filters (Figs. 1.2 and 1.3) highlights that the correction stage is identical for both the filters. Indeed, in both the cases, the state prediction $\hat{\mathbf{x}}_k^-$, computed through the uncertain model $\boldsymbol{f}$ and the noisy input measurements $\mathbf{u}_{k-1}$, is corrected through the error between the output measurements and the output estimates ($\mathbf{y}_k - \hat{\mathbf{y}}_k$), also called innovation, weighed through the filter gain $\mathbf{K}_k$. The resulting a-posteriori estimate $\hat{\mathbf{x}}_k$ is therefore obtained as:

$$\hat{\mathbf{x}}_k = \hat{\mathbf{x}}_k^- + \mathbf{K}_k(\mathbf{y}_k - \hat{\mathbf{y}}_k) \tag{1.5}$$

Therefore, in both the EKF and the SS-UKF, the a-posteriori estimate $\hat{\mathbf{x}}_k$ includes both the prediction $\hat{\mathbf{x}}_k^-$ based on the system model, and the correction $\mathbf{K}_k(\mathbf{y}_k - \hat{\mathbf{y}}_k)$ based on measurements. What differs is the way in which $\hat{\mathbf{x}}_k^-$ and $\mathbf{K}_k$ are computed.

#### 1.2.2.1 Non-stochastic interpretation of KFs

Both the SS-UKF and the EKF, previously discussed, perform the so-called stochastic state estimation, and therefore require the knowledge of the zero-mean Gaussian noise covariance matrices $\mathbf{Q}$ and $\mathbf{R}$ to compute the filter gains. Since, in practice, noise is often non-Gaussian (in particular model noise, whose covariance is also difficult to evaluate), these filters can be also seen in a non-stochastic way by considering matrices $\mathbf{Q}$ and $\mathbf{R}$ as design parameters to be tuned for optimizing performances, rather than actual properties of the disturbance.

## 1.3 Research objectives and work overview

The main objective of the research described in this thesis is to synthesize state observers for MBSs with either rigid or flexible links and characterized by nonlinear dynamic models. Basically, state estimation can be effectively carried out if appropriate MB models and estimation algorithms are adopted.

The approach makes use of a model to predict the behavior of the system in a particular state, and then compares the behavior predicted with the actual one from the real system, in order to determine which state is the most likely to produce the observed system behavior. The determination of the most likely state can be more or less effective, depending on the estimation algorithm selected.

Both MB models and estimation algorithms play an essential role in obtaining state estimates with improved accuracy and real-time capability. Indeed, on the one hand estimation algorithms should cope with MBS nonlinearities and deliver accurate estimates. On the other, MBS models should be accurate in the sense that they must represent the system behavior correctly, and should be scarcely affected by uncertainties, since model uncertainty may seriously compromise the accuracy of the estimates and affect their practical usefulness. Additionally, they should be efficient from a computational viewpoint.

As far as algorithms are concerned, the goals of this dissertation are:

- To investigate the use of SPKFs in state estimation in MBSs.
- To test SPKFs both numerically and experimentally.
- To compare the performances of SPKFs with the ones of the more popular EKF.

As for modeling, the different features of MBSs with either rigid or flexible links have suggested to address the estimation problem by developing dedicated and specific approaches for the two kinds of systems.

When rigid-link MBSs are considered, it is worth underlining that the state of a MBS contains kinematic variables (i.e. positions and velocities) and that all the links of such a system satisfy the rigid-body constraint. This

implies that the kinematic analyses are independent of the dynamic ones, and that the kinematic state can be estimate through observers simply based on nonlinear kinematic constraint equations (or "kinematic models").

The use of kinematic models presents some relevant advantages, in particular, such models are less complex and much less affected by uncertainty than dynamic models, typically used for state estimation. Therefore, the use of kinematic models and of specifically selected and efficient observers capable to cope with the nonlinearities of kinematic models can greatly improve the accuracy of kinematic state estimation in rigid-link MBSs. Based on this evidence, the research aims at:

- Developing a new and comprehensive theory for kinematic state estimation in MBS with rigid links.
- Dealing with the "unknown inputs" problem, i.e. the case in which both the kinematic state and some of the forces acting on the system have to be estimated.
- Proving the soundness of the theory through numerical and experimental tests.

Modeling flexible-link MBSs is more complicated than rigid-link MBSs, and makes it impossible to implement observers based on kinematic models. Indeed, the kinematic equations of flexible-link MBSs are expressed as a sum of rigid displacements of a rigid-link reference mechanism and elastic displacements with respect to the aforementioned reference mechanism. Typically, both of them are not measurable. Furthermore, it is not possible to decouple the elastic displacements from the forces that have generated them. Hence, at least at the current level of knowledge, it is impossible to adopt a kinematic approach for estimating state variables in MBSs with flexible-links (although the state comprises just kinematic variables), and therefore the use of dynamic models is needed.

Currently, the main obstacle to the synthesis of efficient state observers for such systems are the large dimensions of the models. Indeed, the overall motion of a flexible-link MBS is described through some coordinates of the actuated degrees of freedom, which typically describe the system gross motion

(sometimes called rigid-body motion), and through several elastic coordinates (typically resulting from finite element modeling) that describe the system fine motion. The resulting models have high dimensions, and so they are not suitable to synthesize efficient state observers. But state observers are generally useful only if they can run in real-time, which is an ever-rising requirement.

Therefore, an essential preliminary step towards synthesizing state observers for flexible-link mechanisms is developing effective model reduction strategies which allow keeping to a minimum the size of the nonlinear dynamic model of a flexible-link MBS. A considerable effort has been devoted to achieve such a goal.

### 1.3.1 Thesis outline

The remainder of the dissertation is organized as follows:

Chapters 2 and 3 deal with state estimation in rigid-link MBSs, in particular

**Chapter 2** presents a new approach to estimate the state variables exploiting just kinematic constraint equations and measurements of kinematic quantities. The chapter proves the soundness of the proposed approach through numerical and experimental tests on both open-chain and closed-chain MBSs.

**Chapter 3** addresses the "unknown inputs"problem, i.e. the case in which both the state and some of the input forces are unknown and hence have to be estimated. The approach finalized to solve such a problem, called "two-stage" approach, is described in detail and validated.

The Chapters from 4 to 6 deal with state estimation in flexible-link MBSs, according to the following division:

**Chapter 4** is devoted to the modeling of flexible-link MBSs. First, an overview on the different MB formulations for such systems is provided, then the formulation based on the equivalent rigid-link system (ERLS) is described. The latter formulation is then applied straightforwardly to a rather complex example of flexible-link planar manipulator with hybrid topology.

The model is also refined by matching experimental and numerical modes (i.e. by a model updating technique).

**Chapter 5** focuses on the reduction of dynamic models. First an overview on reduction techniques is provided, then the Craig-Bampton (CB) method is recalled, and two novel ranking methods for the interior modes of the CB method are presented. Such ranking methods allow selecting the minimum number of interior modes needed to achieve a desired degree of accuracy of the reduced order model. Initially, the methods have been developed for and applied to linear systems, subsequently, it is shown that they can be successfully applied to MBS.

In **Chapter 6** the implementation of state observers for nonlinear flexible-link MBSs is finally discussed referring to the manipulator presented in Chapter 4. The observer is synthesized adopting a reduced order model obtained by applying the method suggested in Chapter 5.

**Chapter 7** summarizes the chief results achieved and draws the conclusions.

# Chapter 2

# State estimation in rigid-link multibody systems

Athough the interest is often confined to kinematic variables [32], the design of state observers in the multibody field, has been typically based on EKF employing dynamic equations of motion [13–15]. Such dynamic models depend on several uncertain geometric and inertial parameters (such as link dimensions, joint positions, actual mass and moments of inertia values, positions of centers of mass) and on unknown, and often difficult to measure external inputs (such as friction, control and disturbance forces). Therefore, the uncertainty of dynamic models may seriously compromise the accuracy and the convergence of observers, and hence affects their actual usefulness in practical applications. The impact of uncertainty on kinematic state estimates (i.e. typically, estimates of positions, velocities and accelerations) can be reduced considerably by only employing kinematic equations instead of dynamic models, and hence by measuring kinematic quantities and by. Indeed, if all the links of the system are rigid, and whenever joint clearance is negligible, nonlinear kinematic constraint equations can be employed instead of dynamic models to perform the estimation of the kinematic state. The advantage of employing kinematic constraint equations is that they are subject to a lower number of uncertain parameters compared to dynamic models. For instance, kinematic observers can be employed effectively regardless of the presence of joint friction, contrary to dynamic models which need accurate knowledge of such a phenomenon to provide accurate esti-

mates. Additionally, the parameters that might be uncertain in kinematic constraint equations are just of geometric nature, and therefore are usually much less affected by uncertainty.

State observers based on kinematic equations have already been proposed in literature [33,34] and are known as Kinematic Kalman Filters (KKFs). In its original definition, a KKF is a sensor-based estimator where the measurement set is used both as the output and the input to first-order differential equations representing the kinematic model of a system (i.e. the kinematic constraint equations). To the best of the author's knowledge, so far kinematic state observers have been employed just to perform simple encoder-accelerometer sensor fusion (without the use of kinematic constraints) in a single body system [34], or to perform end-effector sensing both in a planar two-link robot [33] and in an industrial open chain robot [35]. In [36] an observer based on kinematic equations has instead been used for kinematic parameter estimation in rigid body systems. However, it still lacks a comprehensive and general theory for kinematic state estimation, capable of dealing with both open-chain and closed-chain multibody systems, and explicitly addressing the problems of state derivative estimation, and estimation in singular configurations.

Therefore, the aim of this chapter is to introduce a general theory for the design of nonlinear discrete-time state observers based on kinematic equations, suitable for MBSs with rigid links and negligible joint clearance. The theory is general in the sense that it can be applied to both open-chain and closed-chain MBSs. The theory also addresses the problem of closed-loop state derivative estimation, which is not trivial when discrete observers are employed, and the problem of computing the estimates in the presence of model singularity, by taking advantage of a switching model. The chapter is set out as follows: Section 2.1 provides a general first-order (state-space) formulation of kinematic constraint equations, suitable for performing state estimation, and details the suggested estimation procedure. In Section 2.2 some open issues in kinematic estimation are discussed. In particular, state derivative estimation and state estimation in the presence of model singularity are discussed. Numerical and experimental tests on both closed-chain (1 dof) and open-chain (2 dofs) MBSs are presented in Section 2.3, to prove the

soundness of the proposed theory. Finally, concluding remarks are given in Section 2.4.

## 2.1 Kinematic modeling: State-space formulation

### 2.1.1 Kinematic constraint equations

The basic idea behind kinematic estimation is to exploit the kinematic constraint equations and a proper set of measurable kinematic variables in order to estimate other unmeasured kinematic variables. Let us consider an arbitrary open-chain or closed-chain MBS with rigid links, joints with no clearance and holonomic, scleronomous constraints, having $n$ degrees of freedom. In order to perform kinematic estimation, the system should be modeled through a suitable set of $n$ independent coordinates $\mathbf{z}$, and a set of $m$ dependent coordinates $\mathbf{h}$, to be measured at some order of derivative (as it will be discussed in Section 2.1.3). The following three sets of $m$ kinematic equations, respectively representing the position, velocity and acceleration constraints, can be hence defined:

$$\mathbf{h} = \mathbf{\Phi}(\mathbf{z}) \tag{2.1}$$

$$\dot{\mathbf{h}} = \mathbf{S}(\mathbf{z})\dot{\mathbf{z}} \tag{2.2}$$

$$\ddot{\mathbf{h}} = \mathbf{S}(\mathbf{z})\ddot{\mathbf{z}} + \dot{\mathbf{S}}(\mathbf{z}, \dot{\mathbf{z}})\dot{\mathbf{z}} \tag{2.3}$$

Matrices $\mathbf{S}$ and $\dot{\mathbf{S}}$ are respectively the sensitivity coefficient matrix and its time derivative. Equation 2.1 is a set of nonlinear equations in the variable $\mathbf{z}$, and does not depend explicitly on time in the case of scleronomous constraints.

### 2.1.2 Definition of the state and input vectors

In order to be useful to state estimation, the constraint equations 2.1, 2.2 and 2.3 must be reformulated as first-order ODEs to fit the model of Eq. 1.1. To this end, proper definitions of the state vector $\mathbf{x}$, the system measured input

vector $\mathbf{u}$, and the measured output vector $\mathbf{y}$ are crucial. Such definitions must ensure both model existence and the observability of the system model realization. As far as the state vector is concerned, its definition depends on the variables to be estimated. If the interest lies only in the estimates of the independent coordinates and their first derivatives (the independent velocities), the state vector should be defined as the following $n$-dimensional vector:

$$\mathbf{x} = \mathbf{z} \tag{2.4}$$

Conversely, if also the second derivatives of the independent coordinates are of interest for the estimation, the state vector is augmented to a $2n$-dimensional vector including both the independent coordinates and their first derivatives (see the methods for state-derivative estimation proposed in Section 2.2.1):

$$\mathbf{x} = \begin{Bmatrix} \mathbf{z}^{\mathrm{T}} & \dot{\mathbf{z}}^{\mathrm{T}} \end{Bmatrix}^{\mathrm{T}} \tag{2.5}$$

The definition provided in Eq. 2.5 should be also adopted whenever velocities are to be estimated through acceleration measurements, to be fused with position measurements.

As for the model input vector $\mathbf{u}$, it should include at least $n$ independent measured kinematic quantities having the same time-derivative order of the components of $\dot{\mathbf{x}}$ with the highest derivative order.

### 2.1.3 First-order model formulation

Once that the state and the input vector are defined, it is possible to develop the first-order ODEs representing the kinematic model of a MBS. In particular, in the case of state vector just including the independent coordinates, as in Eq. 2.4, the model is inferred from the velocity constraint equation 2.2:

$$\dot{\mathbf{x}} = \dot{\mathbf{z}} = [\mathbf{S}^{\mathrm{T}}(\mathbf{z})\mathbf{S}(\mathbf{z})]^{-1}\mathbf{S}^{\mathrm{T}}(\mathbf{z})\mathbf{u} \tag{2.6}$$

The model should be instead based on the acceleration constraint equation 2.3 whenever the state vector includes both the independent coordinates

and the independent velocities, as in Eq. 2.5:

$$\dot{\mathbf{x}} = \left\{ \begin{array}{c} \dot{\mathbf{z}} \\ \ddot{\mathbf{z}} \end{array} \right\} = \left\{ \begin{array}{c} \dot{\mathbf{z}} \\ \left[\mathbf{S}^{\mathrm{T}}(\mathbf{z})\mathbf{S}(\mathbf{z})\right]^{-1} \mathbf{S}^{\mathrm{T}}(\mathbf{z}) \left\{ \mathbf{u} - \dot{\mathbf{S}}(\mathbf{z}, \dot{\mathbf{z}})\dot{\mathbf{z}} \right\} \end{array} \right\} \tag{2.7}$$

In Eqs. 2.6 and 2.7 the model inputs $\mathbf{u}$ are, respectively, the $m$-dimensional vector of the sensed velocities $\mathbf{u} = \dot{\mathbf{h}}$, and the vector of the sensed accelerations $\mathbf{u} = \ddot{\mathbf{h}}$ ($m \geq n$, being $n$ the number of dofs).
It is worth noticing that, in kinematic estimation, the input variables $\dot{\mathbf{h}}$ or $\ddot{\mathbf{h}}$ play the same role as the forces (or torques) in the synthesis of "traditional" state observers based on dynamic models, where the input vector collects the external actuation and disturbance forces.

The models obtained in Eq. 2.6 and Eq. 2.7 clearly show that the choice of the system inputs affects the existence of the system model, since it sets the existence of matrix $[\mathbf{S}^{\mathrm{T}}(\mathbf{z})\mathbf{S}(\mathbf{z})]^{-1}$.

### 2.1.4 Definition of the output vector

In order to set the measurement equation $\boldsymbol{g}$, the output vector $\mathbf{y}$ should be defined by selecting a set of other additional measured variables with the same derivative order of the state vector. The number of the independent measured variables in $\mathbf{y}$ should be at least equal to the number of system dofs, $n$, in order to adequately correct each state variable during the correction phase (i.e. to ensure adequate system observability even in the presence of relevant uncertainty on the model and on the state initial estimates).

The concept of observability can be simplified as the issue of whether the state of a system, whose model is known, is uniquely determinable from its measured inputs and outputs, and the initial conditions [11].

The estimation error is therefore asymptotically stable if the system satisfies the observability condition and if the initial estimation error, as well as the disturbance noise terms, are small enough [37, 38]. Generally speaking, a set of sensors ensuring adequate observability, even in the presence of uncertain state initial conditions and of model noise, should include as many non-redundant position measurements as the number of dofs, since such measurements are able to capture the zero-frequency dynamics.

Finally, it is worth highlighting the different role played in the estimation process by the measured variables collected in $\mathbf{u}$ and those in $\mathbf{y}$. Indeed, the variables in $\mathbf{y}$ intervene in the correction phase by contributing to the filter innovation, which is the discrepancy between the measurements predicted through the nominal model and the actual ones (see Section 1.2). In contrast, the variables in $\mathbf{u}$ play a key role in allowing the correct model formulation and the existence of $[\mathbf{S}^{\mathrm{T}}(\mathbf{z})\mathbf{S}(\mathbf{z})]^{-1}$, without contributing to the filter innovation. They intervene in just the prediction phase.

From the considerations made so far it is apparent that at least $2n$ non-redundant measurements are collected in vectors $\mathbf{u}$ and $\mathbf{y}$, to properly perform state estimations in the prediction-correction way typical of the closed-loop observers here discussed. In Section 2.2.1 it will be shown that, by following the original approach here proposed, the same set of measurement allows performing also state derivative estimation.

### 2.1.5 Discrete-time representation

As previously discussed in Section 1.2, the use of discrete-time filtering is very common in practice. Therefore, the first-order ODE representation of the kinematic constraint equations stated in Eq. 2.6 or in Eq. 2.7, henceforth referred to as "the kinematic model ", should be modeled as a discrete-time process. A typical discrete-time general representation of the state-space model is shown in Eq. 1.2.

As far as the discretization scheme is concerned, most of the works appeared in the literature on state observers usually perform model discretization through the first-order Euler's method, since its implementation is straightforward and it usually requires small computational efforts.

In the case of MBSs, in order to handle the significant nonlinearities due to kinematic constraints, a great improvement can be obtained by adopting the single-step higher order numerical techniques developed for the numerical integration of the equations of motion [39]. Indeed, higher order methods usually allow improving accuracy and getting a larger region of absolute stability, even in the presence of a larger sample time.

The following is an adequately general expression which can be employed

to represent a discrete-time model, in the case of a wide number of both implicit (e.g. the trapezoidal rule) and explicit (e.g. Runge-Kutta) techniques, leading to similar expressions of the discrete state transition function $\boldsymbol{f}$ [39]:

$$\mathbf{x}_k = \mathbf{x}_{k-1} + \Delta t \sum_{i=1}^{\nu} \beta_i \kappa_i, \qquad \kappa_i = \boldsymbol{f}_c \left( \mathbf{x}_{k-1} + \Delta t \sum_{j=1}^{\nu} \lambda_{ij} \kappa_j, \mathbf{u}_{k-1} \right) \tag{2.8}$$

The parameters $\beta_i$, $\lambda_{ij}$ and $\nu$ are peculiar to the specific discretization scheme adopted. Yet, the approach to state estimation proposed in this dissertation does not imposes any specific discretization scheme, and therefore any other method leading to a model representation slightly different from the one in Eq. 2.8, can be adopted.

As for the discretization of the measurement equation $\boldsymbol{g}$, it does not represent a critical issue since $\boldsymbol{g}$ is an algebraic equation.

Once the models formulated in Eq. 2.6 or Eq. 2.7 are discretized as in Eq. 2.8 and the output vector is defined, the observer synthesis can be performed through the methods discussed in Section 1.2. The whole procedure discussed represents a general and consistent approach to state estimation of kinematic variables.

## 2.2 Critical issues

### 2.2.1 State derivative estimation with discrete-time observers

The use of discrete-time filters based on the model in Eq. 1.2 allows estimating the state of a MBS once the system model, the inputs, the outputs, and the initial state vector are known. Conversely, state derivative estimation with the prediction-correction scheme proposed in both Figs. 1.2 and 1.3 is less straightforward with discrete schemes. Indeed it imposes to include all the variables to be estimated within the state, and consequently to augment the set of the continuous-time first-order ODEs in Eq. 2.6 or Eq. 2.7 with some relations involving variables of a greater derivative order. For instance, if acceleration is to be estimated, and hence included in the state, the set

of first-order ODEs must be augmented with some relations involving also jerks. This implies that, at least theoretically, jerk should be measured and included within the system input vector.This is clearly unfeasible.

Alternatively, discrete-time state derivative estimations involving acceleration can be computed through open-loop estimation with no prediction-correction iterations, either by means of numerical derivatives of the state variables or by means of the solution of the acceleration kinematic constraint equations. Since no correction is performed, such approaches may be inaccurate because they are affected, respectively, by sensor noise and model uncertainty.

In order to perform accurate discrete-time closed-loop state derivative estimations with the prediction-correction iterations, the equations representing the state derivative should be included in the state transition function $\boldsymbol{f}$, so that the correction $\mathbf{K}_{k|k}(\mathbf{y}_k^{meas} - \hat{\mathbf{y}}_{k|k-1})$ is applied to compensate for measurement noise or model uncertainty. To this purpose, this Section proposes three alternative approaches, which embed the state derivative equations into the state transition function. In particular, the first approach includes the kinematic constraint equations in $\boldsymbol{f}$ and is therefore suitable in the case of noisy measurements that do not allow effective numerical derivative without introducing delay due to low-pass causal filters. Conversely, the second approach is chiefly based on numerical derivatives, whose scheme is however included into $\boldsymbol{f}$: it is suggested in the presence of considerable model uncertainty. Finally, the third approach combines the advantages of the previous ones, at the cost of a slight increase in the model formulation complexity.

It is worth underlying that the issue of state derivative estimation is of particular interest in the case of acceleration estimation. Indeed, whenever speed estimation is to be performed, it is generally convenient performing acceleration measurements by including speed in the state and in accordance with Eqs. 2.5 and 2.7. In the following theoretical developments it is therefore assumed that acceleration estimation is to be performed without jerk measurements (see Sections 2.2.1.1, 2.2.1.2, 2.2.1.3). Nonetheless, the extension to speed estimation without acceleration measurement, in accordance with Eqs. 2.4 and 2.6, is straightforward.

#### 2.2.1.1 Kinematic equations with random walk

The kinematic constraints are algebraic equations and therefore are not suitable to be employed in the observer model straightforwardly. To overcome this limitation, acceleration is modeled through a so called "random walk":

$$\ddot{\mathbf{z}}_k = \ddot{\mathbf{z}}_{k-1} + \delta_{k-1} \tag{2.9}$$

where $\delta_{k-1}$ is the noise vector, representing the uncertainty on this equation, usually assumed as white noise. Basically, this approach assumes that the current value of the acceleration vector $\ddot{\mathbf{z}}_k$ is equal to the previous one $\ddot{\mathbf{z}}_{k-1}$ plus a noise terms $\delta_{k-1}$. The use of random walk is a trick often adopted for approximating the model of unknown, or highly uncertain, dynamics. Equation 2.9 can be rewritten making explicit the constraint equations:

$$\ddot{\mathbf{z}}_k = [\mathbf{S}_{k-1}^{\mathrm{T}}\mathbf{S}_{k-1}]^{-1}\mathbf{S}_{k-1}^{\mathrm{T}}\{\ddot{\mathbf{h}}_{k-1} - \dot{\mathbf{S}}_{k-1}\dot{\mathbf{z}}_{k-1}\} + \delta_{k-1} \tag{2.10}$$

This approach casts the kinematic constraint equations as first-order difference equations, by taking also advantage of the probabilistic nature of the state observer. The system model adopted in the estimation of the augmented state $\mathbf{x}^{aug} = \left\{\mathbf{x}^{\mathrm{T}} \quad \ddot{\mathbf{z}}^{\mathrm{T}}\right\}^{\mathrm{T}}$ is therefore represented through the following system of equations, originated from Eqs. 2.7 and 2.10:

$$\mathbf{x}_k^{aug} = \left\{ \begin{array}{c} \mathbf{x}_k \\ \ddot{\mathbf{z}}_k \end{array} \right\} =$$

$$\left\{ \begin{array}{c} \boldsymbol{f}(\mathbf{x}_{k-1}, \ddot{\mathbf{h}}_{k-1}) \\ \left[\mathbf{S}_{k-1}^{\mathrm{T}}\mathbf{S}_{k-1}\right]^{-1}\mathbf{S}_{k-1}^{\mathrm{T}}\{\ddot{\mathbf{h}}_{k-1} - \dot{\mathbf{S}}_{k-1}\dot{\mathbf{z}}_{k-1}\} \end{array} \right\} = \boldsymbol{f}_{aug}(\mathbf{x}_{k-1}^{aug}, \ddot{\mathbf{h}}_{k-1}) \tag{2.11}$$

#### 2.2.1.2 Numerical derivative with model uncertainty

An alternative approach to acceleration estimation embeds in the system model a set of first-order difference equations representing the numerical derivation, in the presence of noise $\delta_k$:

$$\ddot{\mathbf{z}}_k = \boldsymbol{\Psi}(\dot{\mathbf{z}}_k, \mathbf{z}_k, \ddot{\mathbf{z}}_{k-1}, \dot{\mathbf{z}}_{k-1}, \mathbf{z}_{k-1}) + \delta_{k-1} \tag{2.12}$$

The estimation of the augmented state $\mathbf{x}^{aug} = \left\{ \mathbf{x}^{\mathrm{T}} \quad \ddot{\mathbf{z}}^{\mathrm{T}} \right\}^{\mathrm{T}}$ is therefore performed through the following model:

$$\left\{ \begin{array}{c} \mathbf{I}\mathbf{x}_k \\ \boldsymbol{\Psi}_l(\mathbf{x}_k, \ddot{\mathbf{z}}_k) \end{array} \right\} = \left\{ \begin{array}{c} \boldsymbol{f}(\mathbf{x}_{k-1}, \mathbf{u}_{k-1}) \\ \boldsymbol{\Psi}_r(\mathbf{x}_{k-1}, \ddot{\mathbf{z}}_{k-1}) \end{array} \right\} = \boldsymbol{f}_{aug}(\mathbf{x}_{k-1}^{aug}, \mathbf{u}_{k-1}) \tag{2.13}$$

where $\mathbf{I}$ is the identity matrix, while functions $\boldsymbol{\Psi}_l$ and $\boldsymbol{\Psi}_r$ are obtained from $\boldsymbol{\Psi}$ by splitting the current state and the one at the previous time step $(k-1)$. Having introduced the numerical derivation scheme in the observer, the error due to measurement noise and to the approximate nature of numerical derivation is partially compensated by the closed-loop correction. Such a correction behaves as an optimal nonlinear filter whose gains, and therefore bandwidth, are updated at each time step depending on the estimation error and on noise, in accordance with the theory discussed in Section 1.2.

For instance, following a very popular approach in multibody system dynamics, the Newmark?s first-order interpolation method [39] can be employed as a derivative scheme for accelerations:

$$\ddot{\mathbf{z}}_k = \frac{1}{\beta \Delta t^2}(\mathbf{z}_k - \mathbf{z}_{k-1}) - \frac{1}{\beta \Delta t}\dot{\mathbf{z}}_{k-1} + \left(1 - \frac{1}{2\beta}\right)\ddot{\mathbf{z}}_{k-1} \tag{2.14}$$

or alternatively

$$\ddot{\mathbf{z}}_k = \frac{\dot{\mathbf{z}}_k - \dot{\mathbf{z}}_{k-1}}{\gamma \Delta t} + \frac{\gamma - 1}{\gamma}\ddot{\mathbf{z}}_{k-1} \tag{2.15}$$

In Eqs. 2.14 and 2.15, $\Delta t$ is the sample time adopted in the estimation (which can be different from the ones of sensor measurements in the case of multirate estimation). $\beta$ and $\gamma$ are positive parameters defining the derivation method.

Compared with the model-based method in Section 2.2.1.1, this approach is more effective in the presence of considerable model uncertainty, while it introduces high-frequency errors in the presence of noisy sensors. Nevertheless, the low-pass filtering due to the correction ensures that such high-frequency errors are smaller than the ones obtained through open-loop numerical derivatives.

#### 2.2.1.3 Kinematic equations with numerical derivative

A third approach is proposed in this thesis and is basically obtained by merging the two techniques presented above, in order to improve the overall estimation by reducing model uncertainty through kinematic modeling, a numerical derivative scheme, and the correction provided by the filter. The method consists in writing explicitly the state derivative at step $k-1$ (i.e. $\ddot{\mathbf{z}}_{k-1}$ in the acceleration estimation) through the kinematic constraint equations relating state, state derivative and inputs at time step $k-1$:

$$\ddot{\mathbf{z}}_{k-1} = [\mathbf{S}_{k-1}^{\mathrm{T}}\mathbf{S}_{k-1}]^{-1}\mathbf{S}_{k-1}^{\mathrm{T}}\{\ddot{\mathbf{h}}_{k-1} - \dot{\mathbf{S}}_{k-1}\dot{\mathbf{z}}_{k-1}\} \tag{2.16}$$

By taking advantage of the numerical derivative scheme in Eq. 2.15, the following set of equations augments the system model:

$$\ddot{\mathbf{z}}_k = \frac{\dot{\mathbf{z}}_k - \dot{\mathbf{z}}_{k-1}}{\gamma\Delta t} + \frac{\gamma-1}{\gamma}[\mathbf{S}_{k-1}^{\mathrm{T}}\mathbf{S}_{k-1}]^{-1}\mathbf{S}_{k-1}^{\mathrm{T}}\{\mathbf{u}_{k-1} - \dot{\mathbf{S}}_{k-1}\dot{\mathbf{z}}_{k-1}\} + \delta_{k-1} \tag{2.17}$$

For instance, if the EKF is employed for the estimation, and the Newmark's method is adopted, the accelerations are estimated as follows (the hat denotes the estimated values):

$$\hat{\ddot{\mathbf{z}}}_k = \frac{\hat{\dot{\mathbf{z}}}_k - \hat{\dot{\mathbf{z}}}_{k-1}}{\gamma\Delta t} + \frac{\gamma-1}{\gamma}[\mathbf{S}_{k-1}^{\mathrm{T}}\mathbf{S}_{k-1}]^{-1}\mathbf{S}_{k-1}^{\mathrm{T}}\{\mathbf{u}_{k-1} - \dot{\mathbf{S}}_{k-1}\hat{\dot{\mathbf{z}}}_{k-1}\} + \mathbf{K}_{k|k}(\mathbf{y}_k - \hat{\mathbf{y}}_{k|k-1}) \tag{2.18}$$

### 2.2.2 Estimation in the presence of model singularity

In Section 2.1.2, the importance of a proper definition of the system inputs has been discussed, since the existence of matrix $[\mathbf{S}^{\mathrm{T}}(\mathbf{z})\mathbf{S}(\mathbf{z})]^{-1}$ depends on the choice of such variables. Indeed, the set of input variables may lead to some configurations where matrix $[\mathbf{S}^{\mathrm{T}}(\mathbf{z})\mathbf{S}(\mathbf{z})]$ is singular, and therefore the system model in Eq. 2.7, (explicitly representing $\dot{\mathbf{x}}$ as a function of $\mathbf{u}$) cannot be formulated. These configurations will be hereafter denoted as "model singularities". In practice, the system input cannot be employed to reconstruct the state variables in these configurations.

Although a good selection of the sensor position and the use of sensor redundancy allows solving this occurrence, a solution based on the use of a

switching model is proposed in this work to overcome this issue whenever the definition of the input vector is restricted by technical or economical constraints.

Switching models are widely and effectively employed in control theory to approximate more complicate models in the synthesis of controllers or estimators (see e.g. [1]). In particular, whenever the system is in the neighborhood of a singular configuration, the kinematic model based on the constraint equations is switched to a random walk model with Gaussian noise, which provides an approximation of the actual one. Let $\Omega_s$ be the set of the singular configurations,

$$\Omega_s(\mathbf{z}) = \left\{\mathbf{z} | \det\left(\mathbf{S}^{\mathrm{T}}\mathbf{S}\right) = 0\right\} \tag{2.19}$$

and let $\Omega$ be a set including $\Omega_s$ ($\Omega_s \subset \Omega$) which represents the so-called switching rule, then the following first-order discrete switching model is defined:

$$\mathbf{x}_k = \begin{cases} \boldsymbol{f}(\mathbf{x}_{k-1}, \mathbf{u}_{k-1}, \mathbf{v}_{k-1}) & \text{if} \quad \mathbf{z}_{k-1} \notin \Omega \\ \mathbf{x}_{k-1} + \delta_{k-1} & \text{if} \quad \mathbf{z}_{k-1} \in \Omega \end{cases} \tag{2.20}$$

By taking advantage of the representation in Eq. 2.8, Eq. 2.20 can be also written as follows, to provide a clearer sample representation of the switching model:

$$\mathbf{x}_k = \begin{cases} \mathbf{x}_{k-1} + \Delta t \sum_{i=1}^{\nu} \beta_i \kappa_i + \mathbf{v}_{k-1} & \text{if} \quad \mathbf{z}_{k-1} \notin \Omega \\ \mathbf{x}_{k-1} + \delta_{k-1} & \text{if} \quad \mathbf{z}_{k-1} \in \Omega \end{cases} \tag{2.21}$$

The simplest choice for $\Omega$ is to define it as just a function of the position,

$$\Omega(\mathbf{z}) = \left\{\mathbf{z} | \det\left(\mathbf{S}^{\mathrm{T}}\mathbf{S}\right) \leq \epsilon\right\} \tag{2.22}$$

where $\epsilon$ is a suitably small threshold, usually approaching zero. More effectively, in order to prevent chattering and instability by operating in the slow switching condition, hysteresis can be employed in the switching rule by means of a redefinition of $\Omega$ as a function of both position and speed ($\Omega(\mathbf{z}, \dot{\mathbf{z}})$).

## 2.3 Numerical and experimental results

Two tests are proposed to prove the effectiveness of the theory developed. The first test is numerical and involves a single-dof, closed-chain, planar mechanism (slider-crank mechanism). The second one is experimental: the estimation approach proposed is applied to an open chain, two-dof, two-link, planar mechanism.

### 2.3.1 Test case I: slider-crank mechanism

The kinematic scheme of the slider-crank mechanism adopted in the first test case is shown in Fig. 2.1. The aim of the test is estimating the angular velocity and acceleration of the crank, as it is often useful in practice, since feedback motion controllers often require precise knowledge of speed and acceleration in order to ensure high bandwidth control.

Indeed, when no estimator is implemented, angular velocities and accelerations are computed by numerical derivatives and low pass filtering. However this approach introduces a phase-lag that reduces the controlled system phase margin and therefore downgrades the bandwidth considerably. Synthesizing an estimator following the proposed approach can greatly improve controller

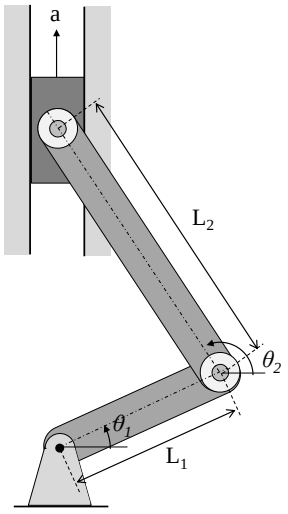


Figure 2.1: kinematic scheme of a slider-crank mechanism

performances.

The augmented state vector is defined as $\mathbf{x}^{aug} = \left\{\theta_1 \quad \dot{\theta}_1 \quad \ddot{\theta}_1\right\}^{\mathrm{T}}$, where $\theta_1$ is the crank rotation. The system is supposed to be equipped with an incremental encoder and a mono-axial accelerometer, measuring respectively the crank angular position $\theta_1$ and the slider linear acceleration a. The measured acceleration (a) is the system input for the estimation: u = a. The encoder measurement is instead the measured output: y = $\theta_1$.

As far as the system model is concerned, a switching model is adopted in order to yield estimates even close to the model singular configuration, which is encountered whenever the crank is aligned to the connecting link, i.e. $\Omega_s = \{\theta_1 | \theta_1 = \theta_2 + k\pi\}, \quad k \in \mathbb{N}$. The resulting state-space model takes the following form, if discretized through the first-order Euler's method:

$$
\begin{aligned}
&\mathbf{x}_k^{aug} = \begin{Bmatrix} \theta_{1_k} \\ \dot{\theta}_{1_k} \\ \ddot{\theta}_{1_k} \end{Bmatrix} = \\
&\quad \text{if} \quad \theta_{1_{k-1}} \in \Omega \supset \Omega_s \\
&\quad = \begin{Bmatrix} \theta_{1_{k-1}} + \Delta t \dot{\theta}_{1_{k-1}} \\ \dot{\theta}_{1_{k-1}} + \Delta t \frac{\sin(\mathrm{acos}(-\mathrm{L}_1/\mathrm{L}_2\cos(\theta_1)))\mathrm{a} + \left(\mathrm{L}_2\mathrm{K}^2_{\theta_2\theta_1} + \mathrm{L}_1\cos(\mathrm{acos}(-\mathrm{L}_1/\mathrm{L}_2\cos(\theta_1)) - \theta_1)\right)\dot{\theta}_1^2}{\mathrm{L}_1\sin(\mathrm{acos}(-\mathrm{L}_1/\mathrm{L}_2\cos(\theta_1)) - \theta_1)} |_{k-1} \\ (\dot{\theta}_{1_k} - \dot{\theta}_{1_{k-1}})/\Delta t + \delta_{k-1} \end{Bmatrix} \\
&\quad \text{if} \quad \theta_{1_{k-1}} \notin \Omega \supset \Omega_s \\
&\quad = \begin{Bmatrix} \theta_{1_{k-1}} + \Delta t \dot{\theta}_{1_{k-1}} \\ \dot{\theta}_{1_{k-1}} + \Delta t \ddot{\theta}_{1_{k-1}} \\ \ddot{\theta}_{1_{k-1}} + \delta_{k-1} \end{Bmatrix} \\
&\mathbf{y}_k = \begin{bmatrix} 1 & 0 & 0 \end{bmatrix} \mathbf{x}_k^{aug}
\end{aligned}
\tag{2.23}
$$

where $\mathrm{K}_{\theta_2\theta_1} = \partial\theta_2/\partial\theta_1$ is the sensitivity coefficient, and $\Delta t$ is the discretization time step (which has been set equal to 1 ms in the numerical simulation). The switching rule is defined as $\Omega = \{\theta_1 | \left|\theta_1 - (\theta_2 + k\pi)\right| \leq 0.08 \text{ rad}\}$.

Simulations have been carried out to assess the capability of different estimation strategies to deliver accurate estimations in the presence of measurement and model uncertainties. A simulation lasting 30 seconds has been tested, which highlights that no drift affects the estimates, i.e. the system is

stable (in the control theory sense).

The crank speed is obtained as the superposition of a constant-speed signal (12.56 rad/s) and a 2 Hz harmonic signal (whose amplitude is 1.256 rad/s). Two sample portions of the time history of the simulated accelerometer and encoder signals are shown respectively in Fig. 2.2 (a) and Fig. 2.2 (b).

Measurement noise has been added on both the encoder and the accelerometer signals to try reproducing more realistic conditions. In particular, Gaussian noises have been generated with amplitudes of, respectively, 0.003 rad for the encoder (corresponding to the resolution of a 2000 ppr encoder) and 0.03 $m/s^2$ for the accelerometer. (corresponding to the resolution provided by an accelerometer with sensitivity 10 $mV/ms^{-2}$ , whose signal is converted by a 16-bit ADC with input range of $\pm 10$ V ).

The estimated angular velocity and acceleration of the crank are shown respectively in Fig. 2.3 (a) and Fig. 2.3 (b). Estimation has been carried out using both the EKF and the SS-UKF observers, which are assumed as two representative examples of filters. The theory is however enough general to allow the use of other filters.

As far as acceleration estimation is concerned, the scheme proposed in Section 2.2.1.3, i.e. the one based on kinematic equations with numerical derivative, has been adopted.

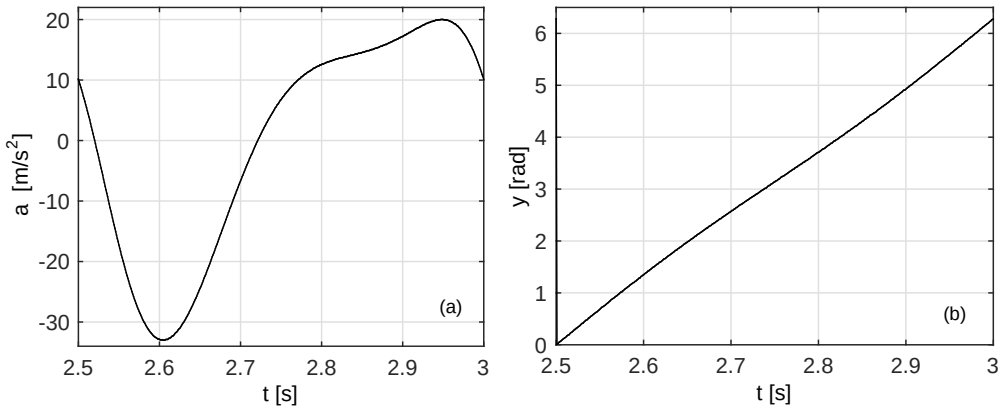


Figure 2.2: Simulated noisy measurements: slider acceleration (a) and crank angular position (b)

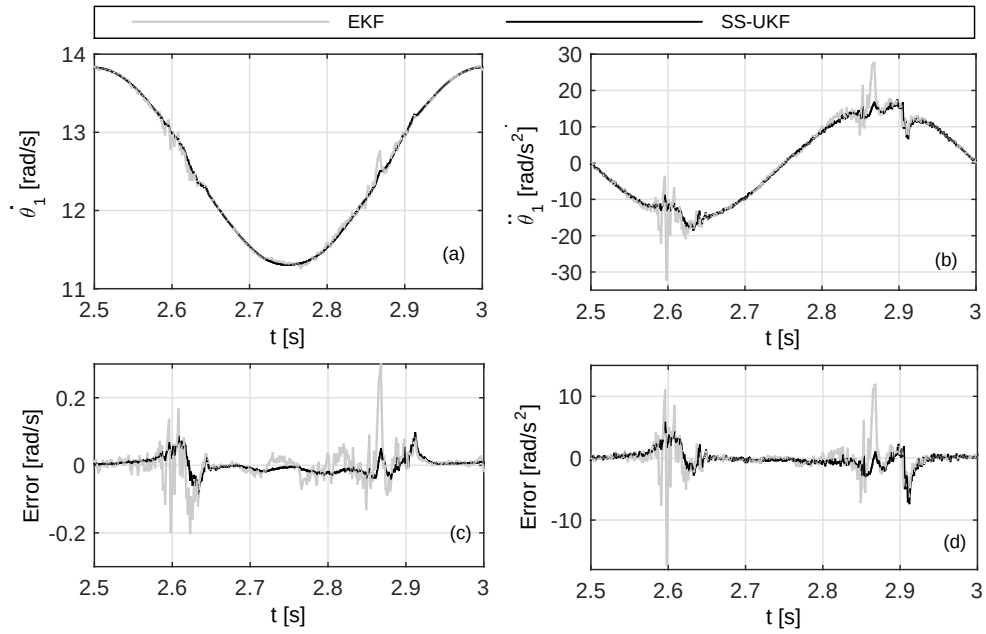


Figure 2.3: Estimated crank angular velocity (a) and acceleration (b). Velocity (c) and acceleration (d) estimation errors.

The estimates obtained are also compared with the actual velocity and acceleration computed analytically, i.e. those with no measuring noise. In particular, the errors between the estimated values and the actual ones are plotted in Fig. 2.3 (c) and Fig. 2.3 (d), to provide clearer evidence of the estimation accuracy.

The error diagrams show that both the observers lead to good velocity and acceleration estimates when the mechanism is far from model singularities, which are crossed at time instants 2.62 s and 2.88 s. When singularities are crossed, estimates become less accurate, but still acceptable.

In particular the use of the SS-UKF is marginally affected by singularity, especially in the estimation of speed. The SS-UKF superiority can be traced back, first of all, to the fact that it does not use any linearization and therefore does not require any Jacobian, whose computation is critical at the model switch, since in such instants the model is not ensured to be derivable. Additionally, the SS-UKF compute the prediction as the weighed

sum of more solutions related to different mechanism configurations (in term of positions, velocities, and, in this example, accelerations), rather than just solving the uncertain system model in a single configuration. All these considerations justify the superiority of this class of nonlinear observers to handle such nonlinear problems.

### 2.3.2 Test case II: two-dof planar mechanism

The laboratory setup shown in Fig. 2.4 (a) has been employed for the experimental validation of the theory developed. The system is an open-chain, planar mechanism with two links, two revolute joints, and therefore two dofs. This MBS recalls a typical planar underactuated manipulator: the shoulder joint is the sole actuated joint, driven by a DC servomotor, while the elbow joint is passive.

Two incremental encoders (with resolution 1000 ppr) measure the link rotations of both the joints, while two MEMS mono-axial accelerometers are mounted to each link for measuring the acceleration in the direction orthogonal to the link itself. Accelerometer sensitivities are 101.9 mV$(\mathrm{m/s^2})^{-1}$ for the one on link 1 and 6.81 mV$(\mathrm{m/s^2})^{-1}$ for the one on link 2, the signals are converted by a 16-bit ADC with input range +/-10 V.

In a manipulator like this one, state estimation could be useful, for instance, in the synthesis of advanced state feedback controllers (see e.g. [40]),

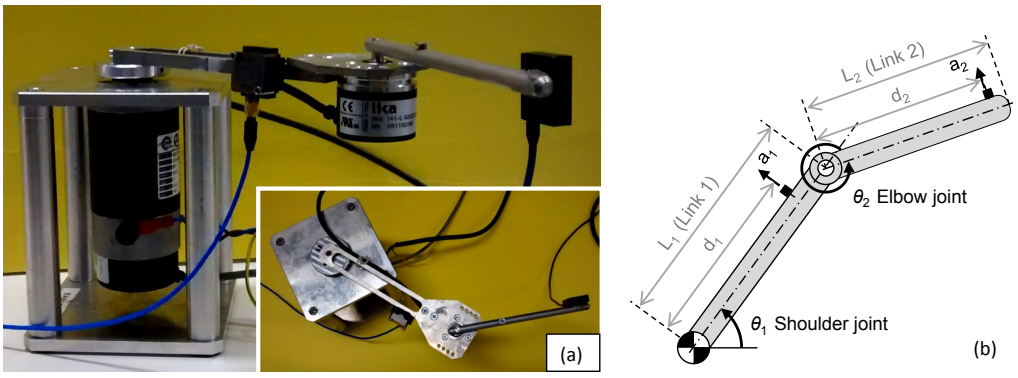


Figure 2.4: Pictures of the instrumented two-dof planar manipulator (seen from one side and above) (a). Kinematic scheme of the manipulator (b)

which require accurate knowledge of the joint speed and sometimes also acceleration. Yet, the direct measurement of such variables is unfeasible, and should be replaced by a suitable estimation.

To estimate the acceleration, the augmented state vector is defined as $\mathbf{x}^{aug} = \left\{\theta_1 \quad \theta_2 \quad \dot{\theta}_1 \quad \dot{\theta}_2 \quad \ddot{\theta}_1 \quad \ddot{\theta}_2\right\}^{\mathrm{T}}$, with the obvious meaning for the symbols (see Fig. 2.4 (b)). The state-space formulations of the kinematic constraints has been obtained by discretizing the following continuous-time state-space representation,

$$\dot{\mathbf{x}}(t) = \begin{Bmatrix} \dot{\theta}_1(t) \\ \dot{\theta}_2(t) \\ \ddot{\theta}_1(t) \\ \ddot{\theta}_2(t) \end{Bmatrix} = \begin{Bmatrix} \dot{\theta}_1(t) \\ \dot{\theta}_2(t) \\ \mathrm{a}_1(t)/\mathrm{d}_1 \\ -\mathrm{a}_1(t)\left(\mathrm{L}_1\cos\left(\theta_2(t)\right) + \mathrm{d}_2\right)/(\mathrm{d}_1\mathrm{d}_2) + \\ \quad + \left(\mathrm{a}_2(t) - \mathrm{L}_1\sin\left(\theta_2(t)\right)\dot{\theta}_1^2(t)\right)/\mathrm{d}_2 \end{Bmatrix} \tag{2.24}$$

and then augmenting the discrete model with the acceleration equations. Among the three strategies, the closed-loop estimation of accelerations has been performed using the scheme based on kinematic equations with random walk (see Section 2.2.1.1). In Eq. 2.24, $\mathrm{a}_1$ and $\mathrm{a}_2$ are the accelerations measured by the two accelerometers attached to link 1 and 2, which are located at distances $\mathrm{d}_1$ and $\mathrm{d}_2$ from respectively the shoulder and the elbow joints. Such accelerations are the system inputs $\left(\mathbf{u} = \{\mathrm{a}_1 \quad \mathrm{a}_2\}^{\mathrm{T}}\right)$. The output vector $\mathbf{y}$ comprises the rotations of both the joints to represent correctly the zero-frequency dynamics of both the links, and therefore linearly depends on the state:

$$\mathbf{y} = \begin{Bmatrix} \theta_1 \\ \theta_2 \end{Bmatrix} = \begin{bmatrix} 1 & 0 & 0 & 0 & 0 & 0 \\ 0 & 1 & 0 & 0 & 0 & 0 \end{bmatrix} \mathbf{x}^{aug} \tag{2.25}$$

This set of measurements defines a less challenging condition for the EKF since it reduces the system model nonlinearities, by making g a linear function. Nonetheless, it will be shown by the experimental recordings that also in this case the SS-UKF allows obtaining better results. It is also worth noticing that this choice of input and output vectors guarantees respectively the existence of $[\mathbf{S}^{\mathrm{T}}\mathbf{S}]^{-1}$ and the observability of the system for any joint configuration.

Two different tests have been carried out. The first test ("TEST 1") consists of a sequence of transient responses imposed by quasi-impulsive excitations exerted to link 1 by the actuator. The encoder and accelerometer signals recorded during the test are shown in Fig. 2.5. The test lasted 10 seconds. The angular velocities and accelerations estimated through the EKF and the SS-UKF are shown in Figs. 2.6 and 2.7 for, respectively, the shoulder and elbow joints. In the same figures, the velocities and accelerations computed by means of just numerical derivatives of encoder signals are shown too. To this purpose a seventh-order, low-noise Lanczos differentiator [41] has been adopted, and implemented in a non-causal form (i.e. two sided), in order to smooth noise and reduce time delay. Nonetheless the resulting velocities and accelerations appear extremely noisy. In contrast, very smooth estimations are provided by both the observers, without any significant delay. This comparison makes the usefulness of state observers apparent: the real-time estimations provided by the EKF and the SS-UKF are much more accurate and grant results that can be obtained only through non-causal

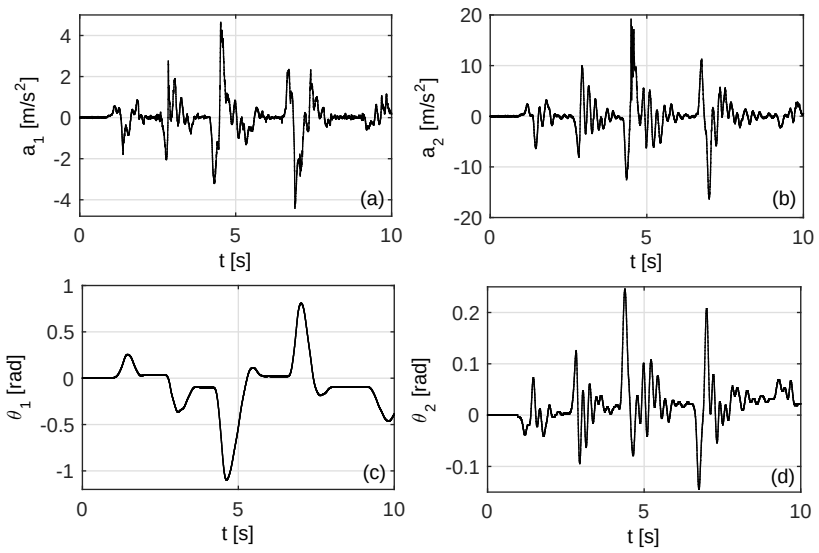


Figure 2.5: TEST 1. System input: acceleration measurements at link 1 (a) and link 2 (b). System output: encoder measurements at the shoulder (c) and elbow (d) joints

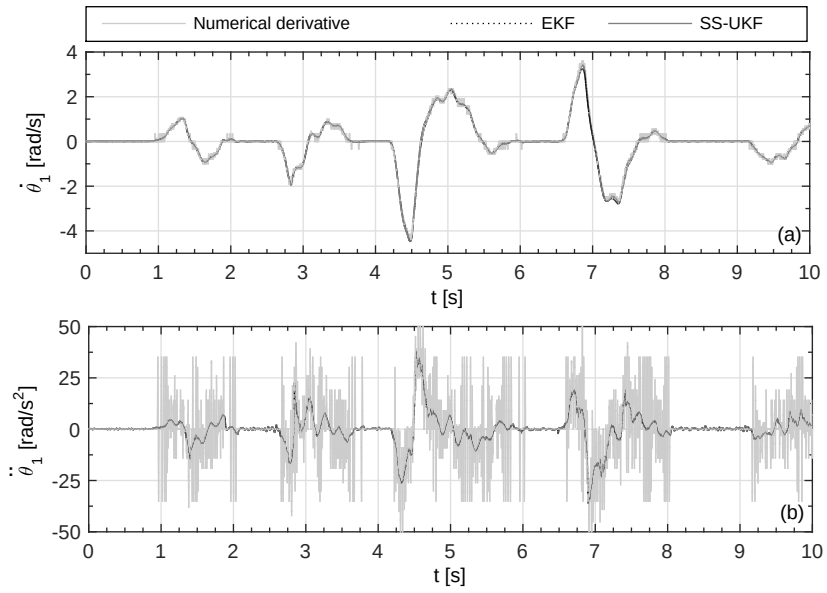


Figure 2.6: TEST 1. Estimated angular velocity (a) and acceleration (b) at the shoulder joint

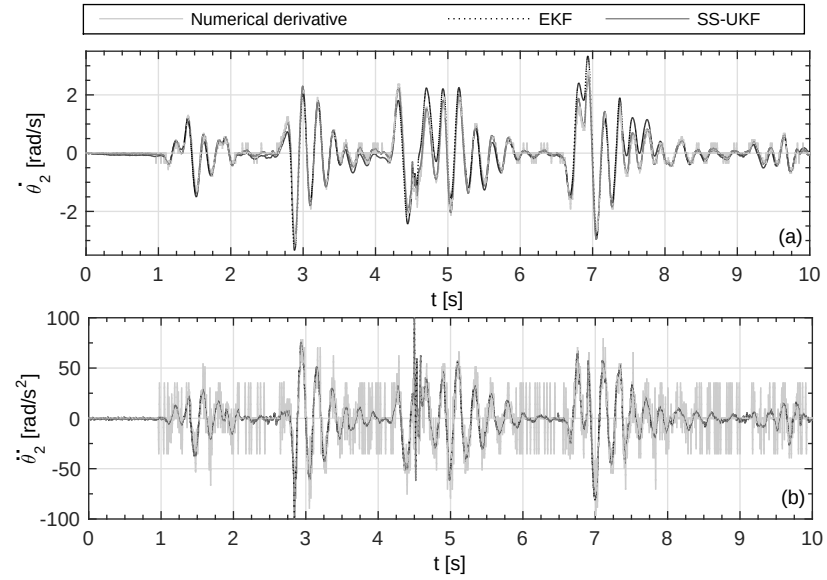


Figure 2.7: TEST 1. Estimated velocity (a) and acceleration (b) at the elbow joint (b)

filtered derivatives, which however cannot be employed in real-time computation. Among the two observers, the velocities estimated through the SS-UKF appear less affected by noise, while accelerations estimates are almost overlapped, as a consequence of the fact that positions and velocities scarcely contribute to acceleration terms in this setup, i.e. joint accelerations mostly depend on the measured input.

In the second test carried out ("TEST 2"), the shoulder joint position is commanded to track a sweep excitation ranging from 10 to 1 Hz, and lasting 9 seconds. For clarity of representation just a sample portion of each signal is shown in Figs. 2.8, 2.9, and 2.10. Similar results are obtained in the whole frequency range but they are not shown for brevity.

The measured signals are shown in Figs. 2.8 while the velocities and accelerations estimated by the EKF and the SS-UKF are shown in Fig. 2.9 and 2.10. In the same figures, velocities and accelerations obtained by means of a numerical derivative of encoder signals are shown too.

These results are coherent with those yielded by the previous numerical

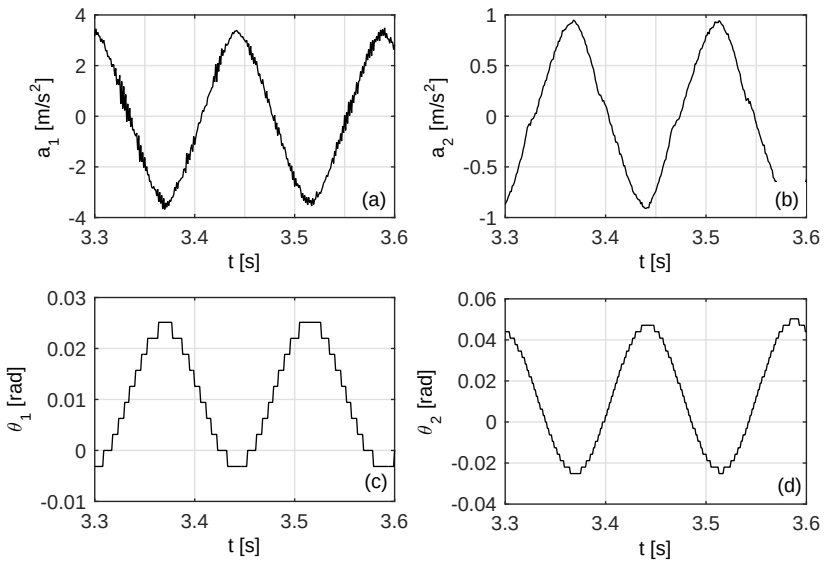


Figure 2.8: TEST 2. System input: acceleration measurements at link 1 (a) and link 2 (b). System output: encoder measurements at the shoulder (c) and elbow (d) joints

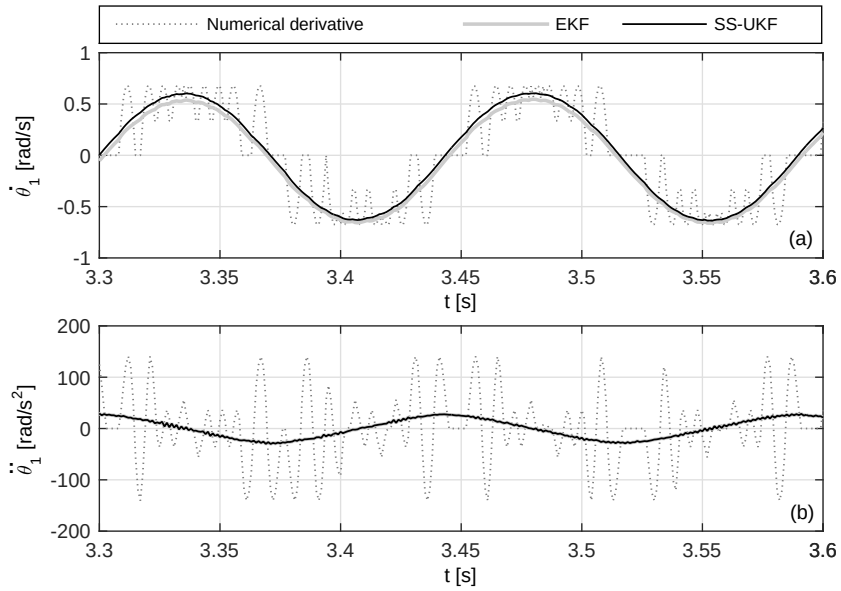


Figure 2.9: TEST 2. Estimated angular velocity (a) and acceleration (b) at the shoulder joint

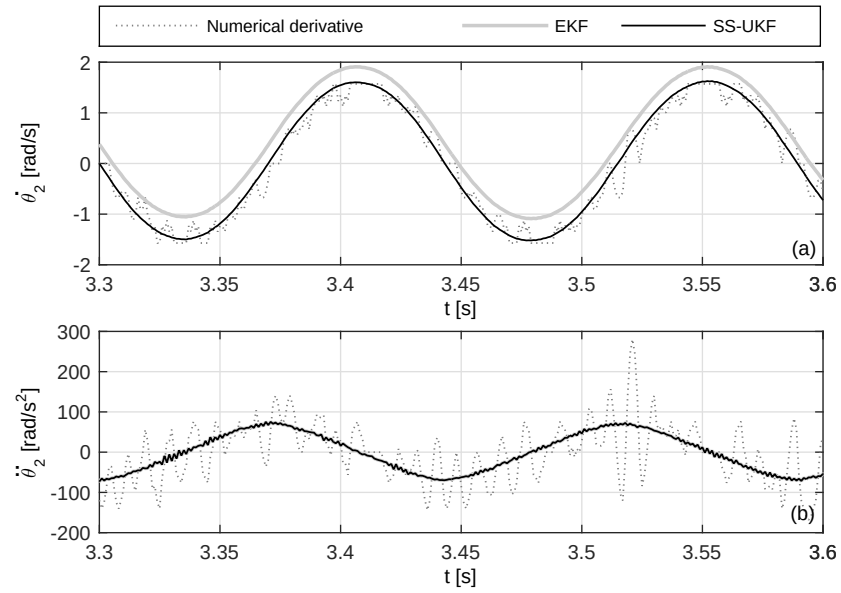


Figure 2.10: TEST 2. Estimated velocity (a) and acceleration (b) at the elbow joint (b)

investigation and corroborate the usefulness and effectiveness of the proposed approach to kinematic state estimation. The real-time applicability of the approach is however also influenced by its computational efficiency, which is briefly addressed in the Section 2.3.3.

### 2.3.3 CPU time comparison between filters

The computational efficiency of the proposed approach strictly depends on the algorithms used for computing state and observation predictions and clearly impacts on the CPU time needed to compute the estimates. In this work only the EKF and the SS-UKF have been implemented, and hence the analysis is restricted to such observes. Although a rigorous analysis of the computational complexity of the two observers goes beyond the scope of this study, some interesting indications can be found in the comparison of the computational efforts related to the two Matlab implementations of the estimation strategies.

As far as the slider-crank mechanism is concerned, 8.38 seconds of CPU time were needed on average (on a PC with Core i7-2700K, RAM 16 GB) to run 30 seconds in the case of the SS-UKF, while 25.15 seconds were necessary to perform the same simulation using the EKF.

When considering the two-dof MBS , the offline state estimations in TEST 1, lasting 10 seconds, just took, on average over a large number of repetitions, 0.85 seconds of CPU time when using the SS-UKF and 6.65 seconds with the EKF. Similarly, in TEST 2, lasting 9 seconds, state estimations took on average 0.78 seconds when performed using the SS-UKF, and 6.00 seconds with the EKF.

Therefore, in all the tests the SS-UKF, which is renown to be the most efficient among the SPKFs, ran much faster than the EKF, mainly because it does not require the evaluation of the Jacobian matrices.

## 2.4 Chapter summary

This chapter has introduced and presented a general theory for the design of nonlinear state observers based on kinematic constraint equations, suitable

for MBSs with rigid links, negligible joint clearance, holonomic and sclerono-mous constraints. The approach is general, in the sense that it can be used for both open-chain and closed-chain MBSs. The use of filters based on kinematic constraint equations is advantageous since such equations are much less affected by uncertainty than the dynamic equations of motion usually employed in state observers. Therefore the impact of model uncertainty in the estimation accuracy is considerably reduced. Indeed, kinematic state estimation just relies on geometric equations and on the measurement of kinematic quantities, while it does not require the knowledge of dynamic equations of motion and external forces, which are often unknown in real-world applications.

The chapter deals with all the aspects concerning kinematic estimation, including state-space first-order formulation of the kinematic constraint equations in both continuous-time and discrete-time, and the suitable definition of model inputs and outputs. Additionally, two critical issues are tackled to extend the range of applications of kinematic filters: the estimation of the state derivative with discrete-time schemes and the estimation in model singularity. As far as the first topic is concerned, three schemes are proposed to perform closed-loop estimation of state derivative through the prediction-correction iterations, aimed at compensating the numerical derivation noise and the model uncertainty. As far as the estimation in singular configurations is concerned, a switching model is proposed, which approximates the kinematic constraint equations with a random walk model with Gaussian noise in a neighborhood of the singular configurations.

Among the numerous strategies to implement nonlinear filters based on the Kalman filter theory, particular attention is paid in this dissertation to the use of sigma point unscented Kalman filters (SPKFs), whose application in the field of kinematic estimation has been proposed in literature for the first time in author's publication [42]. These filters are more accurate than the EKF in tackling nonlinearities, since they do not use model linearization to propagate the covariance matrices and therefore to compute the filter gains. Indeed, SPKFs compute the prediction of both the state vector and the covariance matrices as the weighed sum of more solutions of the constraint equations in different mechanism configurations. Besides improving

the estimation accuracy, especially in the presence of kinematic singularities, this approach does not require the time-consuming computation of the model Jacobian matrices.

Numerical and experimental assessments of the theory proposed are provided through two different rigid-link MBSs: a simulated closed-chain, single-dof mechanism (slider-crank mechanism) and a laboratory test rig consisting in a two-dof, two-link, planar mechanism with two revolute joints. Estimation is performed through the EKF and, as a representative example of SPKFs, the SS-UKF. The results clearly show the correctness and the effectiveness of the theory proposed. Indeed, precise estimations of the kinematic variables are obtained, also including the derivative of the state. Model singularities are effectively crossed too. Finally, the comparison between the performances of the observers highlights that the SS-UKF is more accurate and faster than the widely employed EKF. Hence it turns out to be the most appropriate to kinematic state estimation for rigid-link MBSs featuring the hypothesis made.

# Chapter 3

# Force estimation in rigid-link multibody systems

The problem of force estimation is typically called "unknown input estimation" in literature. Such a definition makes implicit reference to the use of dynamic models in state estimations, since such an approach requires that all the forces (and torques) acting on the system are known and used as the inputs of the dynamic models. Therefore, traditional approaches cannot be implemented whenever such forces are unknown inputs, unless the unknown forces are treated as unknown system parameters [11, 43, 44] and therefore included in an augmented state together with positions and velocities. This approach usually assumes a rough model of the force, such as the so-called random walk, that is a constant value plus white noise. Given these relevant approximations, the resulting system model may lead to diverging or wrong estimates of the kinematic state.

In Chapter 2 it has been proved that the estimation of the kinematic variables in rigid link MBSs (with negligible joint clearance and holonomic and scleronomous constraints) can be effectively based on just the kinematic constraint equations and on kinematic measurements, through the so-called Kinematic Kalman Filter (KKF). Indeed, the use of kinematic equations requires a lower number of parameters compared to dynamic models, and does not require any force measurement. These features boost the achievement of higher levels of accuracy. Following this idea, this chapter proposes a novel technique for improving the simultaneous estimations of the kinematic

state and the external forces in rigid-link MBSs featuring the aforementioned hypothesis.

The proposed two-stage approach [45] consists in using acceleration measurements and in splitting the estimation process into two nonlinear estimations running simultaneously. The first is carried out by a KKF of the type discussed in Chapter 2; the second one is carried out by a force observer based on dynamic models. The KKF estimates positions, velocities and accelerations regardless of the knowledge of the external forces, and hence is unbiased by any uncertainty introduced by the unknown forces and by any force approximate model to be employed in the estimation. In contrast, the force observer, which also employs a nonlinear KF, estimates the unknown forces by employing, as input, the estimated kinematic state and, as model, the motion equations augmented with some force models, in order to have a well-posed system of equations. All the estimations are carried out in a prediction-correction iteration to compensate for model uncertainties and measurement noise.

The chapter is set out as follows: Section 3.1 describes the proposed two-stage approach. In Section 3.2 two numerical tests proving the soundness of the proposed theory are presented. A slider-crank mechanism and an excavator arm are considered. Both the nonlinerar estimation algorithms discussed in Section 1.2 are adopted. Finally, concluding remarks are given in Section 3.3.

## 3.1 The two-stage observer

### 3.1.1 Overview of the two-stage observer

The aim of an observer is to compensate for both the model uncertainties and the measurement errors to reconstruct the system state as accurately as possible. Nevertheless, the use of inaccurate models, can prevent obtaining precise and stable estimates, as well as fast convergence, even if modeling errors affect just some equations, or just some inputs are uncertain. This is a common issue in MBSs, since some of the external forces exciting the system (i.e the system inputs) are often neither measured nor easy to be

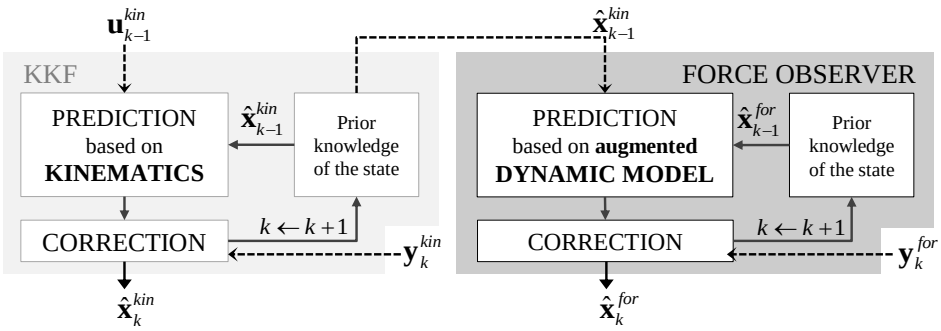


Figure 3.1: Schematic representation of the proposed two-stage approach

estimated through constitutive laws (such as, for example, the elastic forces exerted by linear springs, in accordance with the well known Hook's law). However, the state variables of MBSs are kinematic quantities, and in the case of MBSs with rigid links and negligible joint clearance, their evolution can be predicted by means of just kinematic constraint equations, which do not depend on forces and are much less affected by uncertainties than motion equations. Such considerations justify the choice of estimating the kinematic state and the unknown forces by two observers running simultaneously and only partially coupled (i.e. a KKF and a force observer) rather than by a single fully coupled observer.

The KKF estimates an augmented kinematic state, i.e. positions, velocities and accelerations (collected in vector $\mathbf{x}_k^{kin}$), regardless of the knowledge of the external forces, and hence is unbiased by the uncertainty introduced by unmeasured forces or by the approximate force models employed in the observer. The KKF just uses kinematic constraint equations and some measurements of kinematic quantities as inputs and outputs.

In the second stage, the force observer estimates the unmeasured forces, by employing dynamic models and a number of approximate force models ensuring that the number of model equations matches the one of the forces applied to the system, so that the estimation problem is well-posed. The input of the force observer is the kinematic state estimated at the first stage, while the correction is performed through some direct or indirect measurements of the known forces.

The overall structure of the proposed two-stage estimation strategy is

summarized in Fig. 3.1, where superscripts $kin$ and $for$ indicate, respectively, variables belonging to kinematic and force observers, $\hat{\mathbf{x}}$ denotes the estimated state vector, while vectors $\mathbf{u}$ and $\mathbf{y}$ denote observer inputs and outputs. The scheme clearly shows the type of coupling between the two observers: the output of the KKF plays the role of the measured input of the force observer. In contrast, the KKF does not depend on the force observer. This feature ensures that the uncertainties introduced by the unknown external forces and by the model approximations assumed do not affect the estimation of the kinematic state.

The synthesis of a kinematic observer has been deeply discussed in Chapter 2, while the force observer is described in detail in the following subsection.

### 3.1.2 Force observer

The synthesis of the second stage, force observer relies on the dynamic model, to be formulated through a non redundant set of coordinates. Let us define the force vector $\mathbf{x}^{for}$, including both the known and unknown external forces acting on the MBS, which are collected, respectively, in vectors $\mathbf{F}_1$ and $\mathbf{F}_2$:

$$\mathbf{x}^{for} = \left\{ \mathbf{F}_1^{\mathrm{T}} \quad \mathbf{F}_2^{\mathrm{T}} \right\}^{\mathrm{T}} \tag{3.1}$$

In the case the motion equations can be inverted by explicating the known external forces as functions of the kinematic quantities $\mathbf{z}$, $\dot{\mathbf{z}}$ and $\ddot{\mathbf{z}}$, and of the unknown forces $\mathbf{F}_2$, the following relation can be written:

$$\mathbf{F}_1 = \boldsymbol{f}_{12} \left( \mathbf{F}_2, \mathbf{z}, \dot{\mathbf{z}}, \ddot{\mathbf{z}} \right) \tag{3.2}$$

where $\boldsymbol{f}_{12}$ is the nonlinear function representing the dynamic model. Once the values of the kinematic variables are known, Eq. (3.2) is a kinetostatic problem and $\boldsymbol{f}_{12}$ is a set of $n$ algebraic equations in the unknowns $\mathbf{x}^{for}$. Therefore, it is not suitable to be directly employed as a system equation in KFs, which impose the use of models in first-order ODE formulation. In contrast, $\boldsymbol{f}_{12}$ would be suitable to be employed in the so-called Disturbance Observers [46], which, however, perform the estimates of the external forces

without the prediction-correction "closed loop" iterations used to compensate for model uncertainty and errors, and therefore is not of interest for this work.

In order to make the dynamic model suitable for the synthesis of the observer, Eq. (3.2) is transformed into a set of first-order difference equations (in the discrete-time domain). The state vector is the external force vector (see Eq. (3.1)). The output vector includes the known forces $\mathbf{F}_1$, i.e. $\mathbf{y}^{for} = \mathbf{F}_1$, which allow computing the filter innovation (i.e. the correction). In order to ensure the system observability, $\mathbf{y}^{for}$ should include at least $n$ non-redundant force measurements. The first-order difference equations are formulated by relating the known forces at time $k$ to the kinematic quantities and to the unknown forces computed at the previous step through the dynamic models in Eq. (3.2). Then, in order to account for the approximation introduced by this shift of a discretization step, as well as model uncertainties, an additive noise $\boldsymbol{\delta}_{k-1}$ is included in the model, to take advantage of the probabilistic nature of the state observer:

$$\mathbf{F}_{1_k} = \boldsymbol{f}_{12}\left(\mathbf{F}_{2_{k-1}}, \mathbf{z}_{k-1}, \dot{\mathbf{z}}_{k-1}, \ddot{\mathbf{z}}_{k-1}\right) + \boldsymbol{\delta}_{k-1} \tag{3.3}$$

As a typical assumption, $\boldsymbol{\delta}_{k-1}$ is modeled as white noise, even though band-limited ("colored") noise could be easily adopted whenever necessary.

A second set of equations should be also included to model the unknown forces at time step $k$, in order to have a well-defined system of equations. Such a set of equations can include any type of force model, if known. Conversely, if no information about such forces is available, a random walk model is suggested, as often done in literature. Although this is a rough and approximate model, the use of a two-stage approach makes the estimation of kinematic variables robust to such an uncertainty source. Without lack of generality, in the following developments the unknown forces are modeled by means of random walk models. Basically, a random walk model approximates $\mathbf{F}_2$ by assuming that a current value of $\mathbf{F}_2$ ($\mathbf{F}_{2_k}$) is equal to the previous one ($\mathbf{F}_{2_{k-1}}$), plus a white noise term ($\delta^*_{k-1}$):

$$\mathbf{F}_{2_k} = \mathbf{F}_{2_{k-1}} + \delta^*_{k-1} \tag{3.4}$$

The system model adopted in the second stage observer for the estimation of the state vector $\mathbf{x}^{for}$ is therefore represented through Eq. (3.3) and Eq. (3.4).

The input $\mathbf{u}_{k-1}^{for}$ is the estimated augmented kinematic state, computed at the previous time step through the kinematic observer, $\mathbf{u}_{k-1}^{for} = \hat{\mathbf{x}}_{k-1}^{kin} = \left\{\mathbf{z}_{k-1}^{\mathrm{T}} \quad \dot{\mathbf{z}}_{k-1}^{\mathrm{T}} \quad \ddot{\mathbf{z}}_{k-1}^{\mathrm{T}}\right\}^{\mathrm{T}}$. The model assumed for the state prediction is therefore the following one:

$$\begin{aligned} \mathbf{x}_k^{for} &= \boldsymbol{f}^{for}\left(\mathbf{x}_{k-1}^{for}, \mathbf{u}_{k-1}^{for}\right) = \\ \begin{Bmatrix} \mathbf{F}_{1_k} \\ \mathbf{F}_{2_k} \end{Bmatrix} &= \begin{Bmatrix} \boldsymbol{f}_{12}\left(\mathbf{F}_{2_{k-1}}, \mathbf{x}_{k-1}^{kin}\right) \\ \mathbf{F}_{2_{k-1}} \end{Bmatrix} \end{aligned} \tag{3.5}$$

All the equations are supposed to be affected by noise. As an alternative formulation, the dynamic model can be expressed by explicating $\mathbf{F}_2$ as a function of the kinematic state and of the known forces $\mathbf{F}_1$ (through function $\boldsymbol{f}_{21}$ representing the dynamic model):

$$\mathbf{F}_2 = \boldsymbol{f}_{21}\left(\mathbf{F}_1, \mathbf{z}, \dot{\mathbf{z}}, \ddot{\mathbf{z}}\right) \tag{3.6}$$

and the random walk model is adopted to approximate $\mathbf{F}_1$:

$$\mathbf{F}_{1_k} = \mathbf{F}_{1_{k-1}} + \delta_{k-1}^{*} \tag{3.7}$$

In this case, the model used for the estimation is the following one:

$$\begin{aligned} \mathbf{x}_k^{for} &= \boldsymbol{f}^{for}\left(\mathbf{x}_{k-1}^{for}, \mathbf{u}_{k-1}^{for}\right) = \\ \begin{Bmatrix} \mathbf{F}_{1_k} \\ \mathbf{F}_{2_k} \end{Bmatrix} &= \begin{Bmatrix} \mathbf{F}_{1_{k-1}} \\ \boldsymbol{f}_{12}\left(\mathbf{F}_{1_{k-1}}, \mathbf{x}_{k-1}^{kin}\right) \end{Bmatrix} \end{aligned} \tag{3.8}$$

The selection of the most suitable formulation, between Eq. (3.5) and Eq. (3.8), is based on the existence of $\boldsymbol{f}_{12}$ and $\boldsymbol{f}_{21}$, which is in turn affected by the presence of singular configurations.

The analysis of the equations highlights that the number of unknown forces that can be estimated correctly (i.e. with bounded error) is not greater than the number of system degrees of freedom, provided that the same number of forces (e.g. the control forces exerted by the actuators) is known (or at least accurately estimated indirectly, e.g. through current measurements).

These conditions should not be regarded as drawbacks of this method, since they also hold in the case of the disturbance observer and in the case of the estimation through a single-stage dynamic observer augmented with random walk models for the external forces.

### 3.1.3 Method discussion

The method formulation proposed in the previous sections highlights some of the benefits of the two-stage approach. Indeed it properly merges the use of kinematic models, dynamic models and the random walk approximations to reduce the uncertainty due to the presence of unknown forces.

The first stage kinematic observer allows unbiased estimation of the kinematic augmented state, and prevents the drift due to the effect of unknown forces in the case of observers solely based on dynamic models. This is an advantage over traditional observers where simultaneous state and force estimates are obtained through dynamic MB models. Indeed, in the latter case, the estimation of the kinematic variables can be severely affected by the unknown forces and by the approximate random walk models usually adopted. These uncertainty sources and approximations often lead to unbounded estimation errors (i.e. observer instability).

Additionally, the proposed approach overcomes the "open-loop" nature of several disturbance observers recently adopted in modern motion control schemes, by employing the dynamic equations within the frame of a "closed-loop" prediction-correction iteration to compensate for model uncertainty and sensor noise.

All these features justify the slight increase in the complexity of the proposed two-stage approach, which requires some more sensors to measure accelerations and impose performing kinematic estimation separately. However, as already proved in Chapter 2 and as it is further confirmed in Section 3.2, the low computational effort usually required by kinematic observers does not prevent the real-time implementability of the proposed two-stage strategy.

## 3.2 Numerical results

Two tests are proposed to prove the effectiveness of the theory developed. The first test involves a single-dof, closed-chain, planar mechanism (slider-crank mechanism). The second one involves the arm of an excavator, so it is an open chain, three-dof, three-link, planar mechanism.

### 3.2.1 Test case I: slider-crank mechanism

The theory developed has been applied to a slider-crank mechanism lying on the vertical plane. A scheme of the mechanism is depicted in Fig. 3.2.

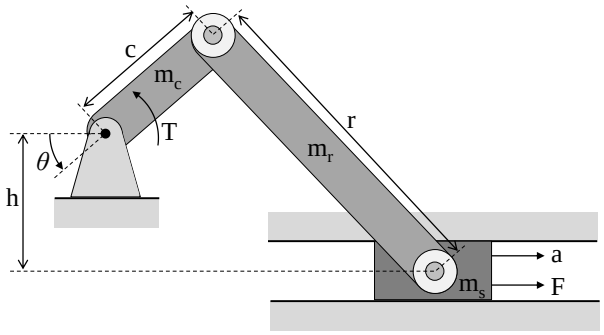


Figure 3.2: Scheme of the slider-crank mechanism

It has been assumed that the crank is driven by a known torque T, whose time history is shown in Fig. 3.3(c). The aim of the test is to estimate the crank angular velocity $\dot{\theta}$ and acceleration $\ddot{\theta}$, and the force F applied to the slider.

In order to carry out such estimations it is necessary to equip the system with some sensors. Therefore, it has been assumed that the system is equipped with an incremental encoder and a mono-axial accelerometer, measuring respectively the crank angular position $\theta$ and the slider linear acceleration a. In particular the slider acceleration has been used as the input of the kinematic observer, while the crank angular position as the output. The torque driving the crank has been set as the output of the force observer.

In order to reproduce a more realistic situation, significant measurement noise has been added to all the simulated signals. Such signals are shown in Figs. 3.3(a), (b) and (c). The effect of noise is made evident by the enlarged views given in Figs. 3.3(d), (e) and (f). In particular, Gaussian noises have been generated with amplitudes of, respectively, 0.003 rad for the encoder (corresponding to the resolution of an encoder with 2000 pulses per revolution), 0.05 $m/s^2$ for the accelerometer (corresponding to the resolution provided by an accelerometer with sensitivity $6{\cdot}10^{-3}$ $V/ms^{-2}$, whose signal is converted by a 16-bit ADC with input range $\pm 10$ V ), and 0.28 Nm for the

Table 3.1: Geometric and inertial parameters (nominal ± error)

| | Crank | Rod | Slider | Frame |
|---|---|---|---|---|
| Mass [kg] | $m_c$ =1.872-0.0191 | $m_r$ =3.744-0.15 | $m_s$ =1.2+0.012 | - |
| Length [mm] | c =300-3 | r =600+12 | - | h =50-1 |

Table 3.2: Variables involved in the estimation process: two-stage approach

| | State | Inputs | Outputs |
|---|---|---|---|
| KKF | $\mathbf{x}^{kin} = \left\{ \theta \quad \dot{\theta} \quad \ddot{\theta} \right\}^{\mathrm{T}}$ | $\mathrm{u}^{kin} = \mathrm{a}$ | $\mathrm{y}^{kin} = \theta$ |
| Force observer | $\mathbf{x}^{for} = \left\{ \mathrm{F} \quad \mathrm{T} \right\}^{\mathrm{T}}$ | $\mathbf{u}^{for} = \left\{ \theta \quad \dot{\theta} \quad \ddot{\theta} \right\}^{\mathrm{T}}$ | $\mathrm{y}^{for} = \mathrm{T}$ |

Table 3.3: Variables involved in the estimation process: benchmark approach

| State | Inputs | Outputs |
|---|---|---|
| $\mathbf{x}^{ben} = \left\{ \theta \quad \dot{\theta} \quad \ddot{\theta} \quad \mathrm{F} \right\}^{\mathrm{T}}$ | $\mathrm{u}^{ben} = \mathrm{T}$ | $\mathbf{y}^{ben} = \left\{ \theta \quad \mathrm{a} \right\}^{\mathrm{T}}$ |

torque sensors (corresponding to 0.35 % of the full scale of a 80 Nm torque sensor). Besides measurement noise, uncertainty on the model parameters has been introduced through some deviations between the nominal and actual values of geometrical and inertial model parameters (see Tab. 3.1).

All the variables involved in both the KKF and the force observer are listed in Tab. 3.2.

The angular velocity and acceleration of the crank estimated through the kinematic observer are plotted respectively Fig. 3.4(a) and Fig. 3.5(a), while the force exciting the slider, and estimated through the force observer, is shown in Fig. 3.6(a).

Figures 3.4(b), 3.5(b) and 3.6(b) plot instead the estimates obtained with a traditional external force estimation approach (hereafter called benchmark approach), which estimates the kinematic states and the unknown force together, by means of a dynamic model augmented with a random walk to represent the external force F (see, for example, [47]).

The state, the inputs and the outputs employed in the benchmark ob-

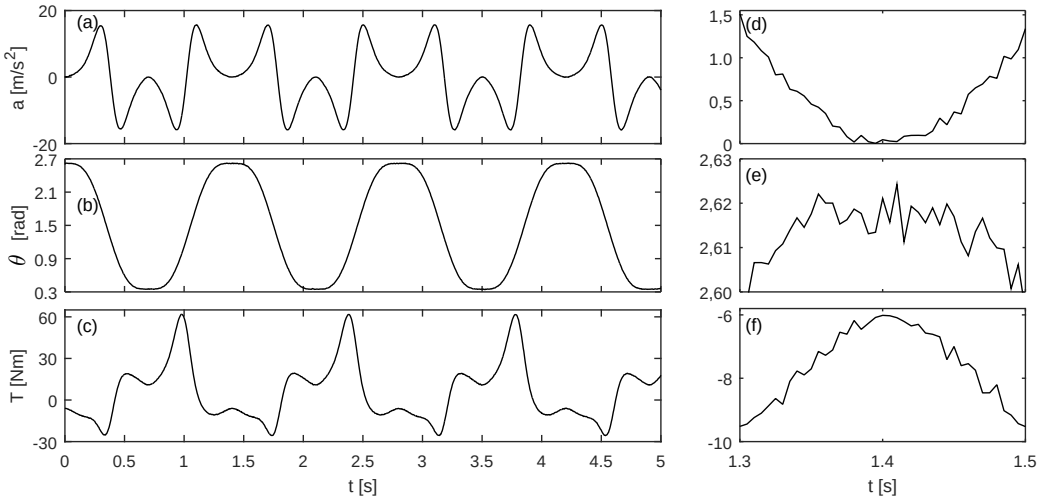


Figure 3.3: Simulated noisy measurements: slider acceleration (a), crank angular position (b), torque (c), and their respective enlarged views (d), (e) and (f)

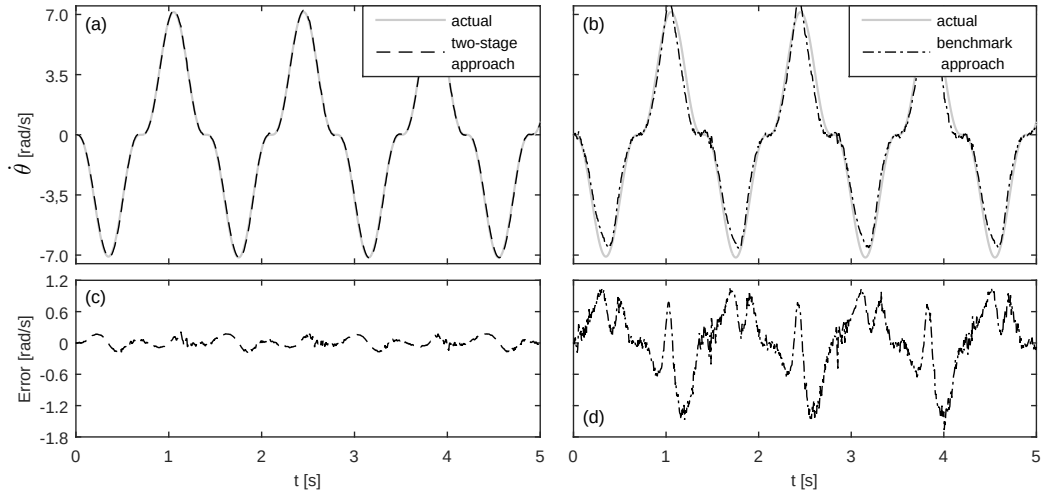


Figure 3.4: Crank angular velocity, $\dot{\theta}$, estimated through the two-stage approach (a) and the benchmark one (b). Crank angular velocity estimation error of the two-stage approach (c) and the benchmark one (d)

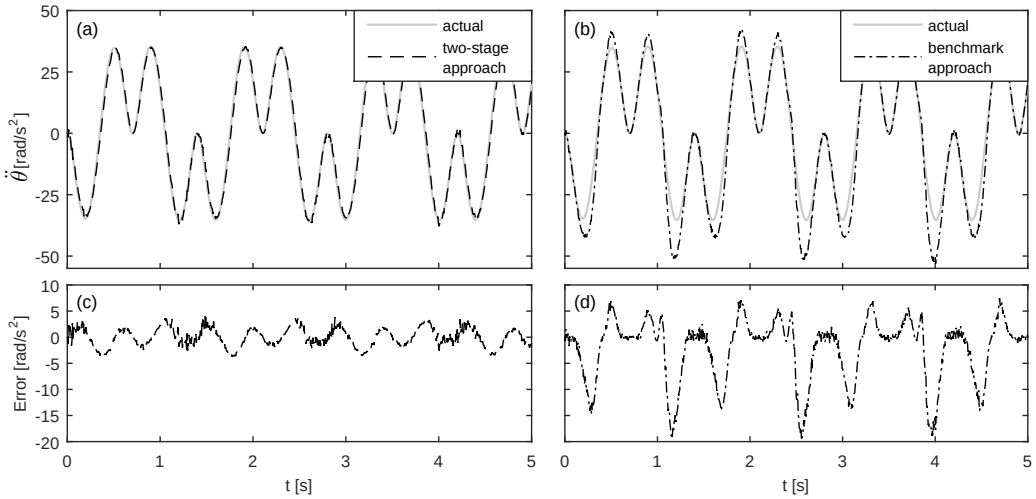


Figure 3.5: Crank angular acceleration, $\ddot{\theta}$, estimated through the two-stage approach (a) and the benchmark one (b). Crank angular acceleration estimation error of the two-stage approach (c) and the benchmark one (d)

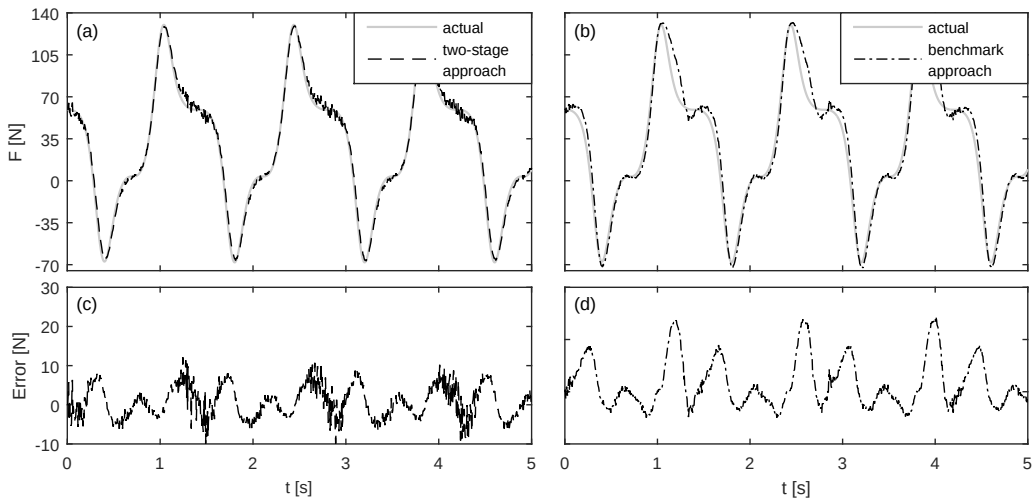


Figure 3.6: Force acting on the slider, F, estimated through the two-stage approach (a) and the benchmark one (b). Force estimation error of the two-stage approach (c) and the benchmark one (d)

server are listed in Tab. 3.3. By comparing Tabs. 3.2 and 3.3, it is evident that identical measurements have been fed to the two estimation strategies, which strengthens the meaningfulness of the comparison.

The figures from 3.4 through 3.6 also show in gray lines the actual (simulated) values of the variables to be estimated, and the errors between the estimated values and the actual ones. The comparison between the error diagrams, obtained by the two-stage approach (Figs. 3.4(c)), 3.5(c) and 3.6(c) and the benchmark one (Figs. 3.4(d), 3.5(d) and 3.6(d)), clearly highlights that more accurate estimates of both the state and the unknown input force can be obtained through the two-stage approach. For sake of clarity, just the results of estimates obtained using the SS-UKF algorithm are shown here. Nevertheless almost identical results are obtained using the EKF algorithm.

In order to simplify the comparison among the performances of observers based on the two-stage strategy (either using the EKF or the SS-UKF) and the traditional single-stage ones, Tab. 3.4 lists the root mean square errors between the estimated and actual values of the crank angular velocity $\dot{\theta}$, and acceleration $\ddot{\theta}$, and of the external force F applied to the slider. Once again the comparison confirms the better performances of the two-stage approach.

Finally, it is worth highlighting the small computational effort required by the proposed approach: the CPU times (on a PC with Core i7-2700K, RAM 16 GB) taken by each approach considered are listed in Tab. 3.5. All the observers have been implemented using Matlab. It is apparent that very similar CPU times are required by the two approaches: the proposed approach allows getting more accurate estimates of both state and unknown input forces, without compromising real time implementation possibilities.

Table 3.4: Root mean square errors between the estimated values and the corresponding actual ones

| | Two-stage observers | | Benchmark observers | |
|---|---|---|---|---|
| | SS-UKF | EKF | SS-UKF | EKF |
| $e_{rms}(\dot{\theta})$ | 0.0846 | 0.0842 | 0.6558 | 0.7215 |
| $e_{rms}(\ddot{\theta})$ | 1.8112 | 1.8226 | 7.0533 | 7.4521 |
| $e_{rms}$(F) | 4.2988 | 4.4267 | 10.8249 | 11.5015 |

Table 3.5: CPU times taken for 5 second runs

| | Two-stage observers | | Benchmark observers | |
|---|---|---|---|---|
| | SS-UKF | EKF | SS-UKF | EKF |
| CPU time | 0.4985 | 1.6102 | 0.7667 | 1.7814 |

### 3.2.2 Test case II: excavator

Excavators are engineering vehicles widely employed in earthworks, like digging of holes, foundations, material handling, demolitions, mining, and so on. An excavator consists of a cabin for the operator on a rotating platform sat atop a wheeled or tracked system for movement, and of a robotic arm, which in turn comprises a boom, a stick, and a bucket, moved by means of hydraulic actuators.

In order to perform the required working tasks, the excavation forces (or digging forces) developed by the excavator actuators must be greater than the resistive ones offered by the soil to be excavated. This means that very high forces, able to tip over the excavator, can be involved during working tasks. One way to forecast the excavator tipping over, and hence to improve human operator's safety, is to know the amount of digging forces. Unfortunately, such forces are very difficult, if not impossible to measure, therefore models and strategies to estimate the digging forces become necessary. Additionally, in such manipulators, force estimation could be useful, for instance, in the development of unmanned excavators, for which there is a growing interest for the sake of work efficiency and safety of operators.

Following the approach proposed in this chapter the digging forces have been estimated by means of the implementation of two partially coupled observers. The kinematic observer, reconstructs the kinematic state of the excavator (i.e. the angular position, velocity and acceleration of each link) exploiting the excavator kinematic constraint equations, and measured kinematic quantities, i.e. both the angular displacements $\theta_b$, $\theta_s$, and $\theta_{bc}$ of the boom, stick and bucket, and the accelerations denoted $\mathbf{a}_1$, $\mathbf{a}_2$, $\mathbf{a}_3$ in Fig 3.7.

Figure 3.7 shows the planar kinematic scheme with three degrees of free-

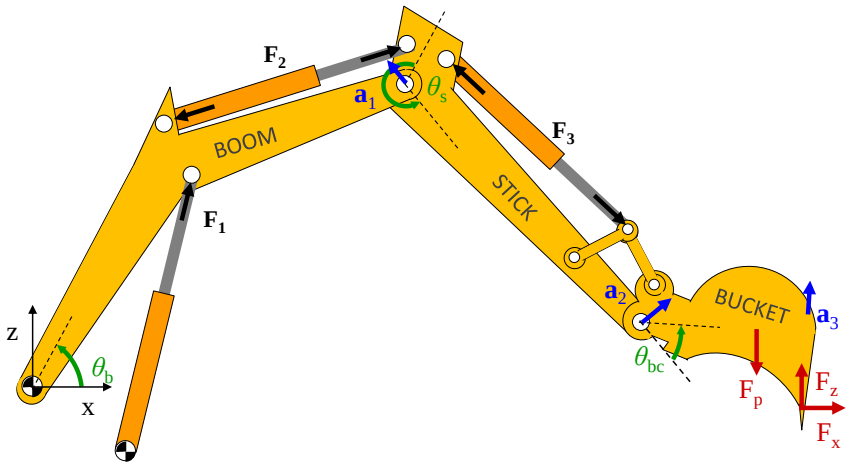


Figure 3.7: Excavator scheme

dom employed. The swing displacement of the excavator, i.e. the rotation about the vertical axis, is instead neglected. Such an hypothesis is not restrictive for representing meaningful operative conditions, since during digging tasks no swing motion is usually imposed by the operator driving the excavator. The force observer estimates the digging forces and the payload mass by employing an augmented excavator dynamic model, the estimated kinematic state, and the measured actuation forces ($\mathbf{F}_1$, $\mathbf{F}_2$, and $\mathbf{F}_3$).

All the signals used in the estimation process have been exported from the excavator simulator developed at the "Mechanical Engineering Laboratory" (LIM) of the University of La Coruña [48]. The excavator has been modeled in such a software by using more than 200 natural coordinates. Conversely it is modeled through the three independent coordinates in the observer. Noise has been also added to all the signals provided by the simulator, that represent the measured signals, in order to simulate the use of actual transducers. In particular, Gaussian noises have been generated with amplitudes of, respectively, 0.0063 rad for the encoders (corresponding to the resolution of a 1000 ppr encoder), 0.03 $m/s^2$ for the accelerometers (corresponding to the resolution provided by an accelerometer with sensitivity $10^{-3}$ $V/ms^{-2}$, whose signal is converted by a 16-bit ADC with input range +/-10 V ), 12.3 kN for the force sensors (corresponding to 0.25 % of the full scale of a 500 ton load cell).

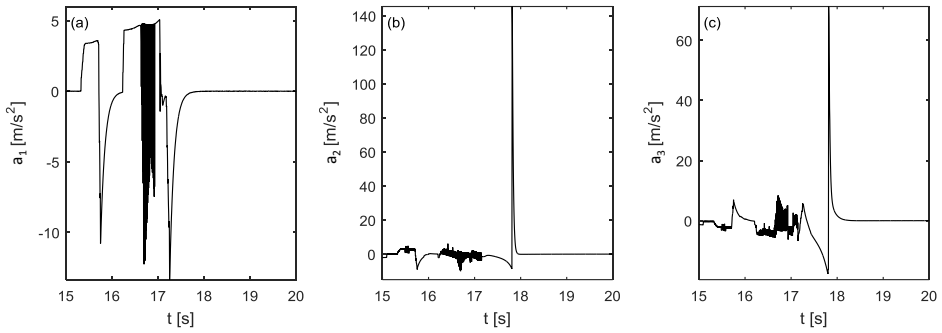


Figure 3.8: Kinematic observer inputs: from left to right, linear acceleration of boom, stick, and bucket

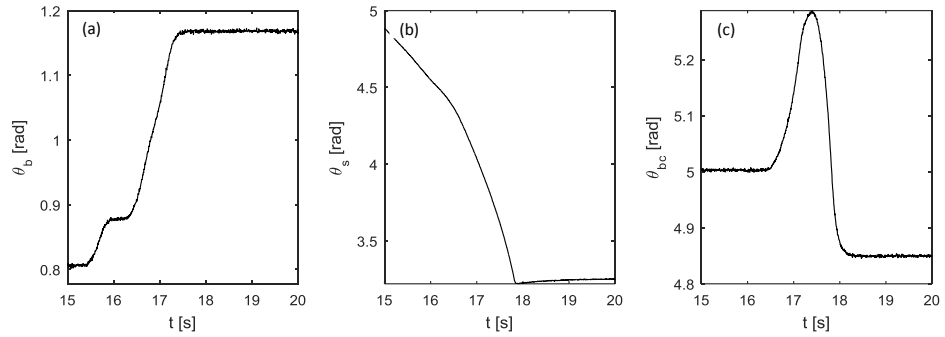


Figure 3.9: Kinematic observer outputs: from left to right, angular position of boom, stick, and bucket

The signals used as the inputs and the outputs of the kinematic observer are respectively plotted in Fig. 3.8 and Fig. 3.9. Just a sample portion of each signal is shown in all the figures, in order to represent more clearly what happens in the interaction phase between the bucket and the ground. Similar results are obtained in the whole simulated test.

The angular velocities and accelerations of the three links estimated through the kinematic observer are plotted respectively in Figs. 3.10 and 3.11, together with the actual values of the same variables, as delivered by the simulator. Since estimated and actual values are almost perfectly overlapped, the estimation error is also shown in the same figures. The results are highly satisfactory and confirm the good performances of the kinematic observer with another challenging test case.

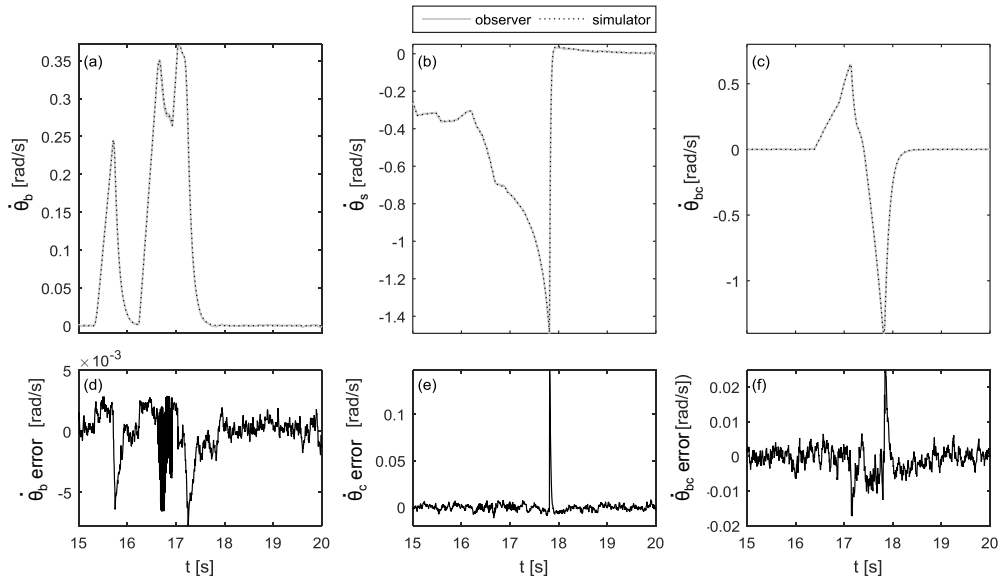


Figure 3.10: Estimated boom (a), stick (b), and bucket (c) angular velocities. Boom (d), stick (e), and bucket (f) velocity estimation errors

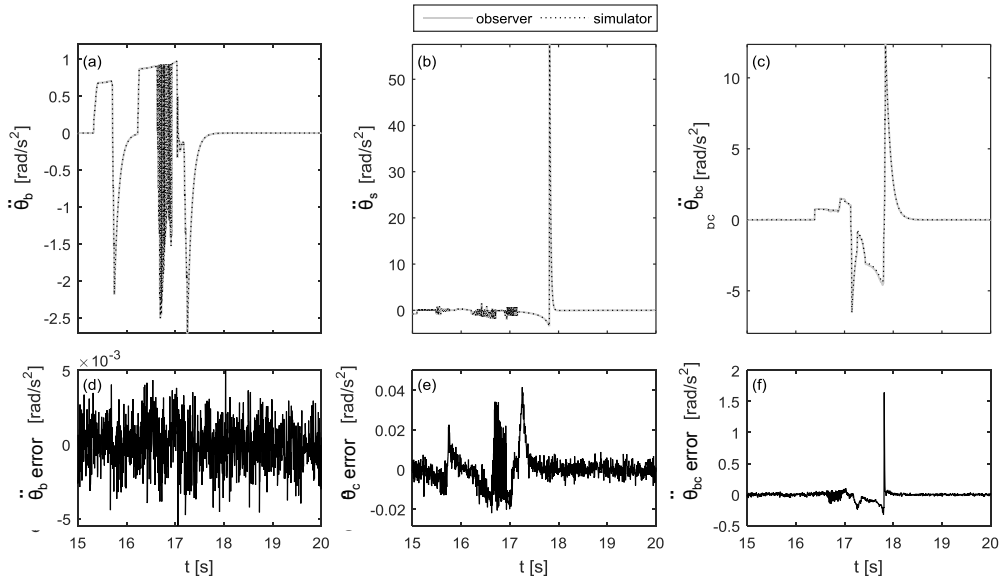


Figure 3.11: Estimated boom (a), stick (b), and bucket (c) angular accelerations. Boom (d), stick (e), and bucket (f) acceleration estimation errors

As for the force estimation, the force observer carries out the state prediction using the augmented dynamic model, in accordance with the theory in Section 3.1.2. In particular the actuation forces are modeled by means of the inverse dynamic model, which makes them depend nonlinearly on the kinematic state, and on digging and payload forces. In contrast, the digging forces are modeled by means of a first-order lowpass filter with 10 Hz cutoff frequency rather than by the typical and easier random walk model. This choice of model is reasonably justified by for two reasons:

- Excavators have very low bandwidth actuators, as it is evident from the fast Fourier transform of the actuation forces supplied by the simulator plotted in Fig. 3.12. In contrast, random walk models assume infinite-bandwidth; therefore they are not suitable to represent correctly the dynamics of excavators.

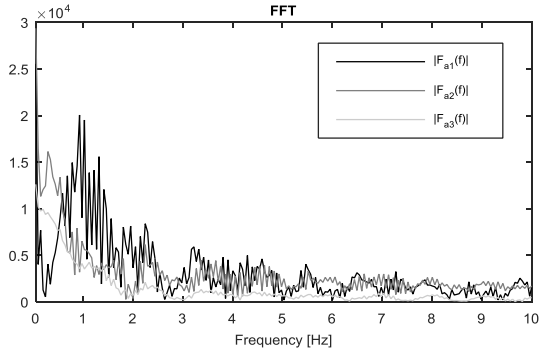


Figure 3.12: Fast Fourier transform of the hydraulic actuation forces

- Force estimation is strongly affected by errors on kinematic estimates, because of the high masses involved. Hence, small estimation errors of the accelerations may lead to high errors in the estimation of the inertial forces, and hence of the external unknown forces. It is worth noticing that acceleration estimations have been obtained introducing a numerical derivation scheme in the observer through the prediction-correction approach described in Section 2.2.1.2. Although this approach partially compensates for the error due to the approximate

nature of such a model, some high frequency errors still remain uncompensated. Therefore, the use of a band-limited model of the forces filters such high-frequency errors, which are not propagated into the force estimation.

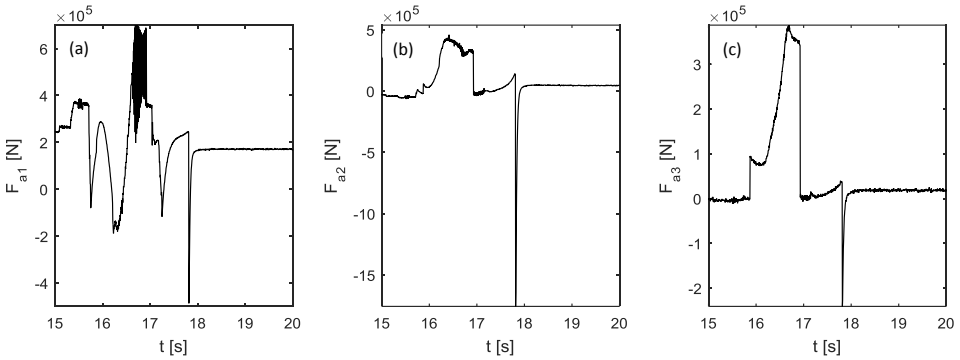


Figure 3.13: Force observer outputs: force of the first (a), the second (b), and the third (c) hydraulic actuator

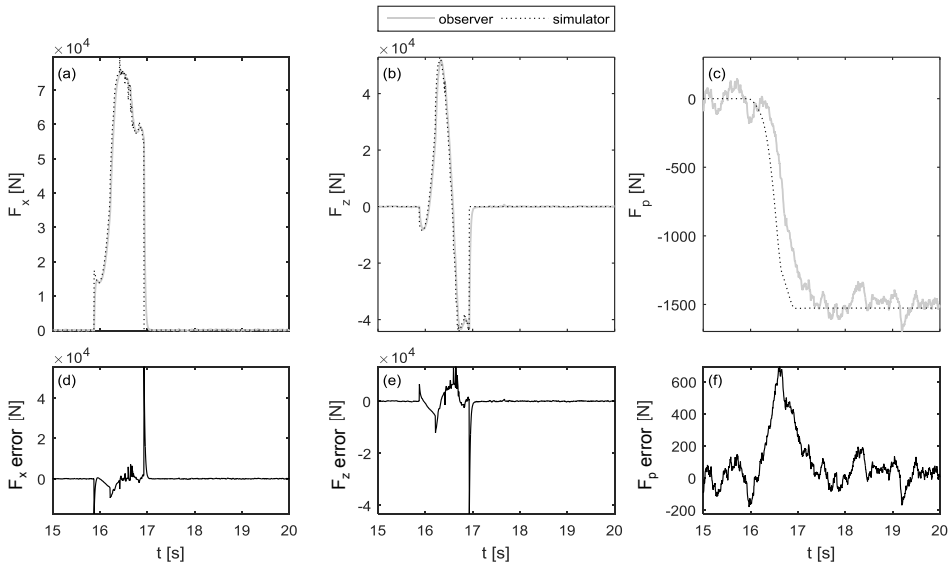


Figure 3.14: Estimated digging forces in x-direction (a) and in z-direction (b), payload force (c). Estimation errors on digging force in x-direction (d), z-direction (e), and payload force (f)

The actuation forces employed in the correction phase of the force observer are plotted in Fig. 3.13. Figure 3.14 shows the estimates provided by such an observer and the corresponding actual values provided by the simulator. The same figure also shows the difference between the estimated values and the actual ones. The peaks in the error diagrams (Figs. 3.14 (d) and (e)) are due to observer delay, however, apart from such a small delay, the estimates of digging forces are very accurate. The payload force estimate is instead less accurate, but still acceptable to have a qualitative information on the amount of the material in the bucket. Such a less accurate estimate of the payload force is due to the small magnitude of such a force, which is comparable with the measurement errors on hydraulic actuator forces. One way to improve the payload force estimation (if higher accuracy was needed) could be carrying out the estimation in static conditions and with no interactions between bucket and ground.

Overall, the results are very satisfactory, which, once again, confirms the effectiveness of the two-stage approach presented in this chapter.

Finally, it is worth noticing the time taken to estimate all the state variable is 9.27 s. Such a time is much shorter than the time simulated (20 s), which should guarantee real time capabilities for the estimator.

## 3.3 Chapter summary

A new approach for improving the accuracy of state and unknown external force estimations has been presented. The proposed approach aims at reducing model uncertainties and getting more accurate estimates by decoupling the overall estimation process into two stages.

The state variables and the unknown forces are estimated through two observes running simultaneously and only partially coupled: a first-stage kinematic observer and a second-stage force observer.

The first one estimates the augmented kinematic state of a MBS (i.e. positions, velocities and accelerations in a number equal to the dofs) just employing kinematic constraint equations and measurements of kinematic quantities. Therefore, it does not require the knowledge of dynamic equations of motion and external forces.

In contrast, the second-stage force observer uses the estimated kinematic state to estimate the external forces. Thus, just the force observer depends on the kinematic observer and no vice-versa. This is a great advantage of the proposed approach over the existing ones, since the estimation of the kinematic state is not affected by the dynamic model and the external forces (which are always more uncertain than the geometrical parameters involved in the kinematic observer), and hence the impact of model uncertainty in the estimation accuracy is considerably reduced. Additionally, the proposed approach takes full advantage of the considerable benefits of state (and state derivative) estimation based on kinematic constraint equations in MBS with rigid links and negligible joint clearance.

Therefore, besides allowing more accurate estimates of the external forces compared to traditional single-stage dynamic observers, the two-stage approach prevents the drift in state estimate due to the effect of unknown forces, and therefore ensures bounded errors in the estimates.

The numerical assessment has been provided through both simulated closed-chain, single-dof mechanism (a slider-crank mechanism) and open chain, three-dof manipulator (an excavator arm). Estimations have been performed through the EKF and, as a representative example of UKF, the SS-UKF.

The comparison between the results obtained with the two-stage approach and the benchmark one (i.e. the traditional single-stage observer, which estimates the kinematic states and the unknown forces by means of a dynamic model augmented with random walks to represent the external forces) corroborates all the theoretical considerations, and highlights that more accurate estimates of both the state and the unknown input forces can be obtained through the two-stage approach.

Finally, the small CPU time taken by the proposed approach represents an additional benefit of it and assure its implementability in real-time systems.

# Chapter 4

# Modeling of flexible-link MBSs

The theory presented in the previous chapters, has been based on the assumption that all the bodies of a MBS satisfy the rigid body constraint, such an assumption is satisfied in most of industrial systems. However, there are some cases in which elastic deformations play an important role. This is the case of lightweight manipulators or high-speed machinery. Lightweight manipulators, compared with their rigid-arm counterparts, have some advantages. Among them, one should recall less material and power consumption, less weight, smaller actuators and improved maneuverability. Unfortunately, the dynamics of such systems is influenced by the elastic deformations. Hence, the formulations presented in the preceding chapters, both in terms of modeling and estimation approach, cannot be applied.

Dynamic modeling of flexible manipulators is a very challenging task, due to the strong coupling between the gross motion and the fine motion (vibration) of the links. This problem has received great attention in the past decade and numerous contributions can be found in literature as well as thorough reviews of the early studies [49–54].

Flexible-link MBSs are continuous dynamical systems characterized by an infinite number of degrees of freedom and are governed by nonlinear coupled, ordinary and partial differential equations. In order to solve such equations some approximations are need. First of all, the continuous equations are discretized by means of either lumped parameter [55, 56], assumed modes [57–59], or finite elements methods [59–61]. Models based on the lumped parameter approximations are the simplest ones for analysis purpose, but

manipulators are modeled as spring and mass systems, hence they do often not yield sufficiently accurate results. Assumed mode methods represent link flexibility by truncated finite modal series in terms of eigenvectors and time-varying mode amplitudes. In particular, modes with higher eigenfrequencies are usually neglected. Finite element methods are the most widespread. Basically, they model the flexible links of a mechanism as discrete systems with a finite number of elastic degrees of freedom, and assume that the total motion of the system be the superposition of a large amplitude rigid-body motion and a small-amplitude elastic deformation. Finite-element-based and fully coupled dynamic models (i.e. taking into account the mutual influence between rigid-body motion and vibration) for multi-body mechanisms have been proposed for instance in [62–65].

The finite-element-based method most used is the floating frame of reference (FFR) [50, 64]. FFR method requires two sets of coordinates: a set of rigid body variables, expressing the large nonlinear overall motion and characterizing the moving frame of each link; and a set of elastic variables, that expresses the deformation of each link with respect to its moving frame. Dynamic models obtained with the FFR methods are systems of coupled differential equations. However, the constraint equations (which express the connection between the joints and the adjacent flexible links) are coupled too, this means that they do not have an immediate and easy formulation [66,67]. Such a coupling is due to the definition of the constraints in the global coordinate system, therefore they are introduced into the dynamic equations by means of nonlinear algebraic constraint equations, depending both on the elastic deformations and on the rigid motion of the floating frames.

Conversely, the method based on an equivalent rigid-link system (ERLS) [65, 66, 68, 69], allows decoupling the kinematic constraint equations of the ERLS, which express the gross motion, from the compatibility equations of the elastic displacements at the joints [66]. Moreover, this method leads, on the one hand, to fully coupled dynamic models and, on the other hand, it allows easily identifying and neglecting the inertia coupling terms having negligible contributions with respect to the others.

The modeling of flexible-link MBSs based on the ERLS is briefly described in Section 4.1, being the approach used in this dissertation to model a rather

complex example of flexible-link planar manipulator with hybrid topology (Section 4.2). In this Chapter, the manipulator model based on the ERLS is also refined by matching experimental and numerical modes (Sections 4.3 and 4.4).

## 4.1 Model based on the ERLS

The following discrete model of a chain of flexible bodies, developed according to the ERLS approach, makes use of finite element techniques to express virtual displacements and real accelerations. The equations of motion are obtained by direct application of the principle of virtual work.

### 4.1.1 Kinematics

Each flexible link of a chain is subdivided into finite elements, and the following kinematic definitions are adopted for the $i^{th}$ element and with respect to a common fixed reference frame {X; Y; Z}:

- $\mathbf{r}_i$ and $\mathbf{u}_i$ represent, respectively, the nodal positions and displacements of the $i^{th}$ element of the ERLS;
- $\mathbf{b}_i$ is the position vector of the nodes belonging to the $i^{th}$ element; mathematically we can write

$$\mathbf{b}_i = \mathbf{r}_i + \mathbf{u}_i \tag{4.1}$$

- $\mathbf{w}_i$ and $\mathbf{v}_i$ contain, respectively, the vector of the positions and of the displacements of a generic point of the $i^{th}$ element;
- $\mathbf{p}_i$ is the position vector of a generic point of the $i^{th}$ element; mathematically we can write

$$\mathbf{p}_i = \mathbf{w}_i + \mathbf{v}_i \tag{4.2}$$

A local reference frame $\{x_i;\ y_i;\ z_i\}$ is defined for each element: these local coordinate systems follow the motion of the ERLS, whose position is defined by the generalized coordinates contained in the vector $\mathbf{q}$. The kinematic definitions are schematically summarized in Fig.4.1: a planar case is considered

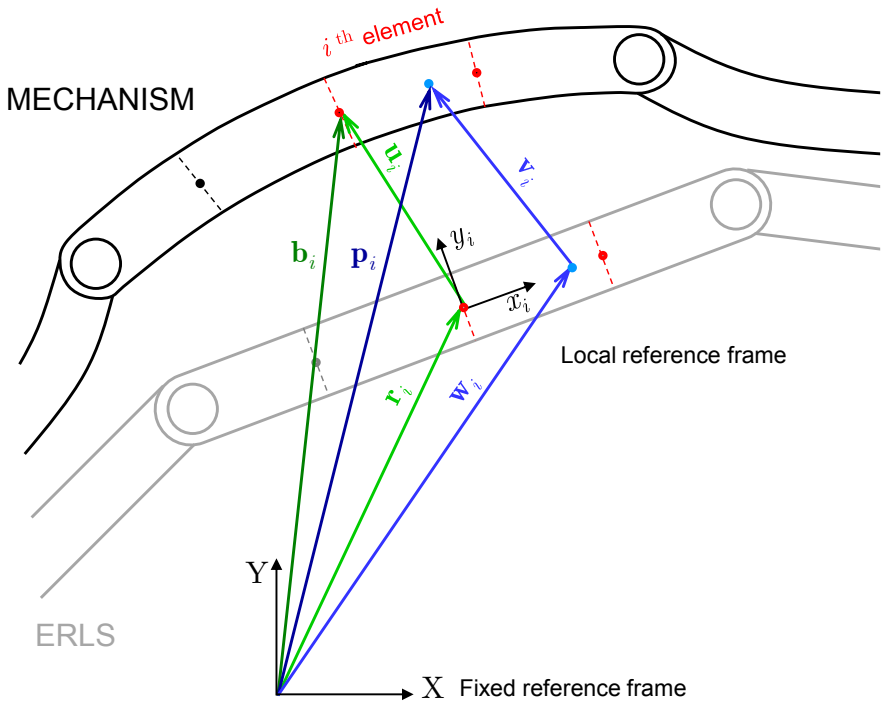


Figure 4.1: Kinematic definitions

to simplify the drawing. The position and orientation of every local system can be uniquely determined through the ERLS kinematics. The position of the ERLS, as well as its velocity and acceleration, can be defined according to the ordinary rules adopted for analyzing rigid-link mechanisms. In particular, by making use of the sensitivity coefficient concept, it is possible to write

$$d\mathbf{r} = \mathbf{S}(\mathbf{q})d\mathbf{q} \tag{4.3}$$

$$\dot{\mathbf{r}} = \mathbf{S}(\mathbf{q})\dot{\mathbf{q}} \tag{4.4}$$

$$\ddot{\mathbf{r}} = \mathbf{S}(\mathbf{q})\ddot{\mathbf{q}} + \dot{\mathbf{S}}(\mathbf{q},\dot{\mathbf{q}})\dot{\mathbf{q}} = \mathbf{S}(\mathbf{q})\ddot{\mathbf{q}} + \left(\sum_k \dot{\mathbf{q}}_k \frac{\partial \mathbf{S}}{\partial \mathbf{q}_k}\right)\dot{\mathbf{q}} \tag{4.5}$$

where $\mathbf{S}(\mathbf{q})$ is the matrix of sensitivity coefficients for all the nodes of the ERLS, and vector $\mathbf{r}$ contains the positions of all the nodes of the ERLS ($\mathbf{r}_i$ is a subset of $\mathbf{r}$). If, accordingly, the elastic coordinates of all the nodes

are grouped into unique vectors, after differentiating Eq.4.1 and employing Eq.4.3, the infinitesimal nodal displacement vector $d\mathbf{b}$ becomes

$$d\mathbf{b} = \left[\begin{array}{c:c} \mathbf{I} & \mathbf{S} \end{array}\right] \left[\begin{array}{c} d\mathbf{u} \\ \hdashline d\mathbf{q} \end{array}\right] \tag{4.6}$$

where $\mathbf{I}$ is the identity matrix. The coefficient matrix of the equation above is not square. If $n_q$ is the dimension of the vector $\mathbf{q}$ of the ERLS generalized coordinates and $n_{u'}$ is the number of the elastic dofs contained in vector $\mathbf{u}$; then $[\ \mathbf{I} \vdots \mathbf{S}\ ]$ has $n_q$ rows and $n_q + n_{u'}$ columns. Therefore, a given configuration of infinitesimal nodal displacements $d\mathbf{b}$ corresponds to more sets of infinitesimal variations $[\ d\mathbf{u}^{\mathrm{T}} \vdots d\mathbf{q}^{\mathrm{T}}\ ]$ of the generalized coordinates of the system. In order to overcome such an issue, the coefficient matrix must be square, which can be obtained forcing to zero $n_q$ elements of $d\mathbf{u}$. As a consequence, the position of the ERLS with respect to the actual deformed mechanism is defined univocally. If $d\mathbf{u}$ is partitioned into its independent part ($d\mathbf{u}_{in} \in \mathbb{R}^{n_u = n_{u'} - n_q}$) and into its zeroed part ($d\mathbf{u}_0 \in \mathbb{R}^{n_q}$), and if $\mathbf{S}$ is accordingly partitioned, Eq.4.6 can be rewritten as:

$$d\mathbf{b} = \left[\begin{array}{c:c} \mathbf{I} & \mathbf{S}_{in} \\ \hdashline \mathbf{0} & \mathbf{S}_0 \end{array}\right] \left[\begin{array}{c} d\mathbf{u}_{in} \\ \hdashline d\mathbf{q} \end{array}\right] \tag{4.7}$$

As underlined in [65], a correct ERLS definition requires not only a non-singular square matrix of coefficients of Eq.4.7, but also ERLS generalized coordinates chosen so as to avoid encountering singular configuration during the motion.

The virtual displacement and the real acceleration of a generic point within an element are computed through the finite element theory. Such quantities are to be determined to apply the principle of virtual work. Let $\mathbf{N}_i(x_i, y_i, z_i)$ be the shape function matrix of the $i^{th}$ element, Eq. 4.2 can be rewritten as

$$\mathbf{p}_i = \mathbf{w}_i + \mathbf{R}_i(\mathbf{q})\mathbf{N}_i(x_i, y_i, z_i)\mathbf{T}_i(\mathbf{q})\mathbf{u}_i \tag{4.8}$$

$\mathbf{N}_i$ is typically defined in the local reference frame of the $i^{th}$ element, so two matrices are introduced in Eq.4.8 to perform coordinate transformations: $\mathbf{T}_i$ ($\mathbf{q}$) is a block-diagonal matrix expressing the transformation from the global

reference frame to the local one of the $i^{th}$ element; $\mathbf{R}_i(\mathbf{q})$ is a matrix expressing the local-to-global transformation. Virtual displacements ($\delta\mathbf{p}_i$) can be obtained by taking variations of Eq.4.8. Both the virtual elastic displacements of the nodes ($\delta\mathbf{u}_i$) and the virtual displacements of the generalized coordinates ($\delta\mathbf{q}$) are considered. Additionally, the shape function matrices can be employed not only to compute elastic displacements inside the elements but also to represent rigid-body displacements, this is due to the requirement of completeness (which the elements must satisfy to encounter monotonic convergence to the exact solution as the number of elements is increased). The following equation is obtained from the complete expression of ($\delta\mathbf{p}_i$) by neglecting the terms with the lowest order of magnitude and is employed to interpolate virtual displacements from

$$\delta\mathbf{p}_i = \mathbf{R}_i(\mathbf{q})\mathbf{N}_i(x_i, y_i, z_i)\mathbf{T}_i(\mathbf{q})\delta\mathbf{r}_i + \mathbf{R}_i(\mathbf{q})\mathbf{N}_i(x_i, y_i, z_i)\mathbf{T}_i(\mathbf{q})\delta\mathbf{u}_i \tag{4.9}$$

An analogous reasoning allows obtaining the following simplified expression of the acceleration from the complete expression of $\ddot{\mathbf{p}}_i$:

$$\begin{aligned}\ddot{\mathbf{p}}_i =& \mathbf{R}_i(\mathbf{q})\mathbf{N}_i(x_i, y_i, z_i)\mathbf{T}_i(\mathbf{q})\ddot{\mathbf{r}}_i + \mathbf{R}_i(\mathbf{q})\mathbf{N}_i(x_i, y_i, z_i)\mathbf{T}_i(\mathbf{q})\ddot{\mathbf{u}}_i + \\ &+ 2\left[\dot{\mathbf{R}}_i(\mathbf{q})\mathbf{N}_i(x_i, y_i, z_i)\mathbf{T}_i(\mathbf{q}) + \mathbf{R}_i(\mathbf{q})\mathbf{N}_i(x_i, y_i, z_i)\dot{\mathbf{T}}_i)(\mathbf{q})\right]\dot{\mathbf{u}}_i\end{aligned} \tag{4.10}$$

The complete expressions of $\delta\mathbf{p}_i$ and $\ddot{\mathbf{p}}_i$ and an investigation of their negligible terms are reported in [65]. The expressions of real and virtual strains also have to be computed to apply the principle of virtual work, since they allow estimating the elastic contributions to the total virtual work. By letting $\mathbf{B}_i(x_i, y_i, z_i)$ denote the strain-displacement matrix, in the local moving frame

$$\epsilon_i = \mathbf{B}_i(x_i, y_i, z_i)\mathbf{T}_i\mathbf{u}_i \tag{4.11}$$

$$\delta\epsilon_i = \mathbf{B}_i(x_i, y_i, z_i)\delta\mathbf{T}_i\mathbf{u}_i + \mathbf{B}_i(x_i, y_i, z_i)\mathbf{T}_i\delta\mathbf{u}_i \tag{4.12}$$

### 4.1.2 Motion equations

The governing equations of motion are obtained by expressing the dynamic equilibrium of the system through the principle of virtual work. For an undamped system, the virtual works due to the inertial, elastic and external

forces should be considered. The total virtual work can be computed summing up the elemental contributions:

$$\underbrace{\sum_i \int_{v_i} \delta \mathbf{p}_i^{\mathrm{T}} \ddot{p}_i \rho_i dv}_{-\delta \mathbf{W}^{inertial}} + \underbrace{\sum_i \int_{v_i} \delta \epsilon_i^{\mathrm{T}} \mathbf{D}_i \epsilon_i dv}_{-\delta \mathbf{W}^{elastic}} = \underbrace{\sum_i \int_{v_i} \delta \mathbf{p}_i^{\mathrm{T}} \mathbf{g} \rho_i dv + (\delta \mathbf{u}^{\mathrm{T}} \delta \mathbf{r}^{\mathrm{T}}) \mathbf{f}}_{+\delta \mathbf{W}^{external}} \tag{4.13}$$

where $v_i$ denotes the $i^{th}$ element volume, $\rho_i$ is the mass density for the element, $\mathbf{D}_i$ is the stress- strain matrix, $\mathbf{g}$ is the gravity acceleration vector, $\mathbf{f}$ is the vector of the concentrated external forces and torques applied to all the nodes of the model, and the virtual displacements $\delta\mathbf{u}$ and $\delta\mathbf{r}$ refer to all the nodes of the model. Invoking the virtual displacement theory, Eq.4.13 can be split into two independent equation as

$$\sum_i \delta \mathbf{u}_i^{\mathrm{T}} \mathbf{M}_i \left( \ddot{\mathbf{r}}_i + \ddot{\mathbf{u}}_i \right) + 2 \sum_i \delta \mathbf{u}_i^{\mathrm{T}} \mathbf{M}_{Gi} \dot{\mathbf{u}}_i + \sum_i \delta \mathbf{u}_i^{\mathrm{T}} \mathbf{K}_i \mathbf{u}_i = \sum_i \delta \mathbf{u}_i^{\mathrm{T}} \mathbf{f}_{gi} + \delta \mathbf{u}^{\mathrm{T}} \mathbf{f} \tag{4.14}$$

$$\sum_i \delta \mathbf{r}_i^{\mathrm{T}} \mathbf{M}_i \left( \ddot{\mathbf{r}}_i + \ddot{\mathbf{u}}_i \right) + +2 \sum_i \delta \mathbf{r}_i^{\mathrm{T}} \mathbf{M}_{Gi} \dot{\mathbf{u}}_i + \sum_i \mathbf{u}_i^{\mathrm{T}} \delta \mathbf{\Phi}_i \mathbf{K}_i \mathbf{u}_i = \sum_i \delta \mathbf{r}_i^{\mathrm{T}} \mathbf{f}_{gi} + \delta \mathbf{r}^{\mathrm{T}} \mathbf{f} \tag{4.15}$$

where the Eqs.4.9-4.12 are employed and the following definitions, described in detail in [65], are introduced for the $i^{th}$ element:

$$\int_{v_i} \mathbf{T}_i^{\mathrm{T}} \mathbf{N}_i^{\mathrm{T}} \mathbf{R}_i^{\mathrm{T}} \mathbf{R}_i \mathbf{N}_i \mathbf{T}_i \rho_i dv = \mathbf{M}_i \tag{4.16}$$

$$\int_{v_i} \mathbf{T}_i^{\mathrm{T}} \mathbf{B}_i^{\mathrm{T}} \mathbf{D}_i^{\mathrm{T}} \mathbf{B}_i \mathbf{T}_i dv = \mathbf{K}_i \tag{4.17}$$

$$\int_{v_i} \mathbf{T}_i^{\mathrm{T}} \mathbf{N}_i^{\mathrm{T}} \mathbf{R}_i^{\mathrm{T}} \mathbf{g} \rho_i dv = \mathbf{f}_{gi} \tag{4.18}$$

$$\int_{v_i} \left( \mathbf{T}_i^{\mathrm{T}} \mathbf{N}_i^{\mathrm{T}} \mathbf{R}_i^{\mathrm{T}} \dot{\mathbf{R}}_i \mathbf{N}_i \mathbf{T}_i + \mathbf{T}_i^{\mathrm{T}} \mathbf{N}_i^{\mathrm{T}} \mathbf{R}_i^{\mathrm{T}} \mathbf{R}_i \mathbf{N}_i \dot{\mathbf{T}}_i \right) \rho_i dv = \mathbf{M}_{Gi} \tag{4.19}$$

$$\delta \mathbf{T}_i^{\mathrm{T}} = \delta \mathbf{\Phi}_i \mathbf{T}_i^{\mathrm{T}} \tag{4.20}$$

When the elastic displacements are small in comparison with the link dimensions, the term $\sum_i \mathbf{u}_i^{\mathrm{T}} \delta \mathbf{\Phi}_i \mathbf{K}_i \mathbf{u}_i$ of Eq.4.15 becomes negligible, because its

order of magnitude is much smaller than that of the other terms. Therefore, if Eq.4.3 is employed to express the ERLS virtual displacements by means of the sensitivity coefficient matrix, and if unit virtual displacements are imposed, the following expressions holds in terms of assembled matrices and vectors:

$$\mathbf{M}(\ddot{\mathbf{r}} + \ddot{\mathbf{u}}) + (2\mathbf{M}_G + \mathbf{C})\dot{\mathbf{u}} + \mathbf{K}\mathbf{u} = \mathbf{f}_g + \mathbf{f} \tag{4.21}$$

$$\mathbf{S}^{\mathrm{T}}\mathbf{M}(\ddot{\mathbf{r}} + \ddot{\mathbf{u}}) + \mathbf{S}^{\mathrm{T}}(2\mathbf{M}_G + \mathbf{C})\dot{\mathbf{u}} = \mathbf{S}^{\mathrm{T}}(\mathbf{f}_g + \mathbf{f}) \tag{4.22}$$

where matrix $\mathbf{C}$ is damping matrix defined by means of the Rayleigh coefficients $\alpha$ and $\beta$ multiplying the mass and the stiffness matrix ($\mathbf{C} = \alpha\mathbf{M}+\beta\mathbf{K}$), such a matrix has been introduced to take into account damping forces. Finally, by making use of Eq. 4.5, Eqs.4.21 and 4.22 can be grouped together and rearranged in matrix form as

$$\begin{bmatrix} \mathbf{M}_{in} & (\mathbf{MS})_{in} \\ (\mathbf{S}^{\mathrm{T}}\mathbf{M})_{in} & \mathbf{S}^{\mathrm{T}}\mathbf{MS} \end{bmatrix} \begin{bmatrix} \ddot{\mathbf{u}}_{in} \\ \ddot{\mathbf{q}} \end{bmatrix} + \begin{bmatrix} 2\mathbf{M}_{Gin} + \mathbf{C}_{in} & (\mathbf{M}\dot{\mathbf{S}})_{in} \\ (\mathbf{S}^{\mathrm{T}}(2\mathbf{M}_G + \mathbf{C}))_{in} & \mathbf{S}^{\mathrm{T}}\mathbf{M}\dot{\mathbf{S}} \end{bmatrix} \begin{bmatrix} \dot{\mathbf{u}}_{in} \\ \dot{\mathbf{q}} \end{bmatrix} + \begin{bmatrix} \mathbf{K}_{in} & \mathbf{0} \\ \mathbf{0} & \mathbf{0} \end{bmatrix} \begin{bmatrix} \mathbf{u}_{in} \\ \mathbf{q} \end{bmatrix} = \begin{bmatrix} \mathbf{M}_{in} & \mathbf{I} \\ (\mathbf{S}^{\mathrm{T}}\mathbf{M})_{in} & \mathbf{S}^{\mathrm{T}} \end{bmatrix} \begin{bmatrix} \mathbf{g} \\ \mathbf{f} \end{bmatrix} \tag{4.23}$$

Equation 4.23 only includes the nodal elastic displacements which are not forced to zero, and the corresponding matrix elements. Inertia coupling between the accelerations of the ERLS generalized coordinates and the elastic accelerations is accounted for through the elements of the submatrices $(\mathbf{MS})_{in}$ and $(\mathbf{S}^{\mathrm{T}}\mathbf{M})_{in}$ Hence, the mutual influence between rigid-body motion and vibration is taken into consideration: the dynamic behaviour of the ERLS is not independent from vibration and vice versa.

## 4.2 Modeling of a flexible three-dof manipulator with hybrid topology

The equations of motion above are derived for general mechanisms and elements. In this dissertation they have been employed to develop a finite element computer code for the dynamic analysis and simulation of a planar


Figure 4.2: Planar, flexible, three-dof manipulator with hybrid topology

manipulator with flexible links and hybrid topology driven by three motors. A picture of a laboratory prototype of such a manipulator is shown in Fig. 4.2. The mechanism consists of five rods with circular cross-sections made of Aluminum Anticorodal (Young's modulus 69 GPa, mass density 2700 kg/m$^3$). The geometric and inertial parameters of the links are listed in Tab. 4.1. The links are connected to each other by mens of revolute joints, created by means of double ball bearings with negligible clearance and friction losses, inserted in Aluminum housings. The mechanism has an hybrid topology, indeed links 1, 2, 3 and 4 are connected in a closed kinematic chain, while links 4 and 5 are connected in an open kinematic chain.

Links 1,2 and 5 are driven by three brushless motors. In particular an Indramat MKD090 motor drives the crank corresponding to link 2, while an Indramat MKD041 motor drive the crank corresponding to link 1. Rod 5 is driven by a Parker SMB40-035, ultra-compact brushless motor. A list of the chief technical features of the three motors is shown in Tab. 4.2.

The angular positions of motor shafts MKD041 and MKD090, are delivered directly by the motor drives with a resolution of $1.534{\cdot}10^{-3}$ degrees, instead the Parker is equipped with a 4096 ppr absolute encoder *Heiden-*

Table 4.1: Geometric and inertial parameters of the links

| **Links** | **Length [m]** | **Diameter [mm]** | **Masses [Kg]** |
|---|---|---|---|
| AB | 0.5 | 30 | 1.052 |
| AD | 0.85 | 30 | 1.596 |
| BC | 0.85 | 16 | 0.444 |
| CE | 1.2 | 24 | 1.343 |
| EF | 0.282 | 20 | 0.190 |

Table 4.2: Motor datasheets

| **Parametro** | **MKD041** | **MKD090** | **SMB40** |
|---|---|---|---|
| Nominal torque [Nm] | 2.9 | 13.5 | 0.35 |
| Peak torque [Nm] | 13.6 | 59.4 | 0.9 |
| Nominal speed [rpm] | 6000 | 3200 | 5000 |
| Nominal current [A] | 8.2 | 14.4 | 0.9 |
| Torque constant [Nm/A] | 0.4 | 1.05 | 0.277 |
| Back electromotive force constant [Vs/rad] | 0.3466 | 0.86899 | 0.16 |
| Armature resistance [Ω] | 1.8 | 1.2 | 10.9 |
| Armature inductance [mH] | 5 | 10.1 | 37 |
| Moment of inertia [kgcm$^2$] | 1.7 | 43 | 0.035 |

Table 4.3: Torque meter data

| **Motors** | $\mathbf{T_n}$ **[Nm]** | $\mathbf{K_t}$ **[Nm/∘]** | **J [kgm$^2$]** |
|---|---|---|---|
| MKDO41 | 200 | 20 | $2.6{\cdot}10^{-3}$ |
| MKDO90 | 500 | 52 | $9{\cdot}10^{-3}$ |

*hain eqn 1125.* Half-bridge strain gages are located on links 1, 2, 3 and 4, at half their length. The signals produced by the strain gage bridges are acquired and conditioned by a HBM carrier (12-bit ADC/DAC). Additionally, the mechanism is instrumented with two torque meters, measuring the torques of the Indramat motors. The nominal torque $T_n$, torsional stiffness $K_t$, and the moment of inertia J of each torque meters are listed in Tab. 4.3

with reference to the motor with which they are connected.

It is worth noticing the mechanism lies on the vertical plane. In order to no overload the motors and to avoid their thermal shutdown, manipulator has two contrast springs DIM T32880 (as you can see in Fig. 4.2), which help motors, in particular the MKD090 motor, to counteract the weight forces. The springs are made in carbon steel *EN10270-1 SH* and are prestressed. Spring design and specifications are, respectively, shown in Fig. 4.3 and Tab. 4.4. The two springs are connected in parallel, so the total rate is double with respect to the one in Tab. 4.4, and the total elastic force exerted by springs is: $F_{el} = -T - 2c(L - L0)$.

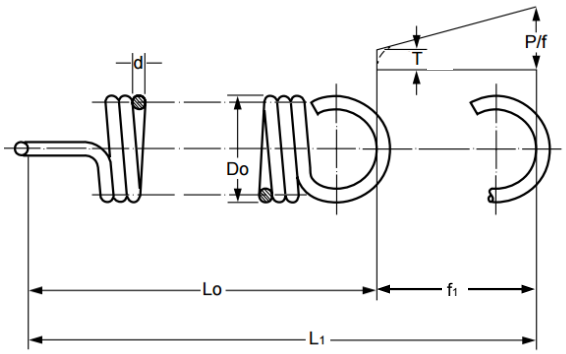


Figure 4.3: Spring design

Table 4.4: Spring datasheet

| | | | |
|---|---|---|---|
| Number of coils | Ns | [-] | 40 |
| Wire diameter | d | [mm] | 3.2 |
| Outside diameter | $D_0$ | [mm] | 36 |
| Free length | $L_0$ | [mm] | 179 |
| Maximum extended length | $L_1$ | [mm] | 453 |
| Load at $L_1$ | $P_1$ | [N] | 243 |
| Deflection at $L_1$ | $f_1$ | [mm] | 274 |
| Rate | c | [N/m] | 760 |
| Initial tension | T | [N] | 34.7 |
| Weight | M | [kg] | 0.2 |

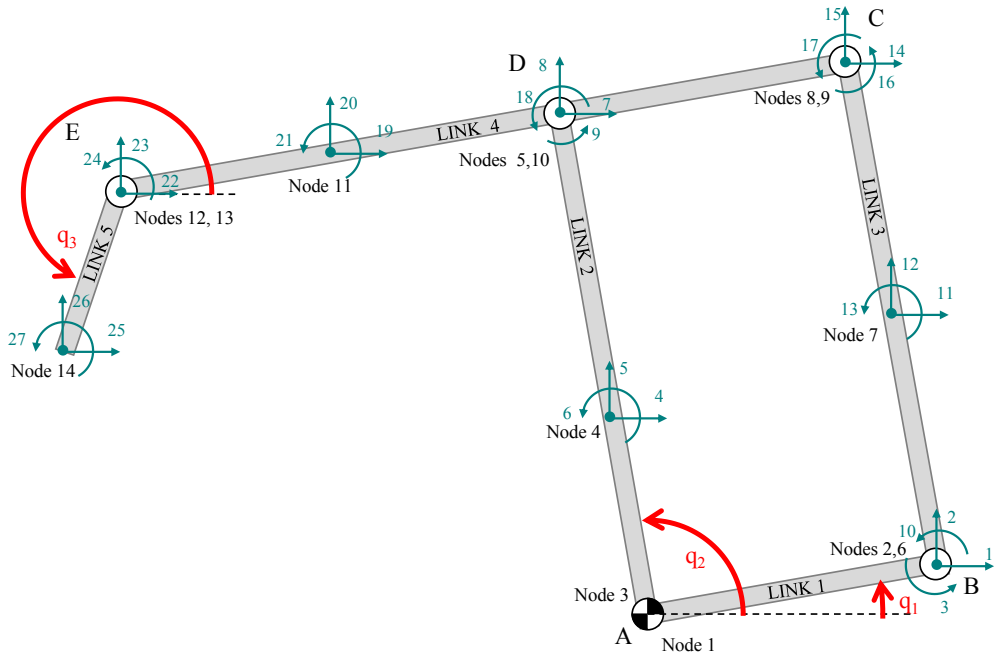


Figure 4.4: Finite element model of the studied mechanism

Figure 4.4 illustrates the finite element model of the mechanism. All the links have been modeled with classical two-node and six-degree-of freedom beam elements, in particular the model comprises nine beam elements. The shape function ($\mathbf{N}_i$), mass ($\mathbf{M}_i$), and stiffness ($\mathbf{K}_i$) matrices for each $i^{\text{th}}$ two dimensional Euler beam elements are common knowledge and are not recalled here. The Coriolis matrix ($\mathbf{M}_{g_i}$) can be effectively computed through the antisymmetric inertia matrix described in [69].

A SW program code has been written using Matlab in order to infer a complete FE model of the manipulator based on the ERLS approach. Through the implemented code it is possible to simulate the dynamic response of such a flexible mechanism and to monitor all the state variables, torque/force inputs and measured output.

Lumped masses are used to account for the moving joints B, C, D and E whose moments of inertia are neglected because of their small dimensions. Two nodal inertia at joints A (nodes 1,3) accounts for the inertia of the brakes,

and the rotors of the brushless motors, as well as of the torque meters and of the coupling devices and bearings. Another nodal inertia in E accounts for the rotor of third motor. In Tab. 4.5 are listed all the lumped parameters in each node.

Fig. 4.4 also shows the 27 elastic dofs of the model, as well as the generalized coordinates $\mathbf{q} = \left\{ q_1 \quad q_2 \quad q_3 \right\}^T$ of the ERLS. The dynamic model has therefore 30 dofs. This is the minimum size of the model capable to correctly represent the dynamics of the systems, experimentally identified through an experimental modal analysis illustrated in the next Section.

The elastic dofs forced to zero to define the position of the ERLS with respect to the deformed mechanism are the angular positions of the actuated links. This definition of the ERLS meets the requirements defined in the previous section for a correct ERLS definition.

Table 4.5: Lumped masses and inertia

| **Nodes** | **Lumped masses [kg]** | **Inertia [kgm$^2$]** |
|---|---|---|
| 1 | 7.644 | 0.013 |
| 2 | 0.392 | 0 |
| 3 | 9.517 | 0.0229 |
| 4 | 0.4 | 0 |
| 5 | 0.648 | 0 |
| 6 | 0.671 | 0 |
| 7 | 0 | 0 |
| 8 | 0.383 | 0 |
| 9 | 0.658 | 0 |
| 10 | 0.308 | 0 |
| 11 | 0 | 0 |
| 12 | 1.537 | 0 |
| 13 | 0.095 | 0.0015 |
| 14 | 0.046 | 0 |

## 4.3 Experimental modal analysis

In order to verify the accuracy and correctness of the dynamic model developed an experimental modal analysis has been carried out. Indeed, an experimental modal analysis provides a dynamic characterization of systems under real mechanical conditions (actual constraints, cabling, etc...). In particular an impact analysis has been carried out. A series of frequency response functions (FRF) (i.e. system response per unit force over the frequency range of interest) have been measured at various geometric locations using an instrumented impact hammer to supply an input force, while the responses have been measured in the x, and y directions with accelerometers. In particular, the frequency range of interest has been set coherently with motor bandwidth, i.e. 0-180 Hz. The analysis has been carried out posing the manipulator in an equilibrium configuration. So it was possible to leave the motor brakes and to study the free evolution of the system. The measurement chain consists in:

- 5 accelerometers, whose specifications are listed in Tab. 4.6;
- an instrumented impact hammer *PCB*® *ModallyTuned*® 086C03 with teflon tip;
- a frontend system *LMS SCADAS Recorder* (max input ±10 V, ADC 24 bit);
- a modal software *LMS Test.Lab Impact Testing 11B*, with tools *Geometry, Modal Analysis, PolyMAX Modal Analysis*

The impact setup defined for the test is described in Tab. 4.7.

In order to determine the mode shapes of the manipulator during the post-processing, it has been necessary to define a manipulator geometry through "drive points" by the software tool *LMS Test.Lab Impact Testing 11B Geometry*. Each measure must be related to a drive point. The number of points, to be employed, and hence the "resolution" of geometrical model, depend on the highest frequency mode shape to be determined. The geometry adopted for such an analysis is shown in Fig. 4.5, it has 22 points, which

Table 4.6: Accelerometer employed

| Manufacturer | Model | Typology | Sensitivity [mV/g ] |
|---|---|---|---|
| Endevco | 27AM1-100 10203 | ICP | 102.4 |
| Dytran | 3136A1945 | ICP | 100 |
| PCB | 3741D4HB30G | Full bridge DC | 66.7 |
| Brüel & Kjaer | 4508 | ICP | 9.78 |
| | | X-triaxial ICP | 93.5 |
| Brüel & Kjaer | 4506B | Y-triaxial ICP | 94 |
| | | Z-triaxial ICP | 98 |

Table 4.7: Impact test settings

| | | |
|---|---|---|
| **Acquisition setting** | | |
| Sample frequency | 2048 | [Hz] |
| Frequency resolution | 0.06 | [Hz] |
| Acquisition time | 16 | [s] |
| **Triggering** | | |
| Trigger level | 5.72 | [N] |
| Pretrigger | 0.01 | [s] |
| **Windowing** | | |
| Input | Uniform | |
| Response | Exponential | Decay 90% |
| **Measurement averages** | | 3 |

is a good compromise between accuracy at high frequencies and number of driving points.

A total of 315 FRFs has been acquired, all such acquisitions are summarized in the experimental frequency response matrix shown in Fig. 4.6. Directions indicated in Fig. 4.6 are referred to the local reference systems of each link, plotted in Fig. 4.5. Each entry of the frequency response matrix corresponds to an FRF obtaining as an average of three measurements. As a representative example of such entries, Figs. 4.7 and 4.8 show respectively the $2^{\text{nd}}$ and $7^{\text{th}}$ row of the matrix in Fig. 4.6.

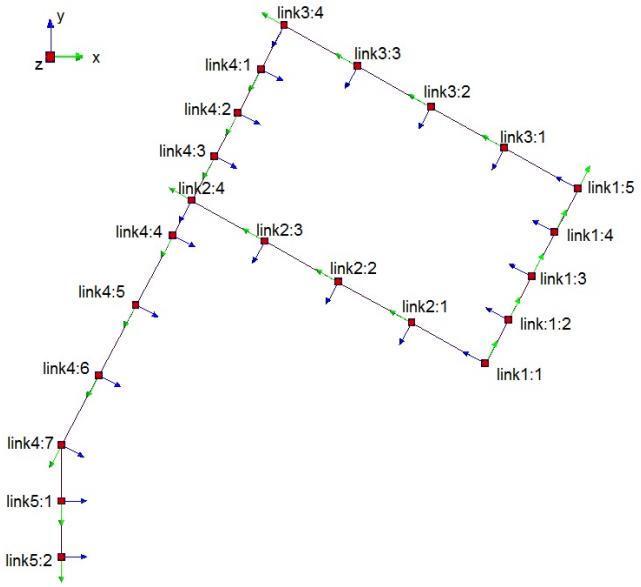


Figure 4.5: Manipulator geometry created by the GUI of *LMS Test.Lab 11B*

| | INPUT | link1:2 | link1:3 | link1:4 | link2:1 | link2:3 | link2:4 | link3:1 | link3:2 | link3:4 | link4:1 | link4:2 | link4:3 | link4:5 | link4:6 | link4:7 |
|---|---|---|---|---|---|---|---|---|---|---|---|---|---|---|---|---|
| OUTPUT | Dir | Y | Y | Y | Y | Y | Y | Y | Y | Y | Y | Y | Y | Y | Y | Y |
| link1:2 | Y | -\+ | -\+ | -\+ | -\+ | -\+ | -\+ | -\+ | -\+ | -\+ | -\- | -\- | -\- | -\- | -\- | -\- |
| link1:3 | Y | +\+ | +\+ | +\- | +\+ | +\+ | +\+ | +\+ | +\+ | +\+ | +\+ | +\+ | +\+ | +\- | +\- | +\+ |
| link1:4 | Y | +\+ | +\- | +\+ | +\+ | +\+ | +\+ | +\+ | +\+ | +\+ | +\+ | +\- | +\+ | +\- | +\- | +\+ |
| link1:5 | Y | -\+ | -\+ | -\+ | -\+ | -\+ | -\+ | -\- | -\+ | -\+ | -\+ | -\+ | -\+ | -\- | -\- | -\- |
| link2:1 | Y | +\+ | +\+ | +\+ | +\+ | +\+ | +\+ | +\- | +\+ | +\+ | +\+ | +\+ | +\+ | +\- | +\- | +\- |
| link2:2 | Y | +\+ | +\+ | +\- | +\+ | +\+ | +\+ | +\+ | +\+ | +\+ | +\+ | +\+ | +\+ | +\- | +\- | +\+ |
| link2:3 | Y | +\+ | +\- | +\+ | +\+ | +\+ | +\+ | +\+ | +\+ | +\+ | +\+ | +\- | +\+ | +\- | +\- | +\+ |
| link2:4 | Y | +\+ | +\+ | +\+ | +\+ | +\+ | +\+ | +\+ | +\+ | +\+ | +\- | +\- | +\- | +\- | +\- | +\- |
| link3:1 | Y | -\+ | -\+ | -\+ | -\+ | -\+ | -\+ | -\- | -\+ | -\+ | -\+ | -\+ | -\+ | -\- | -\- | -\- |
| link3:2 | Y | -\+ | -\- | -\+ | -\+ | -\+ | -\+ | -\+ | -\+ | -\+ | -\+ | -\- | -\+ | -\- | -\- | -\+ |
| link3:3 | Y | -\+ | -\+ | -\- | -\+ | -\+ | -\+ | -\+ | -\+ | -\+ | -\+ | -\+ | -\+ | -\- | -\- | -\+ |
| link3:4 | X | +\- | +\- | +\- | +\+ | +\+ | +\+ | +\+ | +\+ | +\+ | +\+ | +\+ | +\+ | +\+ | +\+ | +\+ |
| link4:1 | Y | -\+ | -\+ | -\+ | -\+ | -\+ | -\+ | -\+ | -\+ | -\+ | -\- | -\- | -\- | -\- | -\- | -\- |
| link4:2 | Y | -\+ | -\- | -\+ | -\+ | -\+ | -\+ | -\+ | -\+ | -\+ | -\+ | -\- | -\+ | -\- | -\- | -\+ |
| link4:3 | Y | -\+ | -\+ | -\+ | -\+ | -\+ | -\+ | -\+ | -\+ | -\+ | -\- | -\- | -\- | -\- | -\- | -\- |
| link4:4 | Y | -\+ | -\+ | -\- | -\+ | -\+ | -\+ | -\+ | -\+ | -\+ | -\+ | -\+ | -\+ | -\- | -\- | -\+ |
| link4:5 | Y | -\+ | -\+ | -\+ | -\+ | -\+ | -\+ | -\- | -\+ | -\+ | -\+ | -\+ | -\+ | -\- | -\- | -\- |
| link4:6 | Y | +\- | +\- | +\- | +\+ | +\+ | +\+ | +\+ | +\+ | +\+ | +\+ | +\+ | +\+ | +\+ | +\+ | +\+ |
| link4:7 | X | -\+ | -\+ | -\+ | -\+ | -\+ | -\+ | -\- | -\+ | -\+ | -\+ | -\+ | -\+ | -\- | -\- | -\- |
| link4:7 | Y | -\+ | -\+ | -\+ | -\+ | -\+ | -\+ | -\- | -\+ | -\+ | -\+ | -\+ | -\+ | -\- | -\- | -\- |
| link5:2 | Y | -\- | -\- | -\- | -\+ | -\+ | -\+ | -\+ | -\+ | -\+ | -\+ | -\+ | -\+ | -\+ | -\+ | -\+ |

Figure 4.6: Frequency response matrix

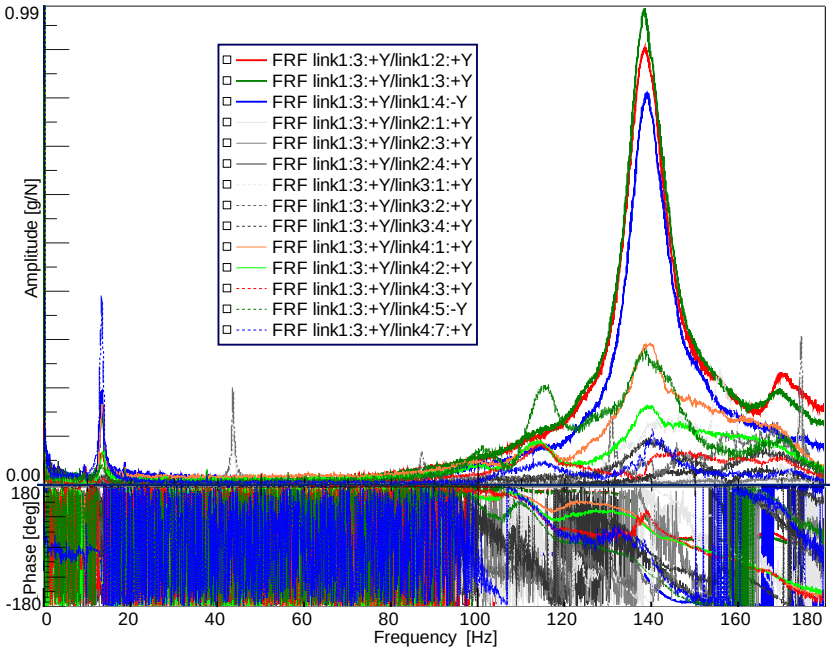


Figure 4.7: 2nd row of the frequency response matrix

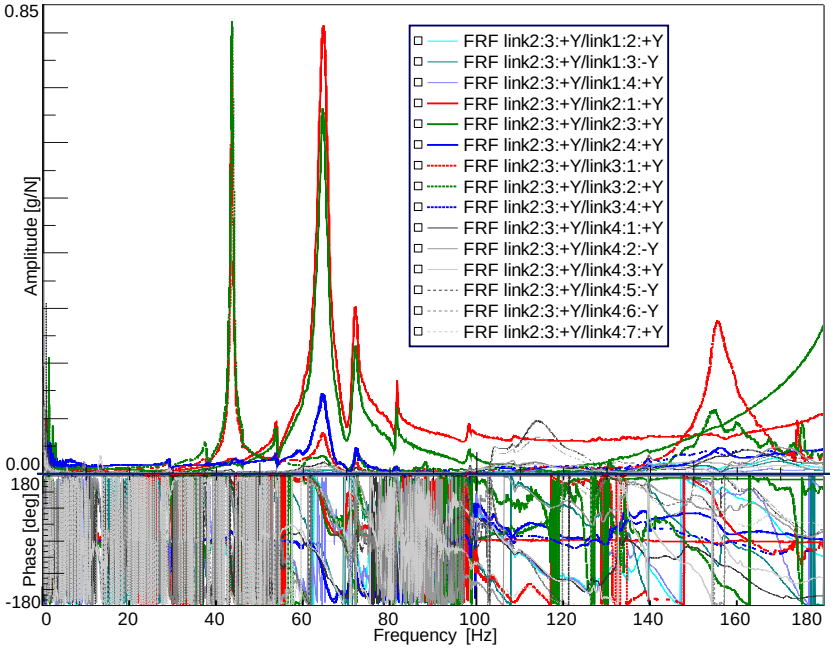


Figure 4.8: 7th row of the frequency response matrix

Data have been processed using the tool *PolyMAX* of *LMS Test.Lab 11B*, yielding the experimental vibration modes of the manipulator.

Figures from 4.9 to 4.15 compare the vibration modes experimentally identified (on the left) to the ones computed by the analytical model (on right) through a local linearization.

The Figures prove a good agreement between the analytical modal shapes and the experimental ones, up to the $7^{\text{th}}$ vibrational mode, and hence in the entire frequency range of interest (0-180 Hz). Conversely, some discrepancies are presented between the analytical eigenfrequencies and the experimental ones. Nonetheless the availability of such a detailed comparison among analytical and experimental modal proprieties has allowed performing a modal updating. The outcomes of such an activity are presented in the next Section.

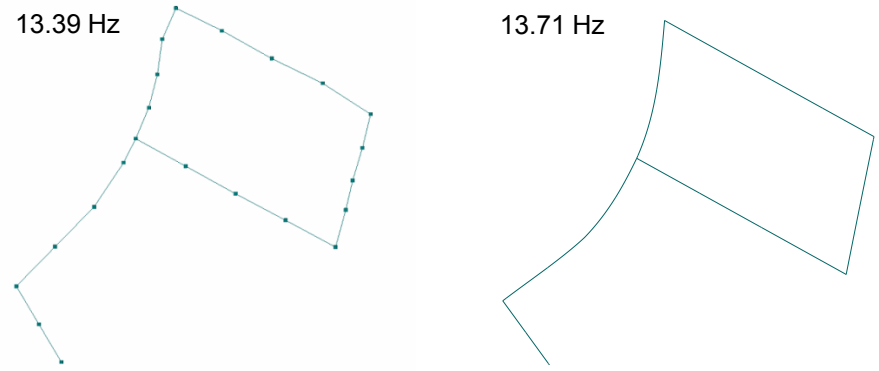


Figure 4.9: First vibration mode: experimental (left), analytical (right)

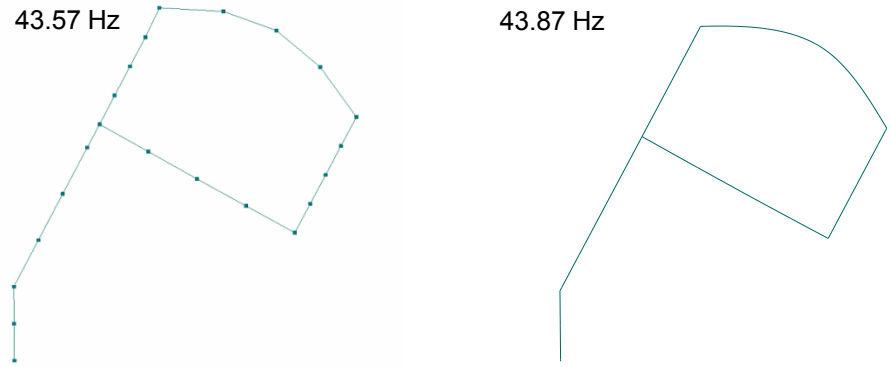


Figure 4.10: Second vibration mode: experimental (left), analytical (right)

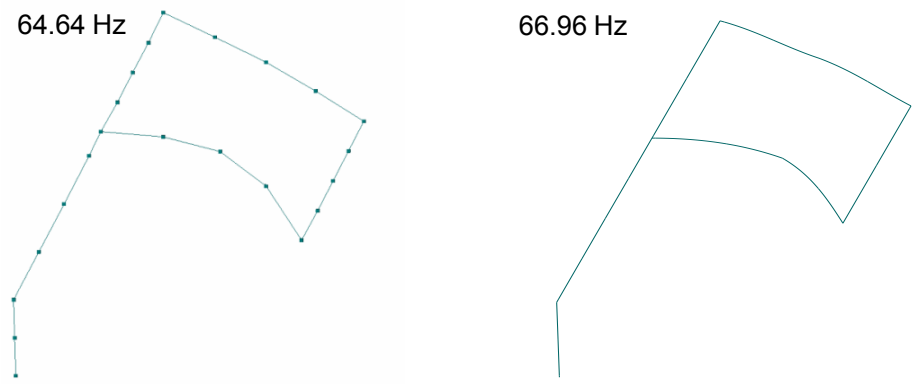


Figure 4.11: Third vibration mode: experimental (left), analytical (right)

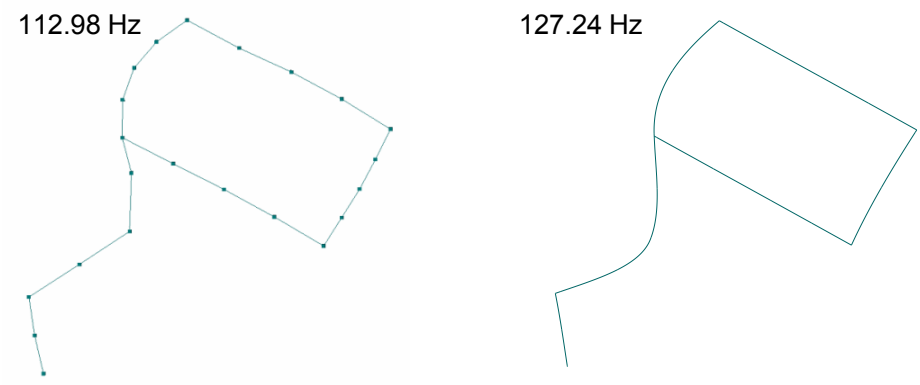


Figure 4.12: Fourth vibration mode: experimental (left), analytical (right)

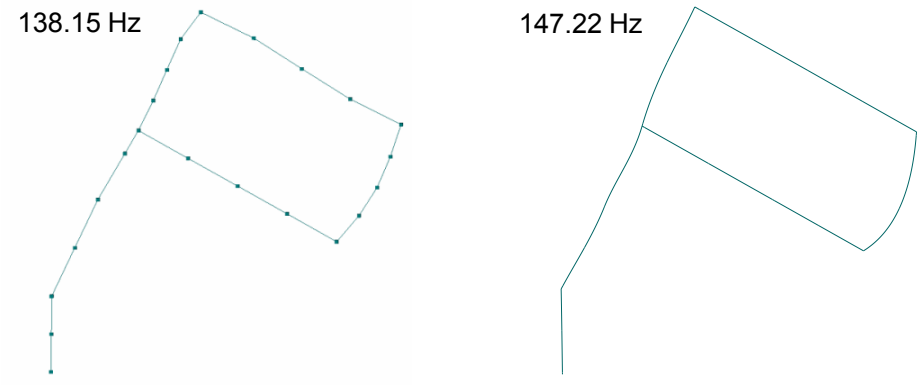


Figure 4.13: Fifth vibration mode: experimental (left), analytical (right)

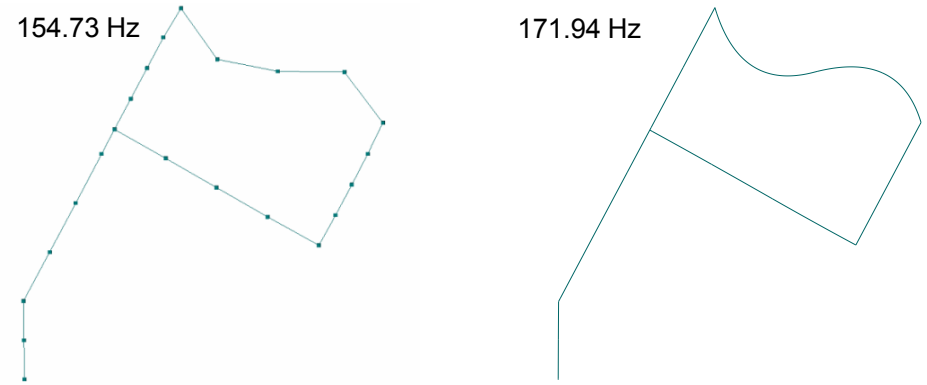


Figure 4.14: Sixth vibration mode: experimental (left), analytical (right)

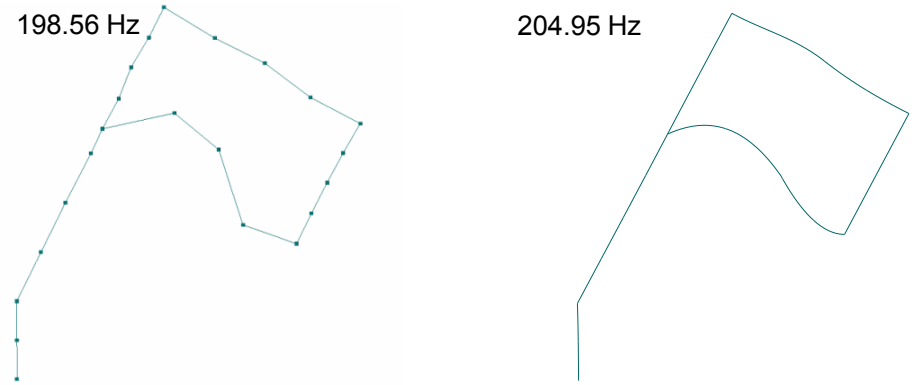


Figure 4.15: Seventh vibration mode: experimental (left), analytical (right)

## 4.4 Model updating

As a matter of fact, FE methods are not able to predict the dynamic responses of systems with adequate accuracy whenever the inertial and elastic properties of the links are not correctly tuned in the model. In order to overcome such an issue, model updating techniques [70] have been developed to correct FE model parameters to feature a set of experimental measurements.

Model updating techniques are usually classified into two categories: direct techniques (also denoted non-iterative or one-step) and iterative techniques (or parametric) [71]. Direct techniques find the solution to model updating problem in just a single step. However they often produce results with no physical meaning, as well as they are not robust to measurement noise.

In contrast, iterative techniques compute the updated parameters through an objective function that represents the differences between analytical and experimental results. Iterative techniques are usually computationally more expensive than the other and may be affect by the presence of local optimal solution if the updating problem is formulated as a non-convex optimization problem. The iterative methods are becoming however more popular, since they preserve physical meaning of the updated parameters, and their solutions can take advantage of the advanced numerical techniques and toolboxes for optimization ( [72, 73]).

A wide literature has been developed for model updating in structures or simple mechanical systems. In contrast, the issue of model updating in multibody systems is often neglected, and in particular experimental and systematic approaches are rarely addressed.

In this Section a model updating procedure for dynamic models based on the ERLS is developed and validated through the manipulator described in Section 4.2 and the experimental modal analysis carried out in Section 4.3. The proposed technique starts from the model linearization, that allows applying modal analysis, by carefully tackling several peculiarities of the model of flexible-link MBSs. Afterwards, an iterative technique based on convex optimization is proposed, to ensure convergence to global optimal solution while accounting for bounds on the feasible values of the updated inertial and elastic parameters.

### 4.4.1 Numerical approach to model updating

Although the dynamics of flexible link mechanisms and manipulators is nonlinear it is widely recognized that in the case of small deformations the accuracy of linearized models about operating points is usually very satisfactory to make their use successful in the synthesis of effective and stable control schemes. Linearized models, represented through ODEs, allow applying modal analysis. Hence, the model tuning made through the linearized model allow also tuning the nonlinear one.

By considering small displacement about a static equilibrium configuration, which is set by the equilibrium configuration of the ERLS $\mathbf{q_e}$, the

following linear model is obtained:

$$\begin{bmatrix} \mathbf{M} & \mathbf{MS} \\ \mathbf{S}^{\mathrm{T}}\mathbf{M} & \mathbf{S}^{\mathrm{T}}\mathbf{MS} \end{bmatrix}_{\mathbf{q}=\mathbf{q}_e} \begin{Bmatrix} \ddot{\mathbf{u}} \\ \ddot{\mathbf{q}} \end{Bmatrix} + \begin{bmatrix} \mathbf{C} & \mathbf{0} \\ \mathbf{S}^{\mathrm{T}}\mathbf{C} & \mathbf{0} \end{bmatrix}_{\mathbf{q}=\mathbf{q}_e} \begin{Bmatrix} \dot{\mathbf{u}} \\ \dot{\mathbf{q}} \end{Bmatrix} + \tag{4.24}$$

$$+ \begin{bmatrix} \mathbf{K} & \mathbf{0} \\ \mathbf{0} & -\left(\frac{d(\mathbf{S}^{\mathrm{T}}\mathbf{M})}{d\mathbf{q}} \otimes \mathbf{g} + \frac{d\mathbf{S}^{\mathrm{T}}}{d\mathbf{q}} \otimes \mathbf{v}\right) \end{bmatrix}_{\mathbf{q}=\mathbf{q}_e} \begin{Bmatrix} \mathbf{u} \\ \mathbf{q} = \end{Bmatrix} \begin{bmatrix} \mathbf{I} \\ \mathbf{S}^{\mathrm{T}} \end{bmatrix}_{\mathbf{q}=\mathbf{q}_e} \{\mathbf{v}\}$$

in Eq. 4.24, the matrices $\mathbf{M}$, $\mathbf{S}$, $\mathbf{K}$, $\mathbf{C}$, and the derivatives $d(\mathbf{S}^{\mathrm{T}}\mathbf{M})/d\mathbf{q}$, and $d\mathbf{S}^{\mathrm{T}}/d\mathbf{q}$ are computed about the equilibrium configuration. The term $(d\mathbf{S}^{\mathrm{T}}/d\mathbf{q}) \otimes \mathbf{v}$ represents the inner product of matrix $[\partial S_{i,1}/\partial q_j \ldots \partial S_{i,n}/\partial q_j]$ with vector $\mathbf{v}$ for all the subscripts $i$, $j$ (obvious extension to $(d(\mathbf{S}^{\mathrm{T}}\mathbf{M})/d\mathbf{q}) \otimes \mathbf{g}$.

Model updating should be performed by investigating the system in a stable equilibrium configuration. Therefore, gravity forces should be compensated whenever the mechanism lies in the vertical plane. The most suitable approach is to balance gravity force through tuned external springs, that cause asymptotic stability of the equilibrium point (if properly chosen in the design). Clearly, springs should be then included in the stiffness matrix of the model. In contrast the use of brakes, such as those of the actuators, modifies the boundary conditions by making the mechanism behave as a structure, and deletes in the model all the term representing the coupling between the ERLS and the elastic displacement. Therefore model updating may lead to less reliable results. It is worth noticing that the absence a of stable equilibrium would make the mechanism diverge from the initial configuration after the excitation, and therefore the hypothesis of the linearized model are not met.

#### 4.4.1.1 Size compatibility between FE model and measurements

As it often happens in model updating, the measured dofs are usually less than those included in the FE model of the system, due to the limited number of sensor used in the experimental measurement or to the presence of some inaccessible locations. Additionally, rotational dofs cannot be easily measured. Thus, the displacement vector of the FE MB model is not compatible

with the experimental data. In contrast, model updating requires one-to-one correspondence between the displacement vector of the MB model and the measured eigenvectors. This correspondence can be achieved by either reducing the FE model or by expanding the experimental results.

In this work, the use of coordinate expansion techniques is adopted. In particular, least-square curve fitting is employed to estimate effectively the unmeasured dofs, while filtering measurement noise. Fitting is based on the measurements of a redundant set of translational dofs, and the least-square regression of the measured displacements by taking advantage of the suitable polynomial interpolation functions. Once that the coefficients of the polynomial representing the translational displacement along the link have been computed, the estimation of the rotational dofs for the model nodes of interest is trivial.

The fitting procedure is applied to each single link of the system, or to just some part of the link whenever the number of measurements allows fitting in a narrow scale.

#### 4.4.1.2 Data representation from the ERLS reference frame to the physical one

A second relevant issue that should be accounted for to perform correct updating is the transformation of the measured eigenvectors from the reference adopted to measure the mode shapes, which is physical, to the notional one adopted in the ERLS model. Indeed, the displacement vector of the MB model based on the ERLS, and hence its eigenvectors, includes the elastic displacements with respect to the ERLS, and the displacement of the ERLS itself (see Section 4.1). In contrast, experimental measurements are defined with respect to the mechanism in its initial static configuration. Transformation should be therefore performed through the ERLS kinematic constraint equations:

$$\overline{\boldsymbol{\varphi}}_i = \boldsymbol{\varphi}_i + \boldsymbol{\Theta}(\mathbf{q}_e, \Delta\mathbf{q}) \tag{4.25}$$

$\overline{\boldsymbol{\varphi}}_i$ is the $i^{\text{th}}$ eigenvector in the model, $\boldsymbol{\varphi}_i$ is the related eigenvector in the physical frame (measured and then expanded, as in Section 4.4.1.1), and $\boldsymbol{\Theta}(\mathbf{q}_e, \Delta\mathbf{q})$ is the transformation representing the kinematic constraint equa-

tions. $\boldsymbol{\Theta}$ is a function of the ERLS equilibrium configuration assumed for linearizing the model, $\mathbf{q}_e$, and of the displacement of the ERLS when the system moves accordingly with such an eigenvector, denoted $\Delta\mathbf{q}$.

#### 4.4.1.3 Modelization of the updating parameters

Updating is performed on just the inertial and elastic parameters. In contrast, damping is neglected. Identification of the Rayleigh coefficients can be performed separately, through the well established methods. This simplifies the formulation of the eigenvalue problem by casting it as a first order problem and by using real eigenvectors and eigenvalues $(\omega_i^2,\ \boldsymbol{\varphi}_i)$, $i = 1, \ldots, n_{ex}$, where $n_{ex} \leq n$ is the number of measured experimental modes, $n$ is the number of model dofs, including both rigid and elastic quantities, and $\omega_i$ is the natural frequency of the mode whose shape is $\boldsymbol{\varphi}_i$.

Therefore, the system linearized model in Eq. 4.24 can be written in the usual form of an undamped vibrating system, represented through the mass $\mathbf{M}^N$ and the stiffness $\mathbf{K}^N$ matrices. Superscript $N$ has been introduced to denote the nominal, i.e. no updated, system matrices synthesized through nominal or theoretical inertial and elastic parameters. The nominal system matrices are updates by means of additive correction matrices $\Delta\mathbf{M} \in \mathbb{R}^{nxn}$ and $\Delta\mathbf{K} \in \mathbb{R}^{nxn}$. The topologies of such matrices are chosen on the basis of the parameters that can be modified in accordance with design constraints, and are hence specified at the design stage. The following representations are adopted for $\Delta\mathbf{M}$ and $\Delta\mathbf{K}$:

$$\Delta\mathbf{M} = \sum_{j=1}^{n_m} \Delta\mathbf{M}_j = \sum_{j=1}^{n_m} \left[\frac{\partial\mathbf{M}^N}{\partial m_j^N}\right] \Delta m_j \qquad \Delta\mathbf{K} = \sum_{k=1}^{n_k} \Delta\mathbf{K}_k = \sum_{k=1}^{n_k} \left[\frac{\partial\mathbf{K}^N}{\partial k_k^N}\right] \Delta k_k \tag{4.26}$$

where $n_j$ and $n_k$ denote the number of modifiable parameters in, respectively, the mass and stiffness matrices. $\Delta\mathbf{M}_j$ and $\Delta\mathbf{K}_k$ are the correction submatrices that define the location and type of model uncertainties and can be obtained as the first derivative of the nominal matrices with respect to the modifiable physical or geometrical model parameters $m_j^N$ or $k_k^N$. Each matrix is related to one of the uncertain parameter of the nominal model ($m_j^N$ or $k_k^N$), to be updated through the unknown additive corrections ($\Delta\mathbf{M}_j$

and $\Delta\mathbf{K}_k$). In practice, all the uncertain parameters of the actual system model is represented as the sum of the value of the nominal one and the modification, $m_j = m_j^N + \Delta m_j$ and $k_k = k_k^N + \Delta k_k$. The topology of $\Delta\mathbf{M}_j$ and $\Delta\mathbf{K}_k$ is imposed, so as to represent correctly the effect of the updated parameters on the different model dofs.

In order to improve the numerical conditioning of the problem, dimensionless corrections are employed, which represent the percentage modifications of the parameters of the nominal model:

$$\alpha_j = \frac{\Delta m_j}{m_j^N} \qquad \beta_k = \frac{\Delta k_k}{k_k^N} \tag{4.27}$$

All the quantities $\alpha_j$ and $\beta_k$, and hence all the updating parameters, are collected in the $(n_m+n_k)$-dimensional unknown vector $\boldsymbol{\chi} = \alpha_j, \quad \beta_k$. Finally the corrective matrices can be defined as follows, where the sub-matrices $\mathbf{A}_j$ and $\mathbf{B}_k$ have been introduced for brevity of notation.

$$\Delta\mathbf{M} = \sum_{j=1}^{n_m} \left[\frac{\partial \mathbf{M}^N}{\partial m_j^N}\right] \alpha_j := \sum_{j=1}^{n_m} \mathbf{A}_j \alpha_j \qquad \Delta\mathbf{K} = \sum_{k=1}^{n_k} \left[\frac{\partial \mathbf{K}^N}{\partial k_k^N}\right] \beta_k := \sum_{k=1}^{n_k} \mathbf{B}_k \beta_k \tag{4.28}$$

Matrix derivatives are constant whenever Young's modulus, mass density, nodal masses, nodal inertias, sectional area or lumped springs are to be updated, i.e. are collected in $m_j^N$ or $k_k^N$. In contrast, if $\alpha$ or $\beta$ represent the length of the beams, the derivatives are not constant, and iteration should be done in model updating. However, it is reasonable assuming the beam length as a known and exact parameter.

The correction of the model parameters should be, in practice, bounded. On the one hand, physical meaningful should be always ensured. On the other hand, unrealistic values due to the mathematical solution, although physically feasible, should be avoided. Hence, both lower ($\boldsymbol{\chi}_L$) and upper ($\boldsymbol{\chi}_U$) bounds should be defined, by defining a feasible set $\Gamma$ (where the inequality are element-wise)

$$\Gamma = \{\boldsymbol{\chi} \quad | \quad \boldsymbol{\chi}_L \leq \boldsymbol{\chi} \leq \boldsymbol{\chi}_U\} \tag{4.29}$$

#### 4.4.1.4 Model updating problem formulation

By defining the unknown mass and stiffness matrices of the $n$-dimensional modified system $\mathbf{M}^N + \Delta\mathbf{M}$ and $\mathbf{K}^N + \Delta\mathbf{K}$, having introduced the additive correction matrices $\Delta\mathbf{M}$ and $\Delta\mathbf{K}$, the following equation must hold for any measured eigenpair:

$$\mathbf{0} = \omega_i^2 \left[\mathbf{M}^N + \Delta\mathbf{M}\right] \boldsymbol{\varphi}_i - \left[\mathbf{K}^N + \Delta\mathbf{K}\right] \boldsymbol{\varphi}_i \tag{4.30}$$

By pre-multiplying by $\boldsymbol{\varphi}_i$, in order to obtain a scalar equation, and by introducing the definitions of the updating matrices given in Eq. 4.28, the eigenvalue problem can be written as:

$$0 = \boldsymbol{\varphi}_i^{\mathrm{T}} \left[\omega_i^2 \mathbf{M}^N - \mathbf{K}^N\right] \boldsymbol{\varphi}_i + \omega_i^2 \sum_{j=1}^{n_m} \boldsymbol{\varphi}_i^{\mathrm{T}} \mathbf{A}_j \boldsymbol{\varphi}_i \alpha_j - \sum_{j=1}^{n_k} \boldsymbol{\varphi}_i^{\mathrm{T}} \mathbf{B}_k \boldsymbol{\varphi}_i \beta_k - \tag{4.31}$$

Equation 4.31 represents a linear problem in the unknown $\{\alpha_j, \beta_k\}$,

$$0 = \mathbf{a}_i \boldsymbol{\chi} - b_i \tag{4.32}$$

where the known term is defined as $b_i = \boldsymbol{\varphi}_i^{\mathrm{T}} \left[\omega_i^2 \mathbf{M}^N - \mathbf{K}^N\right] \boldsymbol{\varphi}_i$, while $\mathbf{a}_i$ denotes the line vector collecting all the coefficients.

Since the parameters collected in $\boldsymbol{\chi}$ are constrained, and more conditions like the one in Eq. 4.32 should be simultaneously satisfied, the problem should be approximated as a norm minimization problem, where the residual of each eigenvalue problem can be weighed through the positive and scalar weight $w_i$:

$$\min \left\| \begin{bmatrix} w_1 \mathbf{a}_1 \\ \vdots \\ w_{n_e x} \mathbf{a}_{n_e x} \end{bmatrix} \boldsymbol{\chi} - \begin{Bmatrix} w_1 b_1 \\ \vdots \\ w_{n_e x} b_{n_e x} \end{Bmatrix} \right\|_2^2 \tag{4.33}$$

Weighing the equations has several justifications when dealing with flexible link MBSs. Besides giving less importance to those eigenpairs whose measurements are less reliable, the weights should take into account the frequency range of interest for the analysis.

In order to improve the numerical conditioning of the problem, preconditioning should be applied to obtain unitary condition number, by taking

advantage of the pseudo-inverse matrix (denoted with the superscript †):

$$\min \left\| \boldsymbol{\chi} - \begin{bmatrix} w_1 \mathbf{a}_1 \\ \vdots \\ w_{n_e x} \mathbf{a}_{n_e x} \end{bmatrix}^{\dagger} \begin{Bmatrix} w_1 b_1 \\ \vdots \\ w_{n_e x} b_{n_e x} \end{Bmatrix} \right\|_2^2 \tag{4.34}$$

Finally, regularization can be adopted to weigh the components of $\boldsymbol{\chi}$ suitably, i.e. to penalize the modifications of the model parameter selectively [74]. As a matter of fact, some parameters are much more uncertain than others, and therefore it is more desirable that updating will modify them. Hence, the term $\lambda \left\| \boldsymbol{\Omega\chi} \right\|_2^2$ is added to the norm minimization problem in Eq. 4.34. The scalar positive value $\lambda$ is the regularization parameter, trading between the cost of missing the eigenpair specifications and the cost of using large values of the design variables, $\left\| \boldsymbol{\Omega\chi} \right\|_2^2$. The positive-definite matrix $\boldsymbol{\Omega}$ is the regularization operator, and defines the relative weight of the different parameter updating. The model updating problem is therefore finally represented as the following constrained minimization problem, where it is defined vector $\mathbf{b}$, for shortness of notation $\mathbf{b} = \left[ w_i \mathbf{a}_i \right]^{\dagger} \left\{ w_i b_i \right\}$:

$$\begin{cases} \min_{\boldsymbol{\chi}} \left\| \begin{bmatrix} \mathbf{I} \\ \lambda \boldsymbol{\Omega} \end{bmatrix} \boldsymbol{\chi} - \begin{Bmatrix} \mathbf{b} \\ \mathbf{0} \end{Bmatrix} \right\|_2^2 \\ \boldsymbol{\chi} \in \Gamma \end{cases} \tag{4.35}$$

Being the problem a quadratic convex optimization problem, its solution is straightforward, and lead to global optimal results regardless of the initial guess adopted. Additionally, numerically reliable and efficient algorithms are available in commercial software for numerical computing. Finally, it is worth noticing that the proposed formulation is suitable for arbitrary mode normalization.

### 4.4.2 Experimental application

Model updating has been made only for the vibrational modes in the frequency range from 0 to 180 Hz. Indeed, the torque-loop bandwidth of the

three actuators driving the system is not greater than such an upper bound, and therefore vibrational modes with higher frequency cannot be controlled by any closed-loop control scheme, given this limitation of the actuators, and hence they are not of interest. Seven vibrational modes have been therefore identified.

#### 4.4.2.1 Statement model updating problem

The updating parameters have been selected judiciously as those more affected by uncertainty, such as the mass density of the links (which is assumed equal among all the links), the Young's modulus (which has been treated separately for each link, to compensate for local stiffening due to the kinematic joints), the spring lumped stiffness, the nodal inertias and masses. The feasible values have been constrained by reasonable bounds, which are not reported here for brevity. Lengths of the links are instead assumed as exactly known. The selection of the updating parameters should be always done carefully. Indeed, assuming too many parameters for the updating often causes numerical problems, and might lead to local minima in the problem solution. Given the convex formulation here proposed, the latter problem cannot occur.

The modifications has been weighed through the regularization operator $\mathbf{\Omega}$ by reducing the cost of modifying the nodal inertia, which have been set to zero in the nominal model. As for the importance of the different eigenpair specifications, equal weight has been set among the seven vibrational modes in the range of frequency of interest (i.e. $w_i = 1$ for any $i = 1, \ldots, 7$).

#### 4.4.2.2 Experimental results

Evaluation of the results is carried by comparing both the eigenfrequencies and the mode shapes, of both the original nominal model (i.e. the one synthesized through nominal parameters) and the updated one. As usual, in order to obtain a concise and clear evaluation of the results, it is computed the percentage frequency error, $(\omega_i - \overline{\omega}_i)/\omega_i$, and the Modal Assurance Criterion, $\text{MAC} = \left(\boldsymbol{\varphi}^{\mathrm{T}}\overline{\boldsymbol{\varphi}}\right)^2 / \left(\left\|\boldsymbol{\varphi}\right\| \left\|\hat{\boldsymbol{\varphi}}\right\|\right)$, where $\overline{\omega}_i$ and $\overline{\boldsymbol{\varphi}}$ denote, respectively, the eigenfrequency and the eigenvector estimated through the

Table 4.8: Comparison of the experimental and analytical modal properties

| Frequency [Hz] | | | % Frequency Error | | MAC | |
|---|---|---|---|---|---|---|
| Experimental | Nominal model | Updated model | Nominal model | Updated model | Nominal model | Updated model |
| 13.39 | 13.72 | 13.29 | 2.46 | 0.74 | 0.822 | 0.865 |
| 43.57 | 43.88 | 43.30 | 0.71 | 0.62 | 0.976 | 0.989 |
| 64.65 | 66.96 | 64.78 | 3.58 | 0.20 | 0.960 | 0.968 |
| 112.99 | 127.25 | 124.24 | 12.62 | 9.95 | 0.820 | 0.829 |
| 138.15 | 147.23 | 142.54 | 6.57 | 3.17 | 0.830 | 0.830 |
| 154.73 | 171.95 | 159.37 | 11.13 | 3.00 | 0.929 | 0.943 |
| 198.56 | 204.93 | 197.43 | 3.21 | 0.57 | 0.936 | 0.939 |
| 221.37 | 264.20 | 251.32 | 19.35 | 13.53 | 0.926 | 0.930 |

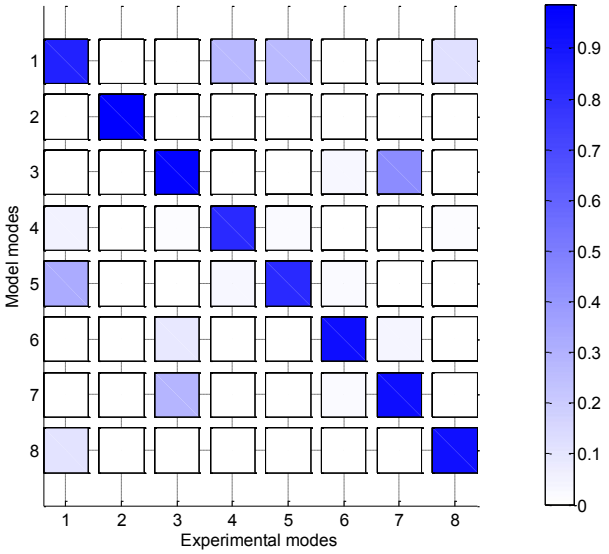


Figure 4.16: MAC matrix between the experimental modes and the updated model modes

models. The results obtained for both the numerical models are listed in Tab. 4.8. They clearly show that model updating has allowed significantly reducing the model discrepancy with the experimental measurements. The major improvement is obtained in term of the eigenfrequencies, whose val-

ues are significantly missed in the nominal model. Indeed, the percentage frequency error for the updated model is smaller than 1% in four modes, by leading to an average value of such an index equal to 3.97% (compared to the 7.46% in the original model). As for the MAC, a smaller improvement has been obtained, since the mode shape specification is accurately meet also by the original model. Nonetheless, the average MAC increases from 0.89 to 0.91 after updating. The result obtained in term of both the frequency and the mode shape is highly satisfactory, given the complexity of the system investigated (whose actual dynamics is nonlinear), the simultaneous presence of more modes to be represented, and the presence of tight constraints bounding the parameter updating.

The analysis of the correlation between the eigenvectors of the updated model and those measured experimentally is also shown in Fig. 4.16 through the MAC matrix. The figure clearly confirms the excellent agreement between the model and the experimental measurements. On the one hand all the experimental modes (in the frequency range of interest) are represented accurately. On the other hand, the off-diagonal terms prove the orthogonality (defined through the canonical scalar product $\mathbf{I}$) between different eigenvectors of the updated model. The results obtained demonstrate the effectiveness of the method.

## 4.5 Chapter summary

In this Chapter an overview on the different MB formulations for MBSs with flexible links has been provided, then the formulation based on the equivalent rigid-link system (ERLS) is described and applied straightforwardly to a rather complex example of flexible-link planar manipulator with hybrid topology.

Successively the manipulator model has been refined by matching experimental and numerical vibration modes through the model updating approach proposed. In particular, the proposed model updating methodology is addressed to tune inertial and elastic parameters of flexible link MB model based on the ERLS. The method takes advantage of the linearization of the nonlinear model to update the mass and stiffness matrices and to the ex-

perimental modal analysis in a stable equilibrium configuration. Once that the experimental eigenvectors are represented in the moving reference frame of the ERLS, through a kinematic transformation and through coordinate expansion, the method is cast as a constrained inverse eigenvalue problem. Constraints on the updating parameters ensure the physical meaningful of the computed values. The use of preconditioners and the regularization also improve the numerical reliability of the convex formulation obtained. The application of the method to the aforementioned manipulator has lead to very satisfactory results.

# Chapter 5

# Model reduction

Regardless of the amount of deformation (small or large), the number of coordinates required to obtain a reasonable mathematical model for flexible-link MBSs can be very large as compared to the number of coordinates used in the analysis of rigid body systems. Such models are often very bulky and require considerable computational efforts, which can prevent their use in simulation [75], and real-time control [76]. Additionally, large dimensional models are often numerically ill conditioned and therefore they cannot be effectively exploited for design optimization (e.g. for the solution of inverse structural modification problems [77, 78]).

Therefore, reduced order models can be very useful in model-based design (see e.g. [79,80]), simulation (see e.g. [76]), control (see e.g. [81,82]) and estimation (see e.g. [83]). Indeed, not only can such models be computationally more reliable and efficient, but their use also simplifies the experimental identification of model parameters by just requiring accurate investigations in a restricted frequency range [84].

Several approaches to model reduction have been presented in literature. Generally speaking either the reduction of different models of different substructures to be coupled (the so called reduction at the component level) or the reduction of the complete model of a complete system (reduction at the system level) have been addressed [85]. The latter is the approach that should be preferred whenever reduced order models are employed for numerical simulations, for the synthesis of model-based controllers or for model-based design and optimization. Indeed, in these fields it is usually de-

sirable getting the best trade-off between accuracy and size, at the cost of an increase in the modeling complexity. Therefore, first of all, an accurate full-order model is often synthesized, and then it is reduced in accordance with the specifications posed by the computation involving the model (i.e. type of model coordinates and frequencies of interest). Indeed, assuming independence between subsystems (i.e. model reduction at component level) often affects negatively the model correctness, by resulting in poor design [86] or controllers with small robustness margins. Therefore, while this assumption makes sense for the purpose of getting faster coupling tests between subsystems, it is reasonable reducing models at the full system level whenever accuracy should be boosted.

The model reduction methods proposed to date can be basically divided into three main categories, according to the state variables employed in the model: non physical, physical and semi physical subspace reduction methods [87]. Clearly, the selection of the most suitable method for performing model reduction depends on several parameters to be evaluated, and is often also a subjective matter since each technique has strengths and weakness.

Non physical reduction methods, such as the Modal Truncation, the Krylov Subspace Method [88] and the Balanced Truncation [89], originate from control theory. These techniques are often unsuitable to model reduction in mechanical systems, since the physical degrees of freedom (dofs) of the full order models are replaced by non physical coordinates and therefore they do not retain their straightforward physical interpretation. Moreover, these techniques may be ill conditioned for large scale models [81].

The availability of physical coordinates in reduced models is of interest, for instance, for coupling a system with other systems (consider not only the CMS [87, 90] but also the coupling with systems designed in other domains, such as the coupling between electro-mechanical systems [79, 91]). Physical coordinates are also of interest when modifications of physical system parameters should be computed through structural modification techniques.

Physical subspace reduction methods are widespread in structural mechanics, since they lead to intuitive model representations in physical coordinates. Among the most relevant, dynamic condensation [92], improved reduction system [93], Guyan condensation [94] are to be mentioned. Gener-

ally speaking, physical reduction methods provide good approximations for static analyses or for dynamic analyses at low frequencies, but may be not accurate when high frequency motion is contemplated [95].

Finally, semi physical methods are often the most suitable to mechanical systems, since the reduced models obtained with these techniques can approximate both the static and the dynamic behavior of mechanical systems accurately and also retain some physical coordinates of interest. In semi physical methods the system behavior is represented through a set of physical coordinates, the so called master dofs, and through a reduced set of non physical coordinates (whose definition depends on the specific boundary conditions set on the physical dofs). On the basis of the boundary conditions set on the master dofs for computing the non physical coordinates, the semi physical techniques are grouped into fixed interface methods [90,96], free interface methods [97–100], hybrid interface methods [98] and loaded interface methods [101].

All the methods mentioned so far, have been developed to reduce linear time-invariant models, but the dynamic equations of the deformable bodies that undergo large rigid body displacements, as flexible links of MBSs, are highly nonlinear.

However, a common way, to reduce the model size of flexible-link MBSs and exploit the well-known reduction techniques developed for linear systems, consists in generating a linear finite element sub-model of each link, reduce it through component mode synthesis, then embed such reduced models in a floating frame [102–106] or in a co-rotational frame [107,108] in order to allow large overall displacements and rotations . Therefore, the model is reduced at the component level. Although such a reduction strategy, widely used for flexible MBSs, is computationally efficient has a drawback, i.e. it does not account for modal characteristic changes due to reference motion.

A model reduction at system level for flexible-link MB models is achieved by means of the adaptive modal integration (AMI) method [109], developed for model obtained through the inertial frame approach [110], or the global modal parameterization (GMP) method [111], developed for model obtained through the floating frame of reference approach [50]. Basically, both methods separate the motion of the mechanism in a nonlinear nominal rigid body

motion and dominant system-level flexible eigenmodes. Then, they compute the matrices of the reduced model in a preprocessing run for a discrete set of configurations along the rigid body trajectory, after which they are interpolated during simulation. The difference between the two methods is in rigid body motion representation, indeed AMI use physical coordinates, while GMP uses the the rigid body system-level eigenmodes.

To the best of author's knowledge no strategy has been developed to perform the reduction at system level of dynamic models obtained through the ERLS. To this end a novel strategy aiming at obtaining reduced dynamic models of flexible-link MBSs has been finalized, in particular it employs the ERLS approach and the fixed interface Craig-Bampton (CB) method [90], suitably modified.

The CB method is a semi physical reduction technique widely used in structural dynamics, and is by far the most popular reduction method in the multibody field, due to a simple and straightforward formulation of the reduction process, combined with good overall performances. Additionally, it is available in most commercial FE codes, which often implement only such a method among those proposed in literature. Generally speaking, the CB method is basically considered a standard framework for model reduction with hybrid coordinates.

The Chapter is set out as follows: in Section 5.1 the CB method is recalled. Section 5.2 tackles an open issue in the application of the CB method, i.e. the selection of the interior modes to be retained in the reduced models, and then it introduces two novel ranking methods for overcoming such an issue. In Section 5.3 the methods described in Section 5.2, which have been initially developed for and applied to linear systems, are adapted and successfully applied to MBS.

## 5.1 Craig Bampton method

In this Section the CB method is briefly recalled; for a more detailed description, the interested reader can refer to the papers cited in the Introduction. Let us consider the FE representation of a $n$-dimensional undamped linear

time-invariant system:

$$\mathbf{M}\ddot{\mathbf{x}}(t) + \mathbf{K}\mathbf{x}(t) = \mathbf{f}(t) \tag{5.1}$$

where vectors $\mathbf{x} \in \mathbb{R}^n$ and $\mathbf{f} \in \mathbb{R}^n$ represent, respectively, the nodal displacements and the nodal forces, $\mathbf{M} \in \mathbb{R}^{n\times n}, \mathbf{K} \in \mathbb{R}^{n\times n}$ are the mass and stiffness matrices and $t$ is the time variable. The practical implementation of the method imposes partitioning the displacement vector $\mathbf{x}$ into two subvectors, $\mathbf{x} = \{\mathbf{x}_1 \quad \mathbf{x}_2\}^{\mathrm{T}}$. Subvector $\mathbf{x}_1 \in \mathbb{R}^m$ comprises the $m$ degrees of freedom (dofs), referred to as the master dofs. Subvector $\mathbf{x}_2 \in \mathbb{R}^s$ comprises the $s$ dofs referred to as the slave or interior dofs ($m + s = n$). The equations of motion Eq.5.1 can be partitioned accordingly:

$$\begin{bmatrix} \mathbf{M}_{11} & \mathbf{M}_{12} \\ \mathbf{M}_{21} & \mathbf{M}_{22} \end{bmatrix} \begin{Bmatrix} \ddot{\mathbf{x}}_1(t) \\ \ddot{\mathbf{x}}_2(t) \end{Bmatrix} + \\ + \begin{bmatrix} \mathbf{K}_{11} & \mathbf{K}_{12} \\ \mathbf{K}_{21} & \mathbf{K}_{22} \end{bmatrix} \begin{Bmatrix} \mathbf{x}_1(t) \\ \mathbf{x}_2(t) \end{Bmatrix} = \begin{Bmatrix} \mathbf{f}_1(t) \\ \mathbf{f}_2(t) \end{Bmatrix} \tag{5.2}$$

The application of the CB technique basically consists of two steps. First of all, an invertible coordinate transformation is applied, which preserves the number of the model dofs; secondly, a model truncation is performed on the transformed model. In particular, in the first step the model representation in Eq. 5.2, with physical coordinates $\mathbf{x} = \{\mathbf{x}_1 \quad \mathbf{x}_2\}^{\mathrm{T}}$, is transformed into an equivalent representation with hybrid coordinates $\mathbf{y}$, by means of the non-singular CB transformation matrix $\mathbf{H}$:

$$\mathbf{x}(t) = \begin{Bmatrix} \mathbf{x}_1(t) \\ \mathbf{x}_2(t) \end{Bmatrix} = \mathbf{H}\mathbf{y}(t) = \mathbf{H} \begin{Bmatrix} \mathbf{x}_1(t) \\ \boldsymbol{\eta}(t) \end{Bmatrix} \tag{5.3}$$

The master dof coordinates $\mathbf{x}_1$ are entirely retained in $\mathbf{y}$ and are typically chosen as those lying at the interface that might be coupled to another system and, often, as those where external loads are applied. Conversely, the slave dof coordinates $\mathbf{x}_2$ are replaced with the so called interior, or fixed interface, modal coordinates $\boldsymbol{\eta} \in \mathbb{R}^s$. $\boldsymbol{\eta}$ is the $s$-dimensional vector of the modal coordinates of the system obtained by constraining the $m$ master dofs. The

CB transformation matrix $\mathbf{H}$ is therefore given by:

$$\mathbf{H} = \begin{bmatrix} \mathbf{I} & \mathbf{0} \\ -\mathbf{K_{22}}^{-1}\mathbf{K_{21}} & \mathbf{\Phi} \end{bmatrix} = \begin{bmatrix} \mathbf{I} & \mathbf{0} \\ \mathbf{B} & \mathbf{\Phi} \end{bmatrix} \tag{5.4}$$

where $\mathbf{I} \in \mathbb{R}^{m \times m}$ is the identity matrix, $\mathbf{0} \in \mathbb{R}^{m \times s}$ is a matrix of zeros, $\mathbf{B} = -\mathbf{K_{22}}^{-1}\mathbf{K_{21}} \in \mathbb{R}^{s \times m}$ is a Guyan's reduction basis and $\mathbf{\Phi} \in \mathbb{R}^{s \times s}$ is the eigenvector matrix of the interior mode shapes and is calculated by solving the eigenvalue problem of the system obtained by constraining the master dofs. The columns of $\mathbf{\Phi}$ ($\boldsymbol{\phi}$) are referred to as the interior, or fixed interface, normal mode shapes, and $\boldsymbol{\eta} \in \mathbb{R}^s$ is therefore the vector of the modal coordinates associated. The columns of matrix $\mathbf{\Psi}_c = [\mathbf{I} \quad \mathbf{K_{22}}^{-1}\mathbf{K_{21}}]^{\mathrm{T}}$ are instead usually referred to as the constraint modes which represent the static deflections due to displacements of the interface. In the second step of the CB technique, the interior modal coordinate vector $\boldsymbol{\eta}$ is truncated to a smaller vector $\widetilde{\boldsymbol{\eta}} \in \mathbb{R}^\tau$ ($\tau \ll s$). $\widetilde{\boldsymbol{\eta}}$ should be chosen so that an adequate approximation of the full system dynamics is provided. The rectangular transformation matrix $\widetilde{\mathbf{H}} \in \mathbb{R}^{n \times (m+\tau)}$ is referred to as a CB reduction basis, and is obtained from Eq. 5.3 by removing the columns of $\mathbf{\Phi}$ associated to the interior modes which are neglected:

$$\mathbf{x}(t) \cong \begin{bmatrix} \mathbf{I} & \mathbf{0} \\ \mathbf{B} & \widetilde{\mathbf{\Phi}} \end{bmatrix} \begin{Bmatrix} \mathbf{x}_1(t) \\ \widetilde{\boldsymbol{\eta}}(t) \end{Bmatrix} = \widetilde{\mathbf{H}}\widetilde{\mathbf{y}}(t) \tag{5.5}$$

The CB system model representation is hence the following:

$$\begin{bmatrix} \overline{\mathbf{M}}_{11} & \overline{\mathbf{M}}_{12} \\ \overline{\mathbf{M}}_{21} & \overline{\mathbf{M}}_{22} \end{bmatrix} \begin{Bmatrix} \ddot{\mathbf{x}}_1(t) \\ \ddot{\widetilde{\boldsymbol{\eta}}}(t) \end{Bmatrix} + \\ + \begin{bmatrix} \overline{\mathbf{K}}_{11} & \mathbf{0} \\ \mathbf{0} & \overline{\mathbf{K}}_{22} \end{bmatrix} \begin{Bmatrix} \mathbf{x}_1(t) \\ \widetilde{\boldsymbol{\eta}}(t) \end{Bmatrix} = \begin{Bmatrix} \overline{\mathbf{f}}_1(t) \\ \overline{\mathbf{f}}_2(t) \end{Bmatrix} \tag{5.6}$$

If, without lack of generality, the modal matrix $\mathbf{\Phi}$ is normalized with respect to the mass matrix $\mathbf{M}_{22}$, the following matrices are obtained:

$$\begin{aligned}
\overline{\mathbf{M}}_{11} &= \mathbf{M}_{11} + \mathbf{B}^{\mathrm{T}}\mathbf{M}_{21} + \mathbf{M}_{12}\mathbf{B} + \mathbf{B}^{\mathrm{T}}\mathbf{M}_{22}\mathbf{B} \\
\overline{\mathbf{M}}_{12} &= \overline{\mathbf{M}}_{21}^{\mathrm{T}} = (\mathbf{M}_{12} + \mathbf{B}^{\mathrm{T}}\mathbf{M}_{22})\widetilde{\mathbf{\Phi}} \\
\overline{\mathbf{M}}_{22} &= \mathbf{I} \\
\overline{\mathbf{K}}_{11} &= \mathbf{K}_{11} + \mathbf{K}_{12}\mathbf{B} \\
\overline{\mathbf{K}}_{22} &= \widetilde{\mathbf{\Omega}} \\
\overline{\mathbf{f}}_1(t) &= \mathbf{f}_1(t) + \mathbf{B}^{\mathrm{T}}\mathbf{f}_2(t) \\
\overline{\mathbf{f}}_2(t) &= \widetilde{\mathbf{\Phi}}^{\mathrm{T}}\mathbf{f}_2(t)
\end{aligned} \tag{5.7}$$

In accordance with the normalization assumed for the eigenvectors, $\widetilde{\mathbf{\Omega}} \in \mathbb{R}^{\tau\times\tau}$ is a diagonal matrix whose entries are the squared angular eigenfrequencies of the constrained system.

## 5.2 Ranking methods

The crux in the practical implementation of the CB method is performing an optimal selection of the interior modes to be retained in reduced models.

Typically, as a widespread rule of thumb, model reduction relies on retaining the interior modes whose eigenfrequencies are not greater than about twice the highest operating frequency [112]. Such a sorting rule based on the eigenfrequencies of the interior modes (henceforth referred to as SBE, for brevity), however, is not based on rigorous principles, as a consequence, it may lead to rough approximations of the full order model by discarding high-frequency interior modes whose participation in the system dynamics is important, or, in contrast, may lead to large dimensional reduced models including low-frequency modes providing negligible contributions.

In order to improve the effectiveness of the reduction, some methods have been proposed in literature to rank and select the interior modes. These techniques can be seen as "auxiliary" methods for CB reduction, since they operate between the two steps of the CB method. This idea is schematically depicted in Fig.5.1.

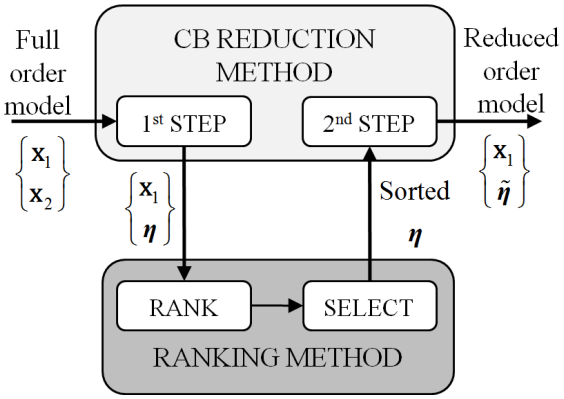


Figure 5.1: Schematic representation of the interaction between a ranking method and the Craig Bampton method

Among the ranking methods proposed in literature one should at least recall the Effective Interface Mass (EIM) method [113,114], the Optimal Modal Reduction (OMR) method [115, 116] and the "Component Mode Synthesis $\chi$" (CMS$\chi$) method [117], which have been proved to be effective techniques that allow reducing model dimensions while preserving accuracy. Their effectiveness is certainly higher than that of the traditional SBE approach.

Basically, all these ranking methods evaluate how the interior normal modes interact with the system interface, on the basis of some coupling terms and are therefore suitable for model reduction at the component level. Additionally, they are general purpose methods that can be applied to several applications, but can lead to approximate and less effective results in some particular cases. Indeed, they cannot handle requirements on the frequencies at which the reduced model should be accurate, or on the external forces in terms of both spatial distribution and frequencies.

However, the reduced model capability to approximate the full system dynamics in a prescribed range of frequencies or the system response at an external force is strongly related to the criterion adopted for ranking and selecting the interior modes to be retained. Hence, effective selection methods are needed to assure accuracy and reduced dimensions concurrently.

In order to address such an issue, this dissertation introduces two ranking methods, the interior mode ranking (IMR) [118] and the energy-based

ranking (EBR) [119–121]. They allow ranking and selecting the interior vibrational modes of the CB method that guarantee obtaining an accurate and minimum-size reduced model.

In particular, the IMR ensures that reduced models accurately describe the dynamics of the system at a specific frequency or in a frequency range of interest.

The EBR method instead ensures that reduced models correctly represent the forced response of a system to periodic inputs (with either single or multi-harmonic components).

Both the methods provide a ranking of the interior vibrational modes on the basis of analytically defined coefficients, describing the relation between each interior mode and either the shape and frequency of the vibration modes of interest, in the case of IMR, or the forced response, in case of EBR.

So the two methods are suitable to two different applications: accurate representation of the system behavior in terms of eigenvectors and eigenvalues in a frequency range (IMR); accurate representation of the system forced response to a periodic excitation force, in terms of spatial distribution and amplitude (EBR).

### 5.2.1 Interior Mode Ranking (IMR) method

The IMR method is aimed at ranking the interior modal coordinates and the related normal modes of the constrained system according to the contribution they provide to the dynamics of one or more selected vibrational modes of the system. As a matter of fact, the correct representation of the dynamics of systems in a frequency range relies on the accurate modeling of just a few vibrational modes of the system. Therefore, the actual state trajectory can be effectively approximated by the combination of these few eigenvectors and their nodal coordinates.

#### 5.2.1.1 IMR for accurate representation of a single mode of a system

In this Section the IMR method will be developed assuming that a single mode is to be represented accurately in the reduced order model. The

straightforward extension to a greater number of modes is instead discussed in Section 5.2.1.2. Let index $i$ refer to a selected vibrational mode of the full order model which has to be represented through the reduced order model. Let $\mathbf{u}_i$ and $\mathrm{q}_i$ be respectively the $i^{\text{th}}$ mode shape and its modal coordinate. In order to evaluate the contribution of each of the $s$ interior modes to the dynamics of the $i^{\text{th}}$ mode of the system, the system is forced to vibrate according to the mode of interest by exciting it through a suitable fictitious force acting on both the master and the slave nodes. The expression of such a fictitious force, whose time history is referred to as $\mathbf{f}(t)$, can be easily found by considering the system response in the frequency domain:

$$\hat{\mathbf{x}}(j\omega) = \sum_{k=1}^{n} \frac{1}{\omega_k^2 - \omega^2} \mathbf{u}_k \mathbf{u}_k^{\mathrm{T}} \hat{\mathbf{f}}(j\omega) \quad k = 1, \cdots, n \tag{5.8}$$

In Eq.5.8 vectors $\mathbf{u}_k \in \mathbb{R}^n$ are the system eigenvectors and $\omega_k^2$ are the eigenvalues, while $\hat{\mathbf{x}}$ and $\hat{\mathbf{f}} \in \mathbb{R}^n$ are respectively the displacement and the fictitious force vector expressed in the frequency domain (henceforth the hat will be employed to represent variables in the frequency domain). Equation 5.8 clearly shows that any force whose spatial shape is orthogonal to all the eigenvectors but one, makes the system vibrate in accordance with the corresponding vibrational mode shape, regardless of the value taken by $(\omega_k^2 - \omega^2)^{-1}$. Since the eigenvectors of an undamped linear system are orthogonal with respect to both the mass matrix $\mathbf{M}$ and the stiffness matrix $\mathbf{K}$, and therefore to any linear combination of such matrices (referred to as $\mathbf{N}$), the fictitious force is defined as a single-harmonic excitation (at angular frequency $\omega_f$), whose amplitude is $\mathbf{N}\mathbf{u}_i$:

$$\mathbf{f}(t) = \mathbf{N}\mathbf{u}_i \cos(\omega_f t) \tag{5.9}$$

In particular, without lack of generality, in this work it is set $\mathbf{N} = \mathbf{M}$. If, as usual, vectors $\mathbf{u}_k \in \mathbb{R}^n$ are normalized with respect to the mass matrix, such a choice allows taking advantage of the $\mathbf{M}$-orthogonality of the eigenvectors:

$$\mathbf{u}_k^{\mathrm{T}} \mathbf{M} \mathbf{u}_i = \begin{cases} 0 & k \neq i \\ 1 & k = i \end{cases} \tag{5.10}$$

The fictitious force can then be expressed in partitioned form and in the frequency domain as follows:

$$\left\{ \begin{array}{c} \hat{\mathbf{f}}_1(j\omega_f) \\ \hat{\mathbf{f}}_2(j\omega_f) \end{array} \right\} = \left\{ \begin{array}{c} \mathbf{M}_{11}\mathbf{u}_{i1} + \mathbf{M}_{12}\mathbf{u}_{i2} \\ \mathbf{M}_{21}\mathbf{u}_{i1} + \mathbf{M}_{22}\mathbf{u}_{i2} \end{array} \right\} \tag{5.11}$$

where $\hat{\mathbf{f}}_1$ and $\hat{\mathbf{f}}_2$ are the force components applied to the master and the slave nodes. As far as the angular frequency of the fictitious force $\omega_f$ is concerned, it is assumed equal to the angular frequency of the mode of interest $\omega_i$ plus a small frequency shift, $\delta\omega$ ($\delta\omega \ll \omega_i$), employed just to prevent numerical singularity and to allow the computation of the receptance matrix for the undamped system.

The analysis of the behavior of the $s$ interior modes of the constrained system in the presence of the fictitious force allows evaluating their contributions to the system dynamics under this particular forcing condition, which in turn allows evaluating the contributions of the interior modes to the representation of the vibrational mode of interest.

Let us focus on the relationship between the modal coordinates ($\mathbf{q}$) and the hybrid coordinates ($\mathbf{y}$) of the $n$-dimensional system. Such a relationship is inferred from Eq. 5.3 and from the definition of the eigenvector matrix of the full system ($\mathbf{U}$), which is assumed to be normalized with respect to $\mathbf{M}$:

$$\begin{aligned} \hat{\mathbf{q}}(j\omega) &= \mathbf{U}^{-1}\mathbf{H}\hat{\mathbf{y}}(j\omega) = \mathbf{U}^{-1}\mathbf{H} \left\{ \begin{array}{c} \hat{\mathbf{x}}_1(j\omega) \\ \hat{\boldsymbol{\eta}}(j\omega) \end{array} \right\} \\ &= \left[ \boldsymbol{\Gamma}_1 \quad \boldsymbol{\Gamma}_2 \right] \left\{ \begin{array}{c} \hat{\mathbf{x}}_1(j\omega) \\ \hat{\boldsymbol{\eta}}(j\omega) \end{array} \right\} \end{aligned} \tag{5.12}$$

The partitioning of the transformation matrix $\mathbf{U}^{-1}\mathbf{H}$ into $\boldsymbol{\Gamma}_1 \in \mathbb{R}^{n\times m}$ and $\boldsymbol{\Gamma}_2 \in \mathbb{R}^{n\times s}$ splits the contribution to $\hat{\mathbf{q}}$ of both $\hat{\mathbf{x}}_1$ and $\hat{\boldsymbol{\eta}}$. The system response to the fictitious force allows evaluating such contributions. In particular, $\hat{\boldsymbol{\eta}}(j\omega_f)$ is obtained by solving the following differential equation arising from Eq. 5.6:

$$\begin{aligned} \ddot{\boldsymbol{\eta}}(t) + \boldsymbol{\Omega}\boldsymbol{\eta}(t) = \boldsymbol{\Phi}^{\mathrm{T}}(\mathbf{M}_{21}\mathbf{u}_{i1} + \mathbf{M}_{22}\mathbf{u}_{i2})\cos(\omega_f t) \\ -\boldsymbol{\Phi}^{\mathrm{T}}\left[\mathbf{M}_{21} + \mathbf{M}_{22}\mathbf{B}\right]\ddot{\mathbf{x}}_1(t) \end{aligned} \tag{5.13}$$

The solution of Eq. 5.13 in the frequency domain is:

$$\hat{\boldsymbol{\eta}}(j\omega_f) = \left[\text{diag}\left(\frac{1}{\frac{\omega_\varsigma^2}{\omega_f^2}-1}\right)\right]\boldsymbol{\Phi}^{\mathrm{T}}\mathbf{m}(j\omega_f) \tag{5.14}$$

where, for compactness of representation, vector $\mathbf{m}(j\omega_f)$ has been defined as follows:

$$\mathbf{m}(j\omega_f) = \left\{\frac{\omega_i^2\mathbf{M}_{21}+\omega_f^2\mathbf{M}_{22}\mathbf{B}}{\omega_f^2(\omega_i^2-\omega_f^2)}\mathbf{u}_{i1} + \frac{\mathbf{M}_{22}}{\omega_f^2}\mathbf{u}_{i2}\right\} \tag{5.15}$$

By just considering the $i^{\text{th}}$ vibrational mode, the $i^{\text{th}}$ row in Eq. 5.12 is developed in the following equation, in order to highlight the contributions of both $\hat{\mathbf{x}}_1$ and $\hat{\boldsymbol{\eta}}$ to the modal coordinate of interest:

$$\hat{\mathrm{q}}_i(j\omega_f) = \sum_{\mu=1}^{m}\Gamma_{1_{i,\mu}}\hat{\mathrm{x}}_{1_\mu}(j\omega_f) + \sum_{\varsigma=1}^{s}\Gamma_{2_{i,\varsigma}}\hat{\eta}_\varsigma(j\omega_f) \tag{5.16}$$

The explicit dependence of $\hat{\mathrm{q}}_i$ on the interior normal modes can be obtained by introducing Eq. 5.14 in Eq. 5.16:

$$\begin{aligned}\hat{\mathrm{q}}_i(j\omega_f) &= \sum_{\mu=1}^{m}\Gamma_{1_{i,\mu}}\hat{\mathrm{x}}_{1_\mu}(j\omega_f) \\ &+ \sum_{\varsigma=1}^{s}\Gamma_{2_{i,\varsigma}}\left(\frac{1}{\frac{\omega_\varsigma^2}{\omega_i^2}-1}\right)\mathbf{m}^{\mathrm{T}}(j\omega_f)\boldsymbol{\phi}_\varsigma\end{aligned} \tag{5.17}$$

In accordance with the CB reduction approach, the first summation in the right-hand side of Eq. 5.17 should be accounted for entirely, being the contributions of the physical master coordinates to the dynamics of the $i^{\text{th}}$ modal coordinate. Conversely, if a reduced order approximation of $\mathrm{q}_i$ is needed, the summation of the contributions of the interior normal modes should be truncated to $\tau \ll s$ elements, by obtaining a reduced order approximation of $\hat{\mathrm{q}}_i$ (referred to as $\widetilde{\hat{\mathrm{q}}}_i$):

$$\begin{aligned}\hat{\mathrm{q}}_i(j\omega_f) &\simeq \widetilde{\hat{\mathrm{q}}}_i(j\omega_f) = \sum_{\mu=1}^{m}\Gamma_{1_{i,\mu}}\hat{\mathrm{x}}_{1_\mu}(j\omega_f) + \\ &+ \sum_{\varsigma=1}^{\tau}\Gamma_{2_{i,\varsigma}}\left(\frac{1}{\frac{\omega_\varsigma^2}{\omega_i^2}-1}\right)\mathbf{m}^{\mathrm{T}}(j\omega_f)\boldsymbol{\phi}_\varsigma\end{aligned} \tag{5.18}$$

Equation Eq. 5.17 clearly shows that the contribution of the $\varsigma^{\text{th}}$ interior normal mode to the dynamics of the full system is weighed through the coefficient $\Upsilon_{i,\varsigma}$:

$$\Upsilon_{i,\varsigma} = \Gamma_{2_{i,\varsigma}} \left( \frac{1}{\frac{\omega_\varsigma^2}{\omega_i^2} - 1} \right) \mathbf{m}^{\mathrm{T}}(j\omega_f)\boldsymbol{\phi}_\varsigma \quad \varsigma = 1, \ldots, s \tag{5.19}$$

Therefore the coefficients $\Upsilon_{i,\varsigma}$ $(\varsigma = 1, \ldots, s)$ can be thought of as participation coefficients of the interior modes in the dynamics of the $i^{\text{th}}$ normal mode of the full order system. It is worth discussing the meaning of the different terms included in $\Upsilon_{i,\varsigma}$, to highlight how the proposed method accounts for several effects that cannot be neglected in the selection. The term $\Gamma_{2_{i,\varsigma}}$ represents the algebraic relation between the $\varsigma^{\text{th}}$ interior modal coordinate and the $i^{\text{th}}$ modal coordinate of the full system. The term $\left(\omega_\varsigma^2/\omega_i^2 - 1\right)$ is a measure of the frequency difference between the $\varsigma^{\text{th}}$ interior mode and the $i^{\text{th}}$ mode of the complete system. This term recalls a common approach adopted in the selection of the modes which is based on selecting the normal modes with the lowest eigenfrequencies (or with the eigenfrequencies which are as close as possible to the range of interest). The third term, $\mathbf{m}^{\mathrm{T}}(j\omega_f)\boldsymbol{\phi}_\varsigma$, can be thought of as a measure of the "orthogonality" between $\mathbf{u}_i$ (which is included in $\mathbf{m}$) and $\boldsymbol{\phi}_\varsigma$. A second interesting interpretation can be given to this last term. By looking at Eq. 5.13 and Eq. 5.15 it is apparent that the term $\mathbf{m}^{\mathrm{T}}(j\omega_f)\boldsymbol{\phi}_\varsigma$ also represents the modal force exciting the $\varsigma^{\text{th}}$ interior mode due to the motion of the master dofs.

The truncation error, introduced by approximating Eq. 5.17 with Eq. 5.18, can be estimated on the basis of the triangle inequality:

$$\begin{aligned} \epsilon_{\mathrm{q}_i} &= \left| \hat{\mathrm{q}}_i(j\omega_f) - \widetilde{\hat{\mathrm{q}}}_i(j\omega_f) \right| = \\ &= \left| \sum_{\varsigma=\tau+1}^{s} \Upsilon_{i,\varsigma} \right| \leq \sum_{\varsigma=\tau+1}^{s} |\Upsilon_{i,\varsigma}| \end{aligned} \tag{5.20}$$

In conclusion, it finds that the larger the absolute value of the coefficient $\Upsilon_{i,\varsigma}$, the more the dynamics of the $\varsigma^{\text{th}}$ interior vibrational mode affects the $i^{\text{th}}$ full system mode $(\mathbf{u}_i)$. Therefore,$|\Upsilon_{i,\varsigma}|$ can be assumed as an effective measure for ranking the interior modes according to their contribution to the full system dynamics.

#### 5.2.1.2 IMR for accurate modal representation in a frequency range

The extension of the approach to the simultaneous representation of more than one vibrational mode of the full system is straightforward. To this end, a weighed participation coefficient, $\Upsilon_{\Lambda,\varsigma}$, is defined for each interior mode. These coefficients synthesize the contributions of each interior mode to the dynamics of the modes of interest. The following equation is adopted:

$$\Upsilon_{\Lambda,\varsigma} = \sum_{i\in\Lambda} \frac{|\Upsilon_{i,\varsigma}|}{||\boldsymbol{\Upsilon}_i||}\alpha_i \qquad \varsigma = 1,\cdots,s \tag{5.21}$$

where $\Lambda$ is the set of the full system vibrational modes to be represented and $\boldsymbol{\Upsilon}_i \in \mathbb{R}^s$ is the vector whose entries are the coefficients $\Upsilon_{i,\varsigma}(\varsigma = 1,\cdots,s)$. $\boldsymbol{\Upsilon}_i$, therefore, collects the participation of all the $s$ interior modes in the dynamics of the $i^{\text{th}}$ vibrational mode of the system. Finally $\alpha_i$ is a normalised weighing factor referring to the $i^{\text{th}}$ mode, employed to define different levels of concern on the representation of each mode in accordance with its importance in the reduced model. Clearly it holds:

$$\sum_{i\in\Lambda} \alpha_i = 1 \tag{5.22}$$

As in the case of one vibrational mode, the larger the value of the coefficient $\Upsilon_{\Lambda,\varsigma}$, the more the dynamics of the $\varsigma^{\text{th}}$ interior mode affects the full system modes in the set $\Lambda$. Therefore the modes retained in the reduced model are those with the largest values of the weighed participation coefficients $\Upsilon_{\Lambda,\varsigma}$ $(\varsigma = 1,\cdots,s)$.

#### 5.2.1.3 Evaluation of the minimum model dimensions

Once the interior modes have been ranked according to the IMR method, it is possible to evaluate a priori the minimum number of the interior modes needed. To this end, the relative truncation error, $\varepsilon_{\mathrm{q}_\Lambda}$, is introduced:

$$\begin{aligned} \varepsilon_{\mathrm{q}_\Lambda} &= \left| \sum_{i\in\Lambda} \frac{\hat{\mathrm{q}}_i(j\omega_{f_i}) - \widetilde{\hat{\mathrm{q}}}_i(j\omega_{f_i})}{\hat{\mathrm{q}}_i(j\omega_{f_i})}\alpha_i \right| \\ &\leq \sum_{i\in\Lambda} \sum_{\varsigma=\tau+1}^{s} \frac{|\Upsilon_{i,\varsigma}|}{\left|\frac{1}{\omega_i^2-\omega_{f_i}^2}\right|}\alpha_i \end{aligned} \tag{5.23}$$

This parameter provides an evaluation of the accuracy of the reduced model obtained by retaining the first $\tau$ interior modes. Clearly, the closer $\varepsilon_{q\Lambda}$ to zero, the more the reduced model represents correctly the dynamics of interest. The modes to be retained are therefore those ensuring that $\varepsilon_{q\Lambda}$ is below a prescribed threshold.

### 5.2.2 IMR method application and assessment

In this Section the IMR method is applied to a resonant system and its effectiveness is tested in the representation of either one or two modes of the full order system. The results obtained are also compared with those provided by other methods available in literature (see Section 5.2).

#### 5.2.2.1 Criteria for result evaluation

Two parameters are adopted to evaluate the accuracy of the reduced model in matching the mode frequency and shape of the full order model. Such parameters give an effective and concise measure of the correctness of the approximation provided. The first parameter is the relative (percentage) error on the natural frequency:

$$e_f = \frac{|f_i - f_*|}{f_i} \cdot 100 \tag{5.24}$$

where $f_i$ and $f_*$ are the frequencies of the mode of interest respectively in the full and in the reduced order model.

The second parameter is the normalized cross orthogonality (NCO) [122]:

$$\mathrm{NCO} = \frac{\left(\mathbf{u}_i^{\mathrm{T}}\mathbf{M}\mathbf{u}_*\right)^2}{\left(\mathbf{u}_i^{\mathrm{T}}\mathbf{M}\mathbf{u}_i\right)\left(\mathbf{u}_*^{\mathrm{T}}\mathbf{M}\mathbf{u}_*\right)} \tag{5.25}$$

where $\mathbf{u}_i \in \mathbb{R}^n$ is the eigenvector of interest represented through the full order model (i.e. the "actual" mode shape), while $\mathbf{u}_* = \widetilde{\mathbf{H}}\overline{\mathbf{u}}$ is its approximation provided by the reduced order model. The $n$-dimensional vector $\mathbf{u}_* \in \mathbb{R}^n$ is spanned by the columns of the CB reduction basis (the transformation matrix) with the entries of $\overline{\mathbf{u}}$ as the scalar coefficients of the linear combination. In practice, the reduced order eigenvector, $\overline{\mathbf{u}} \in \mathbb{R}^{m+\tau}$, is transformed into a $n$-dimensional vector through the reduced order CB transformation

matrix $\widetilde{\mathbf{H}}$. Generally speaking the NCO is the squared cosine between two $n$-dimensional and arbitrarily scaled vectors computed by using $\mathbf{M}$ as the scalar product. Thus it provides a measure of the $\mathbf{M}$-orthogonality of the vectors and ranges from 0 to 1. Clearly, the higher the NCO, the more the vectors are $\mathbf{M}$-parallel and therefore the more they represent the same mode shape.

#### 5.2.2.2 Test case: bar horn

The system chosen for validation is the ultrasonic bar horn with a single central slot and straight profile, discussed in [123]. This device is an ultrasonic resonator, or sonotrode, recalling the ones typically employed in plastics welding. Such sonotrodes are usually excited by piezoelectric transducers. Transducers are driven at a frequency which should match, or be as close as possible to, the eigenfrequency of sonotrode first longitudinal mode. As for the shape of the oscillation, the horns are designed to have uniform displacements along the output face (i.e. the one in contact with the plastic film) to ensure uniform welding. The studied bar horn is assumed to be made of Aluminium alloy Al7075 (mass density $\rho = 2.81\text{g/cm}^3$, Young's modulus $\text{E} = 71.7$ GPa, Poisson's ratio $\nu = 0.33$, yield stress $\sigma_y = 450$ MPa).

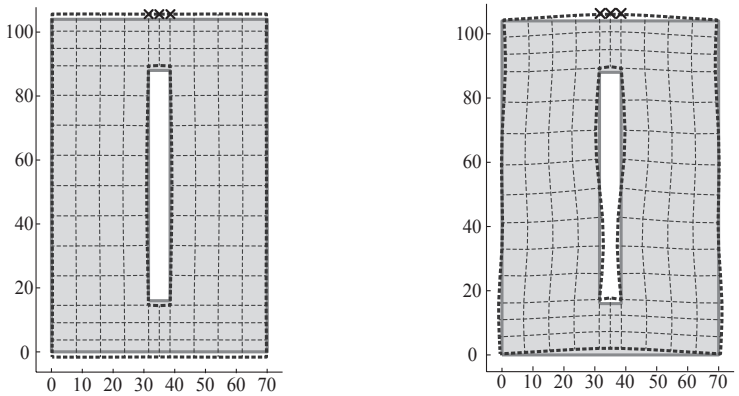


(a) (b)

Figure 5.2: Selected modal shapes of the ultrasonic horn: (a) first mode (b) second mode.

The dimensions (length, width and thickness) of the bar horn are respectively $104 \times 70 \times 30$ mm, while the dimensions of the slot are respectively $72 \times 7 \times 30$ mm. The full order FE model of the horn (in free-free boundary conditions) has been developed adopting non uniform mesh with plane elements (four nodes per element and two dofs per node). The model dofs are 316. The computed frequency of the first longitudinal mode (the $8^{\text{th}}$ mode in an ascending frequency sorting of the modes), is 24.878 kHz. The FE mesh adopted is fine enough to approximate the actual value of this frequency, measured experimentally in [123], with a 0.7 % error. As for the master nodes (represented through the crosses in the Figure 5.2(a) and 5.2(b)), they have been chosen as those on the boundary surface coupling the horn with a booster, which is in turn excited by an actuator in a typical ultrasonic welding stack. Such a choice leads to 6 master dofs and 310 slave dofs.

It is worth observing that this device represents a particularly significant test case to evaluate the correctness and the applicability of the IMR method. Indeed, if the first longitudinal mode shape lacks adequate uniformity in the output surface, optimization through inverse structural modification techniques should be performed. Model reduction is thus an essential step to improve the numerical conditioning of the mathematical problem to be solved [77].

The goal of the reduced model of an ultrasonic horn is primarily to ensure an accurate representation of the aforementioned first longitudinal mode (the $8^{\text{th}}$ mode, in the full order model). The deformed shape of the $8^{\text{th}}$ mode is schematically depicted in Fig. 5.2(a) in dashed black lines. In the same figure, the deformed shape is compared with the undeformed bar horn, depicted in gray continuous line.

Additionally,it is assumed that the $14^{\text{th}}$ mode is to be represented correctly too. Thus, the set of the modes to be represented is $\Lambda = \{8, 14\}$. The $14^{\text{th}}$ vibrational mode is schematically depicted in Fig. 5.2(b) in dashed black lines, from which it is evident that the corresponding deformation occurs prevalently in the longitudinal direction. The eigenfrequency of the $14^{\text{th}}$ mode is 48.543 kHz, which is almost twice the eigenfrequency of the first longitudinal mode (24.878 kHz). Thus, the $14^{\text{th}}$ mode can be basically considered the second longitudinal mode. Both the modes have been equally

Table 5.1: Relative truncation error for reduced models of ascending dimensions

| $N_{red}$ [−] | $\varepsilon_{q\Lambda}$ [%] |
|---|---|
| 7 | 70.8666 |
| 8 | 47.9001 |
| 9 | 35.4221 |
| 10 | 25.5901 |
| 11 | 17.0620 |
| 12 | 8.5531 |
| 13 | 3.3567 |
| 14 | 1.5902 |
| 15 | 0.7700 |

Table 5.2: Reduced models of ascending dimensions

| | | | | $8^{th}$ mode | | $14^{th}$ mode | |
|---|---|---|---|---|---|---|---|
| $N_{red}$ | $\lvert\Upsilon_{\Lambda,\varsigma}\rvert$ | $N_\varsigma$ | $\varepsilon_{q\Lambda}$ | $e_f$ | NCO | $e_f$ | NCO |
| [−] | [−] | [−] | [%] | [%] | [−] | [%] | [−] |
| 15 | 6.40E-02 | 12 | 0.77 | 0.09 | 0.9994 | 0.79 | 0.9779 |
| 16 | 3.05E-02 | 22 | 0.58 | 0.05 | 0.9997 | 0.43 | 0.9921 |
| 17 | 7.08E-03 | 34 | 0.41 | 0.04 | 0.9997 | 0.30 | 0.9943 |
| 18 | 6.02E-03 | 26 | 0.26 | 0.03 | 0.9998 | 0.21 | 0.9961 |
| 19 | 5.82E-03 | 19 | 0.20 | 0.02 | 0.9998 | 0.15 | 0.9982 |
| 20 | 2.21E-03 | 29 | 0.16 | 0.02 | 0.9998 | 0.11 | 0.9987 |

weighted in Eq. 5.23, i.e. $\alpha_8 = \alpha_{14} = 0.5$.

In order to estimate the minimum dimensions of the reduced model, first of all the relative truncation error $\varepsilon_{q\Lambda}$ is evaluated. By setting a 1% threshold for $\varepsilon_{q\Lambda}$, at least 9 interior modes are needed, and hence the minimum model dimensions are 15, as it is shown in Tab. 5.1. The overall dimensions of the model $N_{red}$ the row refers to are stated in the first column. Clearly, model dimensions cannot be smaller than 7, due to master dofs.

A thorougher analysis is proposed in Tab. 5.2, which provides further details on the accuracy of the models obtained by including additional interior modes ranked through $\Upsilon_{\Lambda,\varsigma}$. Each row of the table describes the characteristics of a single reduced model obtained by retaining the 6 master dofs plus both the interior mode in the third column of the row and the ones in the rows above. Following a widespread approach the mode numbers $N_\varsigma$ are defined by sorting the modes with ascending frequency. The modes are progressively added, each time selecting the mode with the highest participation coefficient $|\Upsilon_{\Lambda,\varsigma}|$, shown in the second column. It is worth stressing that the most relevant modes are not the lowest frequency ones. Tables 5.1 and 5.2 show that the analysis of the relative truncation error $\varepsilon_{q\Lambda}$ provides an effective and

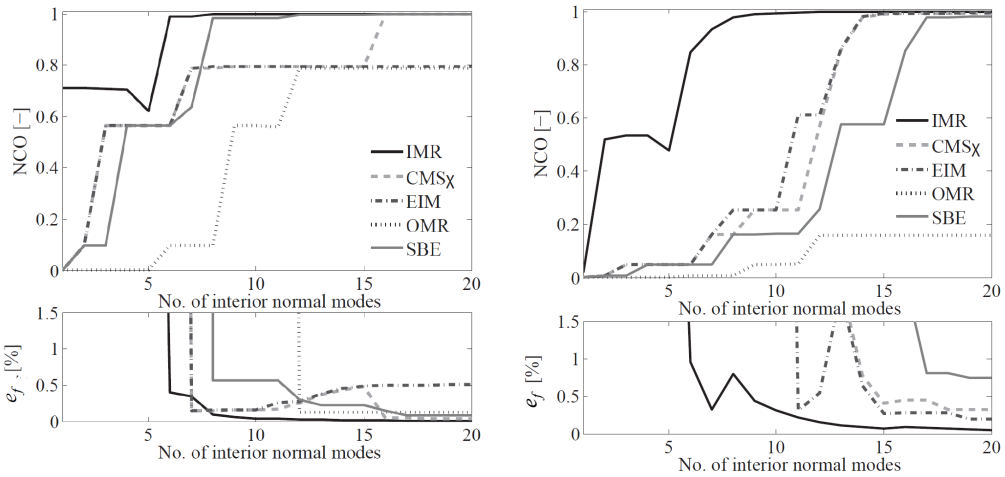


(a) (b)

Figure 5.3: NCO (top) and $e_f$ (bottom) for the $8^{\text{th}}$ mode (a) and the $14^{\text{th}}$ mode (b) vs number of interior modes selected.

straightforward measure of the model error. Indeed, when $\varepsilon_{q_\Lambda}$ falls below an 1% threshold, a very accurate approximation is obtained (see $e_f$ and NCO in columns from 5 to 8 in Tab. 5.2 ). Therefore, such a parameter is an effective aid in the identification of the minimum number of interior modes to be included in the reduced model. Based on the value of $\varepsilon_{q_\Lambda}$, it comes out that at least 9 interior modes are needed, to approximate accurately the $8^{\text{th}}$ and $14^{\text{th}}$ modes of the 316-dimensional model. In order to further highlight the effectiveness of the proposed model and its capability to ensure minimum model dimensions, a comparison is proposed with other ranking methods [112–117], as well as to the common selection approach based on ascending values of the eigenfrequency (SBE). The results are plotted in Fig. 5.3. In particular, Fig. 5.3(a) displays the NCO (top) and $e_f$ (bottom) for the $8^{\text{th}}$ mode, while Fig. 5.3(b) displays the same parameters for the $14^{\text{th}}$ mode. Although most of these methods provide effective model reduction, the results summarized in Fig. 5.3 clearly highlight that the proposed IMR (black lines) outperforms the other techniques by selecting the minimum number of interior modes.

### 5.2.3 Energy-Based Ranking (EBR) method

The goal of the EBR is finding an optimal sequence according to which the interior modes should be progressively included to achieve a desired accuracy of the forced response of the reduced-order model at the frequencies of interest, while keeping model dimensions to a minimum. The underlying idea is that the most important interior modes are those providing the largest energy contributions to the system forced response.

#### 5.2.3.1 System energy in physical coordinates

Let us consider a $n$-dimensional linear time-invariant and undamped vibrating system, represented through its stiffness and mass matrices $\mathbf{K}, \mathbf{M} \in \mathbb{R}^{nxn}$ and the physical coordinate vector $\boldsymbol{x}$ . The total system mechanical energy is given by the sum of the elastic and kinetic energy contributions:

$$\mathrm{E}(t) = \frac{1}{2}\boldsymbol{x}^{\mathrm{T}}(t)\mathbf{K}\boldsymbol{x} + \frac{1}{2}\dot{\boldsymbol{x}}^{\mathrm{T}}(t)\mathbf{M}\dot{\boldsymbol{x}} \tag{5.26}$$

The system is supposed to be excited on the master dofs by a set of periodic external nodal forces $\boldsymbol{f} \in \mathbb{R}^n$, which are represented as the sum of a finite numbers $n_f$ of harmonic components $\boldsymbol{f}_k$:

$$\boldsymbol{f}(t) = \begin{Bmatrix} \boldsymbol{f}_{master}(t) \\ \mathbf{0} \end{Bmatrix} = \sum_{k=0}^{n_f} \boldsymbol{f}_k(t) = \sum_{k=0}^{n_f} \begin{Bmatrix} \mathrm{f}_{1,k}\cos(\omega_k t + \alpha_{1,k}) \\ \vdots \\ \mathrm{f}_{m,k}\cos(\omega_k t + \alpha_{m,k}) \\ 0_{m+1,k} \\ \vdots \\ 0_{n,k} \end{Bmatrix} \tag{5.27}$$

In Eq. 5.27 $\boldsymbol{f}_k$ is the $k^{th}$ harmonic component of the periodic force, and $\mathrm{f}_{i,k}, \omega_k, \alpha_{i,k}$ are, respectively, the amplitude, the angular frequency and the relative phase of the $k^{th}$ harmonic component exciting the $i^{th}$ dof. By applying the superposition principle, the system steady-state response to such a force is represented as the sum of the responses $\boldsymbol{x}_k$ $(k = 1, \ldots, n_f)$ to each

single-harmonic component $\boldsymbol{f}_k$:

$$\boldsymbol{x}(t) = \sum_{k=0}^{n_f} \boldsymbol{x}_k(t) = \sum_{k=0}^{n_f} \begin{Bmatrix} \mathrm{x}_{1,k}\cos(\omega_k t + \beta 1, k) \\ \vdots \\ \mathrm{x}_{n,k}\cos(\omega_k t + \beta_{n,k}) \end{Bmatrix} \tag{5.28}$$

where $\mathrm{x}_{i,k}, \beta i, k$ are, respectively, the amplitude and the relative phase of the response of the $i^{th}$ dof to the $k^{th}$ harmonic component. On the basis of Eq. 5.28, the system total energy defined in Eq. 5.26 can be rewritten highlighting the contributions at each frequency:

$$\begin{aligned} \mathrm{E}(t) &= \frac{1}{2}\sum_{k=1}^{n_f}\left(\boldsymbol{x}_k^{\mathrm{T}}(t)\mathbf{K}\boldsymbol{x}_k + \frac{1}{2}\dot{\boldsymbol{x}}_k^{\mathrm{T}}(t)\mathbf{M}\dot{\boldsymbol{x}}_k\right) + \\ &\quad \sum_{k=1}^{n_f}\sum_{j=k+1}^{n_f}\left(\boldsymbol{x}_k^{\mathrm{T}}(t)\mathbf{K}\boldsymbol{x}_j + \frac{1}{2}\dot{\boldsymbol{x}}_k^{\mathrm{T}}(t)\mathbf{M}\dot{\boldsymbol{x}}_j\right) \end{aligned} \tag{5.29}$$

The mean value of the time varying energy in a period of excitation $\tau$ is therefore:

$$\begin{aligned} \overline{\mathrm{E}} &= \frac{1}{\tau}\int_0^{\tau} \mathrm{E}(t)dt \\ &= \frac{1}{2}\sum_{k=1}^{n_f}\left(\sum_{i=1}^{n}\left(\frac{\mathbf{K}_{ii} + \omega_k^2\mathbf{M}_{ii}}{2}\mathrm{x}_{i,k}^2 + \right.\right. \\ &\quad \left.\left.\sum_{j=i+1}^{n}\left(\mathbf{K}_{ij} + \omega_k^2\mathbf{M}_{ij}\right)\mathrm{x}_{i,k}\mathrm{x}_{j,k}\cos(\beta_{i,k} - \beta_{j,k})\right)\right) \end{aligned} \tag{5.30}$$

In the development of the ranking method, the mean energy $\overline{\mathrm{E}}$ will be accounted for, since it is a time-independent scalar value providing a meaningful and concise measure of the elastic and kinetic energy stored in the system in a period. Equation 5.30 can be rewritten in the following more compact form:

$$\overline{\mathrm{E}} = \frac{1}{2}\sum_{k=1}^{n_f}\left(\mathbf{x}_k^{\mathrm{T}}\mathbf{D}_{s\beta_k}\frac{\mathbf{K} + \omega_k^2\mathbf{M}}{2}\mathbf{D}_{s\beta_k}\mathbf{x}_k + \mathbf{x}_k^{\mathrm{T}}\mathbf{D}_{c\beta_k}\frac{\mathbf{K} + \omega_k^2\mathbf{M}}{2}\mathbf{D}_{c\beta_k}\mathbf{x}_k\right) \tag{5.31}$$

where $\mathbf{x}_k$ is the amplitude vector of the response to the $k^{th}$ harmonic component. The notation $\mathbf{D}_{s\beta_k}$ and $\mathbf{D}_{c\beta_k}$ denotes diagonal matrices having, respectively, the sine and cosine of $\beta_{i,k}$ $(i = 1, \ldots, n)$ on the main diagonal.

#### 5.2.3.2 Energy contributions of the interior modes

In order to evaluate the contribution of each interior mode to the system energy, and in particular to its mean value $\overline{\mathrm{E}}$, the set of physical coordinates in Eq. 5.31 is transformed in the CB basis through Eq. 5.3:

$$\overline{\mathrm{E}} = \frac{1}{2}\sum_{k=1}^{n_f}\left(\mathbf{y}_k^{\mathrm{T}}\mathbf{D}_{s_k}\mathbf{H}^{\mathrm{T}}\frac{\mathbf{K}+\omega_k^2\mathbf{M}}{2}\mathbf{H}\mathbf{D}_{s_k}\mathbf{y}_k + \mathbf{y}_k^{\mathrm{T}}\mathbf{D}_{c_k}\mathbf{H}^{\mathrm{T}}\frac{\mathbf{K}+\omega_k^2\mathbf{M}}{2}\mathbf{H}\mathbf{D}_{c_k}\mathbf{y}_k\right) \tag{5.32}$$

where $\mathbf{y}_k = \left\{\mathbf{x}_{1_k} \quad \boldsymbol{\eta}_k\right\}^{\mathrm{T}}$ is the vector of the amplitude of the response to the $k^{th}$ harmonic component (in hybrid coordinates), $\mathbf{D}_{s_k}$ and $\mathbf{D}_{c_k}$ are diagonal matrices defined as follows:

$$\mathbf{D}_{s_k} = \begin{bmatrix}\mathbf{D}_{s\beta_{1,k}} & \mathbf{0}\\ \mathbf{0} & \mathbf{D}_{s\gamma_k}\end{bmatrix} \qquad \mathbf{D}_{c_k} = \begin{bmatrix}\mathbf{D}_{c\beta_{1,k}} & \mathbf{0}\\ \mathbf{0} & \mathbf{D}_{c\gamma_k}\end{bmatrix}$$

where

$$\begin{aligned}\mathbf{D}_{s\beta_{1,k}} &= \mathrm{diag}\left(\sin(\beta_{i,k})\right) & \mathbf{D}_{s\gamma_k} &= \mathrm{diag}\left(\sin(\gamma_{j,k})\right)\\ \mathbf{D}_{c\beta_{1,k}} &= \mathrm{diag}\left(\cos(\beta_{i,k})\right) & \mathbf{D}_{c\gamma_k} &= \mathrm{diag}\left(\cos(\gamma_{j,k})\right)\\ i &= 1,\ldots,m & j &= 1,\ldots,s\end{aligned} \tag{5.33}$$

(the notation $\mathrm{diag}(\mathbf{v})$ represents a square diagonal matrix with the elements of an arbitrary vector $\mathbf{v}$ on the main diagonal). The terms in Eq. 5.33 represent the relative phase of the response of the interior modal coordinate to the $j^{th}$ harmonic component. Equation 5.32 also introduces matrices $\mathbf{H}^{\mathrm{T}}\mathbf{K}\mathbf{H} := \overline{\mathbf{K}}$ and $\mathbf{H}^{\mathrm{T}}\mathbf{M}\mathbf{H} := \overline{\mathbf{M}}$, which are the stiffness and the mass matrices in the CB basis, previously defined in Eqs. 5.6 and 5.7. Such matrices will be hereafter referred to through the following compact notation, with the obvious meaning of the symbols (see Eq. 5.7):

$$\overline{\mathbf{K}} = \begin{bmatrix}\overline{\mathbf{K}}_{11} & \mathbf{0}\\ \mathbf{0} & \boldsymbol{\Omega}\end{bmatrix} \qquad \overline{\mathbf{M}} = \begin{bmatrix}\overline{\mathbf{M}}_{11} & \overline{\overline{\mathbf{M}}}_{12}\boldsymbol{\Phi}\\ \boldsymbol{\Phi}^{\mathrm{T}}\overline{\overline{\mathbf{M}}}_{21} & \mathbf{I}\end{bmatrix} \tag{5.34}$$

By making explicit the entries of $\mathbf{y}_k$, $\mathbf{D}_{sk}$ and $\mathbf{D}_{ck}$ in Eq. 5.32, and by employing the notation introduced in Eq. 5.34, the contributions to the mean energy provided by the master dofs and by the interior modal coordinates

can be splitted as follows:

$$\begin{aligned}\overline{\mathrm{E}} \;=\; \sum_{k=1}^{n_f} \Bigg( & \mathbf{x}_{1_k}^{\mathrm{T}} \frac{\mathbf{D}_{s\beta_{1,k}} \left[\overline{\mathbf{K}}_{11} + \omega_k^2 \overline{\mathbf{M}}_{11}\right] \mathbf{D}_{s\beta_{1,k}} + \mathbf{D}_{c\beta_{1,k}} \left[\overline{\mathbf{K}}_{11} + \omega_k^2 \overline{\mathbf{M}}_{11}\right] \mathbf{D}_{c\beta_{1,k}}}{2} \mathbf{x}_{1_k} \\ & + \omega_k^2 \mathbf{x}_{1_k}^{\mathrm{T}} \left[\mathbf{D}_{s\beta_{1,k}} \overline{\overline{\mathbf{M}}}_{12} \boldsymbol{\Phi} \mathbf{D}_{s\gamma_k} + \mathbf{D}_{c\beta_{1,k}} \overline{\overline{\mathbf{M}}}_{12} \boldsymbol{\Phi} \mathbf{D}_{c\gamma_k}\right] \boldsymbol{\eta}_k \\ & + \boldsymbol{\eta}_k^{\mathrm{T}} \frac{\mathbf{D}_{s\gamma_k} \left[\boldsymbol{\Omega} + \omega_k^2 \mathbf{I}\right] \mathbf{D}_{s\gamma_k} + \mathbf{D}_{c\gamma_k} \left[\boldsymbol{\Omega} + \omega_k^2 \mathbf{I}\right] \mathbf{D}_{c\gamma_k}}{2} \boldsymbol{\eta} \Bigg) \frac{1}{2} \end{aligned} \tag{5.35}$$

In equation 5.35 three distinct terms can be recognized within brackets. The first term (first line) represents the contribution of the $m$-dimensional external dof subsystem (represented through $\overline{\mathbf{K}}_{11}$ and $\overline{\mathbf{M}}_{11}$) regardless of the motion of the interior modes. Therefore, it can be discarded in the evaluation of the contribution of each interior mode to $\overline{\mathrm{E}}$. Conversely, all the other terms within brackets explicitly depend on the interior modes and therefore must be accounted for. In particular, the second term (second line) represents the inertial coupling between the master dofs and the interior modal coordinates, while the third term (third line) only depends on the interior modes. The second and third terms within brackets of all the $k^{th}$ harmonic components will be henceforth collected in the scalar variable named $\overline{\mathrm{E}}_s$, which can be also expressed as the summation of the contributions of each interior mode (indexed through $\varsigma = 1, \ldots, n_f$), over the $n_f$ harmonic components of the force (indexed through $k = 1, \ldots, n_f$):

$$\overline{\mathrm{E}}_s = \frac{1}{2} \sum_{\varsigma=1}^{s} \sum_{k=1}^{n_f} \left( \frac{1}{2} \left(\omega_\varsigma^2 + \omega_k^2\right) \eta_{\varsigma,k}^2 + \omega_k^2 \mathbf{x}_{1_k}^{\mathrm{T}} \mathbf{D}_{\beta_{1,k}\gamma_{\varsigma,k}} \overline{\overline{\mathbf{M}}}_{12} \boldsymbol{\phi}_\varsigma \eta_{\varsigma,k} \right)$$

$$\text{with} \qquad \mathbf{D}_{\beta_{1,k}\gamma_{\varsigma,k}} = \mathrm{diag}\left(\cos(\beta_{i,k} - \gamma_{\varsigma,k})\right), \quad i = 1, \ldots, m \tag{5.36}$$

The amplitudes $\mathbf{x}_{1,k}$ and $\eta_{\varsigma,k}$ ($\varsigma = 1, \ldots, s$) in hybrid coordinates of the forced responses to each harmonic component in Eq. 5.36 can be rewritten as a function of the external force, by means of receptance matrices:

$$\begin{Bmatrix} \mathbf{x}_{1,k} \\ \boldsymbol{\eta}_k \end{Bmatrix} = \left| \left[\overline{\mathbf{K}} - \omega_k^2 \overline{\mathbf{M}}\right]^{-1} \mathbf{f}_k \right| := \left| \begin{bmatrix} \mathbf{G}_{1_k} \\ \mathbf{G}_{\boldsymbol{\eta}_k} \end{bmatrix} \mathbf{f}_k \right| \tag{5.37}$$

where $\mathbf{f}_k = \left\{ \mathrm{f}_{1,k} \quad \dots \quad \mathrm{f}_{m,k} \quad 0_{m+1,k} \quad \dots \quad 0_{n,k} \right\}^{\mathrm{T}}$ is the amplitude vector of the $k^{th}$ harmonic component of the force vector $\boldsymbol{f}$ (see Eq. 5.27), and $\mathbf{G}_{1_k}$ and $\mathbf{G}_{\boldsymbol{\eta}_k}$ are receptance matrices. By substituting Eq.5.37 in Eq.5.36, $\overline{\mathrm{E}}_s$ can be explicitly written as a function of the external force:

$$\overline{\mathrm{E}}_s = \frac{1}{2} \sum_{\varsigma=1}^{s} \sum_{k=1}^{n_f} \left( \frac{1}{2} \left( \omega_\varsigma^2 + \omega_k^2 \right) \left( \mathbf{G}_{\eta_{\varsigma,k}} \mathbf{f}_k \right)^2 + \omega_k^2 \left| \mathbf{f}_k^{\mathrm{T}} \mathbf{G}_{1_k}^{\mathrm{T}} \right| \mathbf{D}_{\beta_{1,k}\gamma_{\varsigma,k}} \overline{\overline{\mathbf{M}}}_{12} \boldsymbol{\phi}_\varsigma \left| \mathbf{G}_{\eta_{\varsigma,k}} \mathbf{f}_k \right| \right) \tag{5.38}$$

Such an expression clearly shows that the contribution of the $\varsigma^{th}$ interior mode to the system mean energy can be evaluated through the scalar coefficients $\Gamma_\varsigma$:

$$\Gamma_\varsigma = \sum_{k=1}^{n_f} \left| \tfrac{1}{2} \left( \omega_\varsigma^2 + \omega_k^2 \right) \left( \mathbf{G}_{\eta_{\varsigma,k}} \mathbf{f}_k \right)^2 + \omega_k^2 \left| \mathbf{f}_k^{\mathrm{T}} \mathbf{G}_{1_k}^{\mathrm{T}} \right| \mathbf{D}_{\beta_{1,k}\gamma_{\varsigma,k}} \overline{\overline{\mathbf{M}}}_{12} \boldsymbol{\phi}_\varsigma \left| \mathbf{G}_{\eta_{\varsigma,k}} \mathbf{f}_k \right| \right|$$

$$\varsigma = 1, \dots, s \tag{5.39}$$

In the equation above, $\mathbf{G}_{\eta_{\varsigma,k}}$ is the $\varsigma^{th}$ row of the receptance matrix $\mathbf{G}_{\boldsymbol{\eta}_k}$, relating the response of the $\varsigma^{th}$ interior mode to the $k^{th}$ harmonic component of the force, $\eta_{\varsigma,k} = \left| \mathbf{G}_{\eta_{\varsigma,k}} \mathbf{f}_k \right|$. Clearly, the larger the value of $\Gamma_\varsigma$, the more the $\varsigma^{th}$ interior mode contributes to the system response in the presence of the periodic force $\boldsymbol{f}(t)$ defined through Eq. 5.27. It is here therefore proposed to rank the interior modes in descending order based on the values of $\Gamma_\varsigma$. Then, they can be progressively included in the reduced model until a desired model accuracy is achieved.

### 5.2.4 EBR method application and assessment

This Section proposes two different test cases for demonstrating the EBR method effectiveness: an ultrasonic sonotrode (Section 5.2.4.2) and a vibratory feeder (Section 5.2.4.3). Both the systems are often employed in industry or research laboratories, and are designed to generate suitable vibrations excited by periodic forces. Such forces usually have a few harmonic components and their spatial distribution is known. They are, therefore, well suited for the application of the proposed method. On the other hand, the availability of reduced order models is essential for model-based design or

optimization of these devices, both whenever direct approaches are adopted (i.e. through extensive multiphisics simulations), and when inverse dynamic structural modification techniques are employed [77].

#### 5.2.4.1 Criteria for result evaluation

A reduced order model should provide an accurate description of the system forced response to the periodic force, both in terms of spatial distribution and amplitude. Two parameters are adopted to evaluate the correctness of the approximation provided by the reduced models and hence the method capability to select the most important modes to be retained. The first one is the modal assurance criterion (MAC) between the vectors of the forced responses in all the FE model nodes (at an arbitrary time $\bar{t}$) computed through the full-order model ($\boldsymbol{x}$) and through the reduced-order ones ($\widetilde{\boldsymbol{x}}$):

$$\mathrm{MAC} = \frac{\left(\boldsymbol{x}^{\mathrm{t}}(\bar{t})\widetilde{\boldsymbol{x}}(\bar{t})\right)^2}{\left(\boldsymbol{x}^{\mathrm{T}}(\bar{t})\boldsymbol{x}(\bar{t})\right)\left(\widetilde{\boldsymbol{x}}^{\mathrm{T}}(\bar{t})\widetilde{\boldsymbol{x}}(\bar{t})\right)} \tag{5.40}$$

In practice, the MAC is the squared cosine between the two mentioned vectors and should hence approach 1 to ensure identical spatial distributions of the forced response (i.e. parallel vectors). In the case of the reduced models, whose dimension $m + r$ is smaller than $n$, the $n$-dimensional vector $\widetilde{\boldsymbol{x}}$ is computed by mapping the reduced set of hybrid coordinates into an approximated set of physical coordinates by means of Eq. 5.5, where vector $\widetilde{\boldsymbol{\eta}}$ includes the interior modal coordinates retained in each reduced model evaluated.

Since the MAC does not provide any information on the amplitude of the system response, and therefore of the receptances, the relative gain error is introduced and defined as follows:

$$\varepsilon_g = \frac{x_i(\bar{t}) - \widetilde{x}_i(\bar{t})}{x_i(\bar{t})} \cdot 100 \tag{5.41}$$

Such a parameter is the relative percentage error between the forced response computed through the full-order model $x_i$ and through the reduced-order ones $\widetilde{x}_i$, evaluated at an arbitrary time $\bar{t}$ for one representative, or sample, master dof (denoted through index $i$). Clearly, since the same force is considered for

both the models, $\varepsilon_g$ can be also seen as the relative percentage error of the receptances.

Both the MAC and $\varepsilon_g$ obtained by the proposed method have been compared with those obtained by adopting the other methods available in literature, and quoted in the Introduction. Although these methods are not specifically developed for these kind of applications, they are the most important techniques for ranking the interior modes available to date, and their effectiveness has been extensively proved.

#### 5.2.4.2 First test case: ultrasonic sonotrode

The theory proposed is firstly applied to the device shown in Fig.5.4(a), which is an ultrasonic sonotrode (or horn). Sonotrodes are, for example, employed in welding of plastics and nonferrous metals, cleaning, cutting, and so on. A sonotrode is one of the components of the so called ultrasonic stack, consisting of a piezoelectric transducer, a booster, and a sonotrode. Piezoelectric transducers are the actuators transforming electrical energy into high frequency mechanical vibrations, boosters amplify the amplitude of vibrations, and finally, sonotrodes, brought into contact with the workpieces, transfer mechanical vibrational energy from piezoelectric transducers to workpieces. All the components of the stack are tuned to resonate at the same ultrasonic frequency. For example, in plastic welding, application for which the experimental test-bed studied is designed, the ultrasonic stack is tuned to the eigenfrequency of sonotrode first longitudinal mode [123]. Therefore, transducer must be driven at a known frequency which should match, or be as

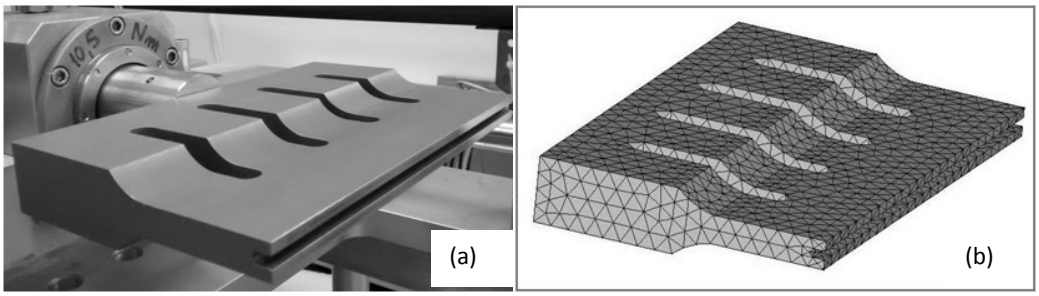


Figure 5.4: Ultrasonic horn investigated (a) and its finite element model (b)

close as possible to such an eigenfrequency.

In order to correctly model the sonotrode studied, some experimental measurements have been carried out, which have led to the identification of the correct properties of the sonotrode material (Titanium alloy Ta6V): mass density 4340 kg/m$^3$, Young's modulus 115 GPa, Poisson's ratio 0.32. Measurements have also corroborated the typical assumption that these systems are almost undamped. In particular, this assumption is confirmed by the experimental frequency response functions (FRFs) measured in the neighborhood of the sonotrode first longitudinal eigenfrequency (19886 Hz). An example of FRF is shown in Fig.5.5. This FRF represents the ratio between the velocity of one of a sample nodes at the sonotrode tip and the voltage exciting the piezoelectric transducer. A modal damping ratio $\xi = 0.01$ has been identified through the half-power method. Similar results (not shown here for brevity) have been obtained for the other nodes along the tip. The experimental setup adopted to estimate the experimental FRFs is shown in Fig.5.6 and is composed by:

- an Agilent 33220A waveform generator, used to drive the transducer through sine sweep voltage signals in the frequency range 19 kHz to 21 kHz;
- a Polytec laser Doppler vibrometer (LDV), used to measure the vibration velocities of the nodes at the sonotrode tip;
- a LMS SCADAS SCR02 acquisition system, interfaced to a PC running the proprietary software LMS Test.Lab for performing the experimental modal analysis.

A model of the sonotrode has been obtained through FEs by employing solid tetrahedral elements with eight nodes and three dofs (i.e. Cartesian coordinates) per node. In order to achieve an adequate accuracy in the representation of the system dynamics and to match the experimental response, it has been necessary to mesh the model very finely (see Fig. 5.4(b)). The resulting FE model has 8685 dofs. Clearly, handling such a large dimensional model, with mass and stiffness matrices of dimensions equal to the number of dofs is cumbersome, not only for their size, but also for the large condition

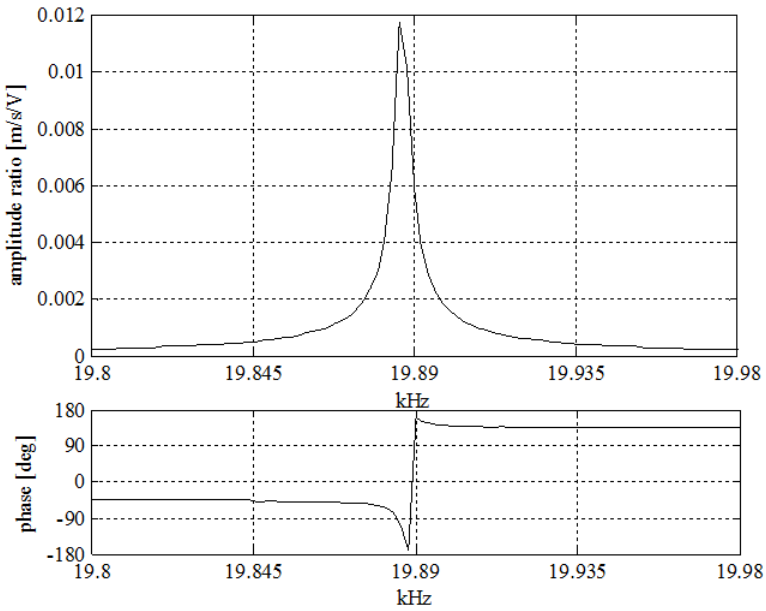


Figure 5.5: Experimental frequency response function

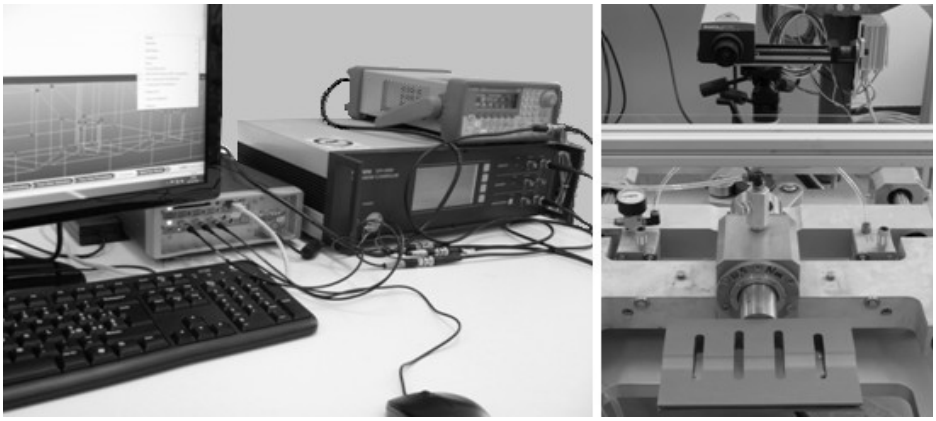

Figure 5.6: Experimental setup

number, which causes large ill conditioning whenever numerical algorithms for model based design are to be applied (see e.g. [77]).

Following the CB approach, a set of 21 Cartesian coordinates has been chosen as the master dofs, while the remaining 8664 coordinates are the slave dofs. The set of master dofs includes the displacements of the nodes lying at the physical interface between the sonotrode and the booster, through which

the mechanical vibrations are transmitted from the booster to the sonotrode. In particular, the force applied to such master dofs is a single-harmonic force whose spatial distribution along the longitudinal direction is uniform in all the nodes, while it is zero in the other directions. The force frequency $\omega$ is set almost equal to the natural eigenfrequency of the sonotrode first longitudinal mode ($\omega$ is not set equal to it, to avoid trivial numerical problems arising from exciting an undamped system at a natural frequency). The sonotrode is designed to respond to that force with uniform displacements along the tip to ensure regular welding.

The application of the EBR method leads to the results summarized in the logarithmic plot shown in Fig.5.7, where the two evaluation parameters defined in Section 5.2.4.1 are plotted as functions of the dimensions of the reduced-order models. In the same figure the evaluation parameters obtained by adopting the other ranking methods available in literature are plotted too. These models with increasing dimensions have been obtained by adding the interior modes progressively, following the ranking order provided by the methods investigated. The capability of the EBR method to ensure accu-

Table 5.3: Dimensions of the reduced models ensuring MAC$\geq$0.999 and $\varepsilon_g \leq$ 1% for each method

| Method | Reduced model dimensions | Order reduction ratio |
|---|---|---|
| EBR | 775 | 91.1% |
| $CMS_\chi$ | 1065 | 87.7% |
| EIM | 1086 | 87.5% |
| OMR | $>$1221 | - |
| SBE | 1169 | 86.6% |

racy through a minimum set of properly selected interior modes is clearly proved by the results obtained. Indeed, the convergence of the EBR method to the ideal results (i.e. MAC=1 and $\varepsilon_g$=0) outperforms the ones of the benchmark methods, which in turn, are more effective than the empirical sorting based on eigenfrequency. Table 5.3 collects some more results. For

instance it proves that, by adopting reasonable accuracy thresholds for the MAC and $\varepsilon_g$ of respectively 0.999 and 1%, a 775-dimensional model (with 21 master dofs and just 754 out of the 8664 interior modes) turns out to be adequate if the retained modes are selected through the EBR method. This leads to a percentage order reduction ratio (i.e. the ratio between the number of dofs neglected in the reduced model and the number of dofs of the full-order model) of 91.1%. Conversely, significantly higher model dimensions are needed to achieve the same accuracy through all the other benchmark methods. A further proof of the effectiveness of reducing the order of a dynamic model through the CB reduction technique together with the EBR method comes from a comparison with a FE model directly synthesized with a reduced set of dofs. Indeed, small size models might be also obtained by coarsening the mesh at the FE modeling stage. However, this approach usu-

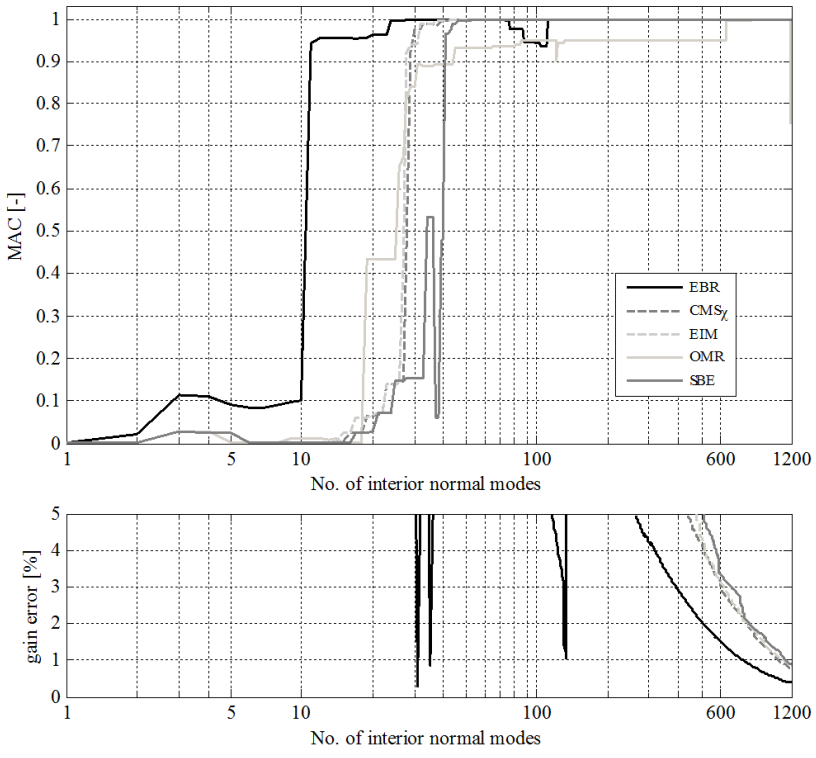


Figure 5.7: Logarithmic plot of MAC (top) and $\varepsilon_g$ (bottom) vs number of interior modes

ally results in a significant reduction of the model accuracy. For example, if the investigated horn is modeled with a coarse but rather uniform mesh resulting in a 1383 dof model (notice that these dofs are about twice the ones of the reduced model previously obtained by the EBR method), the longitudinal natural eigenfrequency computed through the system matrices is 20541 Hz. Such a result is affected by a considerable error of 3.3% in the estimation of the natural frequency of the first longitudinal mode. Conversely, the 775-dimensional model obtained through the proposed EBR method leads to a negligible 0.01% error in the estimation of the same frequency.

#### 5.2.4.3 Second test case: vibratory feeder

The second vibrating system to which the EBR method is applied is the one sketched in Fig.5.8. It represents a linear vibratory feeder, of the type usually employed in packaging or manufacturing plants for conveying small components or products.

The conveyed products move along the upper beam (the so called tray), forced by three concentrated electromagnetic exciters, modeled as three independent lumped masses connected to the beam through three linear springs. Six linear springs also connect the tray to a lower beam, which is a support beam, connected to the rigid frame by means of two elastic supports modeled as linear springs. Both the beams are modeled through a suitable number of four-dof Euler-Bernoulli beam finite elements (see Fig.5.8). The resulting model has 39 dofs.

The system is supposed to be excited by three in-phase forces, having

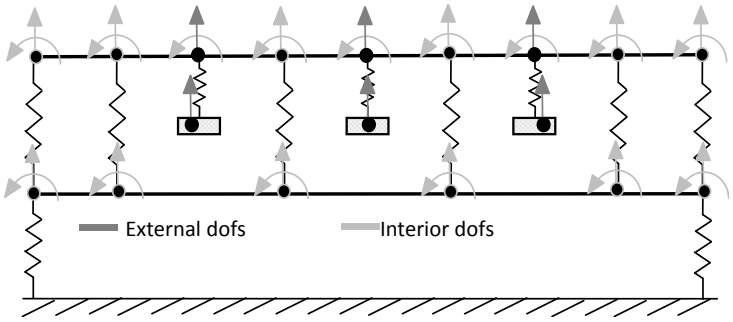


Figure 5.8: Finite element model of the vibratory feeder investigated

the same amplitude for all the six actuated dofs, which are chosen as the master dofs. Opposite directions are instead assumed for the forces exciting the three master dofs in the upper beam, and for those exciting the three lumped masses. Indeed, the electromagnetic exciters are usually driven by identical and in-phase periodic currents, so as to generate the proper motion of the tray and of the conveyed products.

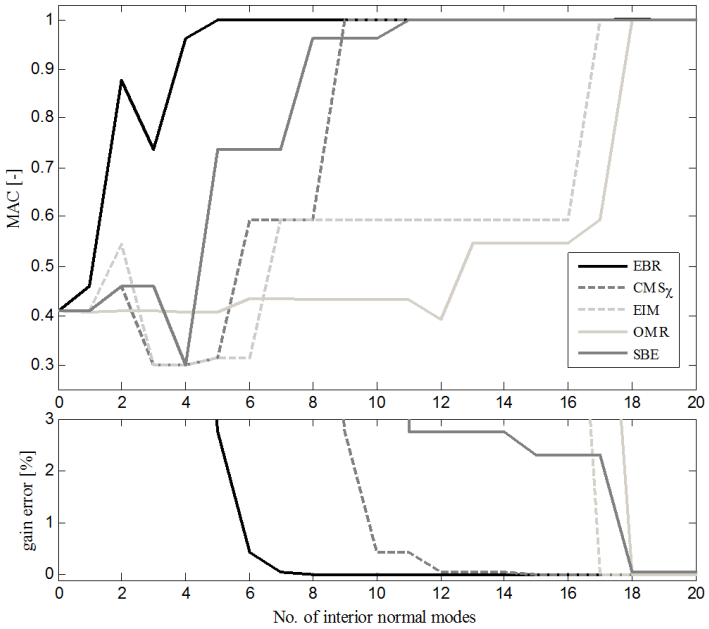


Figure 5.9: MAC (top) and $\varepsilon_g$ (bottom) vs number of interior modes

Table 5.4: Dimensions of the reduced models ensuring MAC$\geq$0.999 and $\varepsilon_g \leq$ 1% for each method

| Method | Reduced model dimensions | Order reduction ratio |
|---|---|---|
| EBR | 12 | 69.2% |
| CMS$_\chi$ | 16 | 59.0% |
| EIM | 23 | 41.0% |
| OMR | 24 | 38.4% |
| SBE | 24 | 38.4% |

Mode ranking and model reduction have been carried out focusing on the two harmonic components of the excitation force at 50 Hz and 100 Hz, which are the first two harmonic components due to the electromagnetic actuators forcing the system, and hence, the two harmonic components with respect to which maximum system response accuracy is required. The results of the investigation are summarized in Fig.5.9, where the two evaluation parameters are shown as functions of the reduced-order model dimensions.

As in the first test case, the EBR method outperforms the other benchmark techniques: a significantly smaller number of interior modes is needed to get a very accurate representation of the system forced response. Once again, Table5.4 summarizes the number of interior modes required by the different ranking strategies to meet the accuracy requirement of 0.999 for the MAC and of 1% for $\varepsilon_g$. This leads to a model order reduction ratio of 69.2%. The most effective among the other benchmark methods (i.e. the $\text{CMS}_\chi$) requires a number of modes that is 171% higher than the number of modes required by the EBR method.

## 5.3 Reduction of ERLS-based dynamic models

Up to now, with reference to linear systems, has been proved that the use of the CB method together with the proposed ranking methods allows keeping dynamic model dimensions to a minimum, while preserving model accuracy. The aim of this Section is to prove that the proposed reduction strategy, properly modified, is also suitable to reduce the dimensions of ERLS-based nonlinear dynamic models of flexible-link MBSs.

To achieve such a goal, first of all it is necessary to investigate how the CB method can be applied to MB models. Let us consider an $n$-dimensional dynamic model, having $n_q$ rigid dofs and $n_u$ elastic dofs, in the form of Eq.

4.23, and let us re-arrange it as follows:

$$\begin{bmatrix} \mathbf{M}(\mathbf{q}) & \mathbf{M}(\mathbf{q})\mathbf{S}(\mathbf{q}) \\ \mathbf{S}^{\mathrm{T}}(\mathbf{q})\mathbf{M}(\mathbf{q})) & \mathbf{S}^{\mathrm{T}}(\mathbf{q})\mathbf{M}(\mathbf{q})\mathbf{S} \end{bmatrix} \begin{bmatrix} \ddot{\mathbf{u}} \\ \ddot{\mathbf{q}} \end{bmatrix} + \\ + \begin{bmatrix} 2\mathbf{M}_G(\mathbf{q}) + \mathbf{C}(\mathbf{q}) & \mathbf{M}(\mathbf{q})\dot{\mathbf{S}}(\mathbf{q},\dot{\mathbf{q}}) \\ \mathbf{S}^{\mathrm{T}}(\mathbf{q})(2\mathbf{M}_G(\mathbf{q}) + \mathbf{C}(\mathbf{q})) & \mathbf{S}^{\mathrm{T}}(\mathbf{q})\mathbf{M}(\mathbf{q})\dot{\mathbf{S}}(\mathbf{q},\dot{\mathbf{q}}) \end{bmatrix} \begin{bmatrix} \dot{\mathbf{u}} \\ \dot{\mathbf{q}} \end{bmatrix} + \\ + \begin{bmatrix} \mathbf{K}(\mathbf{q}) & 0 \\ 0 & 0 \end{bmatrix} \begin{bmatrix} \mathbf{u} \\ \mathbf{q} \end{bmatrix} = \begin{bmatrix} \mathbf{M}(\mathbf{q}) & \mathbf{I} \\ (\mathbf{S}^{\mathrm{T}}(\mathbf{q})\mathbf{M}(\mathbf{q})) & \mathbf{S}(\mathbf{q})^{\mathrm{T}} \end{bmatrix} \begin{bmatrix} \mathbf{g}(\mathbf{q}) \\ \mathbf{f}(\mathbf{q}) \end{bmatrix} \tag{5.42}$$

In such a rearrangement the subscript *in* has been omitted and the matrix dependency on the ERLS generalized coordinates $\mathbf{q}$ has been stressed. Equation 5.42 clearly highlights that the dynamic model is a set of nonlinear equations with respect to the ERLS coordinates $\mathbf{q}$, and conversely, it is a set of linear configuration-varying equations with respect to the elastic coordinates $\mathbf{u}$. Therefore, with a few expedients it is still possible the use of both the CB method and of the developed ranking methods, although these are addressed to linear systems.

First of all, it is necessary to make the CB transformation matrix $\mathbf{H}$ a configuration-dependent matrix. As discussed in Section 5.1 the application of the CB method requires to split the dofs into master and slave dofs. In particular, all the ERLS coordinates (which express the system gross motion) have to be selected as master dofs. Indeed, such a selection leads to a linear configuration-varying subsystem of slave dofs, which allows applying modal analysis for the computation of the interior modes. The set of master dofs can also be expanded to include elastic coordinates, especially with reference to the elastic coordinates of those nodes where external forces may be applied or where sensors are located.

Let $\mathbf{u}_m \in \mathbb{R}^m$ and $\mathbf{u}_s \in \mathbb{R}^s$ $(m+s=n_u)$ be the elastic coordinates chosen, respectively, as master and slave, the partitioned form of the motion equation

in Eq. 5.42 can be written as:

$$\left[\begin{array}{c|cc} \mathbf{S}^{\mathrm{T}}\mathbf{M}\mathbf{S} & \mathbf{S}^{\mathrm{T}}\begin{bmatrix}\mathbf{M}_{mm}\\ \mathbf{M}_{sm}\end{bmatrix} & \mathbf{S}^{\mathrm{T}}\begin{bmatrix}\mathbf{M}_{sm}\\ \mathbf{M}_{ss}\end{bmatrix} \\ \hline \begin{bmatrix}\mathbf{M}_{mm} & \mathbf{M}_{ms}\end{bmatrix}\mathbf{S} & \mathbf{M}_{mm} & \mathbf{M}_{ms} \\ \hline \begin{bmatrix}\mathbf{M}_{sm} & \mathbf{M}_{ss}\end{bmatrix}\mathbf{S} & \mathbf{M}_{sm} & \mathbf{M}_{ss} \end{array}\right] \left\{\begin{array}{c}\ddot{\mathbf{q}}\\ \hline \ddot{\mathbf{u}}_m\\ \hline \ddot{\mathbf{u}}_s\end{array}\right\} + \tag{5.43}$$

$$+\left[\begin{array}{c|cc} \mathbf{S}^{\mathrm{T}}\mathbf{M}\dot{\mathbf{S}} & \mathbf{S}^{\mathrm{T}}\begin{bmatrix}2\mathbf{M}_{G_{mm}}+\mathbf{C}_{mm}\\ 2\mathbf{M}_{G_{sm}}+\mathbf{C}_{sm}\end{bmatrix} & \mathbf{S}^{\mathrm{T}}\begin{bmatrix}2\mathbf{M}_{G_{sm}}+\mathbf{C}_{sm}\\ 2\mathbf{M}_{G_{ss}}+\mathbf{C}_{ss}\end{bmatrix} \\ \hline \begin{bmatrix}\mathbf{M}_{mm} & \mathbf{M}_{ms}\end{bmatrix}\dot{\mathbf{S}} & 2\mathbf{M}_{G_{mm}}+\mathbf{C}_{mm} & 2\mathbf{M}_{G_{ms}}+\mathbf{C}_{ms} \\ \hline \begin{bmatrix}\mathbf{M}_{sm} & \mathbf{M}_{ss}\end{bmatrix}\dot{\mathbf{S}} & 2\mathbf{M}_{G_{sm}}+\mathbf{C}_{sm} & 2\mathbf{M}_{G_{ss}}+\mathbf{C}_{ss} \end{array}\right] \left\{\begin{array}{c}\dot{\mathbf{q}}\\ \hline \dot{\mathbf{u}}_m\\ \hline \dot{\mathbf{u}}_s\end{array}\right\} +$$

$$+\left[\begin{array}{c|cc} \mathbf{0} & \mathbf{0} & \mathbf{0} \\ \mathbf{0} & \mathbf{K}_{mm} & \mathbf{K}_{ms} \\ \hline \mathbf{0} & \mathbf{K}_{sm} & \mathbf{K}_{ss} \end{array}\right] \left\{\begin{array}{c}\mathbf{q}\\ \hline \mathbf{u}_m\\ \hline \mathbf{u}_s\end{array}\right\} = \left[\begin{array}{c|cc} \mathbf{S}^{\mathrm{T}} & \mathbf{S}^{\mathrm{T}}\begin{bmatrix}\mathbf{M}_{mm}\\ \mathbf{M}_{sm}\end{bmatrix} & \mathbf{S}^{\mathrm{T}}\begin{bmatrix}\mathbf{M}_{sm}\\ \mathbf{M}_{ss}\end{bmatrix} \\ \hline \mathbf{I} & \mathbf{M}_{mm} & \mathbf{M}_{ms} \\ \hline \mathbf{I} & \mathbf{M}_{sm} & \mathbf{M}_{ss} \end{array}\right] \left\{\begin{array}{c}\mathbf{f}\\ \hline \mathbf{g}_m\\ \hline \mathbf{g}_s\end{array}\right\}$$

Consistently with the block matrices delimited by the dashed lines, Eq. 5.43 is rewritten in a more compact formulation:

$$\begin{bmatrix}\overline{\mathbf{M}}_{11}(\mathbf{q}) & \overline{\mathbf{M}}_{12}(\mathbf{q})\\ \overline{\mathbf{M}}_{21}(\mathbf{q}) & \overline{\mathbf{M}}_{22}(\mathbf{q})\end{bmatrix}\begin{Bmatrix}\ddot{\mathbf{x}}_1\\ \ddot{\mathbf{u}}_s\end{Bmatrix} + \begin{bmatrix}\overline{\mathbf{C}}_{11}(\mathbf{q},\dot{\mathbf{q}}) & \overline{\mathbf{C}}_{12}(\mathbf{q},\dot{\mathbf{q}})\\ \overline{\mathbf{C}}_{21}(\mathbf{q},\dot{\mathbf{q}}) & \overline{\mathbf{C}}_{22}(\mathbf{q},\dot{\mathbf{q}})\end{bmatrix}\begin{Bmatrix}\dot{\mathbf{x}}_1\\ \dot{\mathbf{u}}_s\end{Bmatrix} +$$

$$+\begin{bmatrix}\overline{\mathbf{K}}_{11}(\mathbf{q}) & \overline{\mathbf{K}}_{12}(\mathbf{q})\\ \overline{\mathbf{K}}_{21}(\mathbf{q}) & \overline{\mathbf{K}}_{22}(\mathbf{q})\end{bmatrix}\begin{Bmatrix}\mathbf{x}_1\\ \mathbf{u}_s\end{Bmatrix} = \begin{bmatrix}\overline{\mathbf{L}}_{11}(\mathbf{q}) & \overline{\mathbf{M}}_{12}(\mathbf{q})\\ \overline{\mathbf{L}}_{21}(\mathbf{q}) & \overline{\mathbf{M}}_{22}(\mathbf{q})\end{bmatrix}\begin{Bmatrix}\mathbf{f}_1\\ \mathbf{g}_s\end{Bmatrix} \tag{5.44}$$

where $\mathbf{x}_1$ is the vector of master dofs ($\mathbf{x}_1 = \{\mathbf{q}^{\mathrm{T}} \quad \mathbf{u}_1^{\mathrm{T}}\}^{\mathrm{T}}$).

In order to define the CB matrix transformation, the Guyan's basis $\mathbf{B}$ and the eigenvector matrix of the interior modes $\mathbf{\Phi}$ should be identified.

The Guyan's condensation is defined as:

$$\mathbf{B} = -\overline{\mathbf{K}}_{22}^{-1}\overline{\mathbf{K}}_{21} \tag{5.45}$$

Typically $\mathbf{B}$ is a constant matrix, but since dynamic models of flexible-link MBSs are configuration-dependent, here it is defined as a configuration-dependent matrix. By making use of Eq. 5.43, Eq. 5.45 can be rearranged as:

$$\mathbf{B}(\mathbf{q}) = -\mathbf{K}_{ss}^{-1}(\mathbf{q}) \begin{bmatrix} \mathbf{0} & \mathbf{K}_{sm}(\mathbf{q}) \end{bmatrix} = \begin{bmatrix} \mathbf{0} & -\mathbf{K}_{ss}^{-1}(\mathbf{q})\mathbf{K}_{sm}(\mathbf{q}) \end{bmatrix} \tag{5.46}$$

Such a new definition of the Guyan's matrix requires to known the inverse of $\mathbf{K}_{ss} \in \mathbb{R}^{s\text{x}s}$ for each value of the ERLS generalized coordinates $\mathbf{q}$. $\mathbf{K}_{ss}$ is a stiffness matrix arising from a FE model, therefore it is typically a block, and sparse matrix. As a consequence, the inverse of $\mathbf{K}_{ss}$ can be easily computed analytically in advance (pre-processed) by means of Schur Complements or other well-known linear algebra methods [124]. Once an analytical formulation of $\mathbf{K}_{ss}^{-1}$ is available it is possible to set an analytical configuration-dependent formulation of $\mathbf{B}$. However, if the number of slave dofs $s$ is big, it might not possible, or at least it could be not convenient, to compute the inverse of $\mathbf{K}_{ss}$ analytically. Numerical methods should hence be employed. In this case, matrix inversion must be performed for each variation of $\mathbf{q}$. Although such an operation decreases the computational efficiency of the reduced model, the use of reduced models is generally still extremely advantageous compared to the use of full-order models. This point will be clarified in the next Chapter.

The computation of the interior vibrational modes $\boldsymbol{\phi}$ requires the selection of a reference configuration $\mathbf{q}^*$. Indeed, they are calculated by solving the eigenvalue problem of the system obtained by constraining the master dofs, posing the ERLS at the configuration $\mathbf{q}^*$ and by putting its motion to zero, so that $\dot{\mathbf{q}} = \ddot{\mathbf{q}} = \mathbf{0}$:

$$\left(\overline{\mathbf{K}}_{22}(\mathbf{q}^*) - \omega_i \overline{\mathbf{M}}_{22}(\mathbf{q}^*)\right) \boldsymbol{\phi}_i = \mathbf{0}, \quad i = 1, \ldots, s \tag{5.47}$$

$$\boldsymbol{\Phi} = \begin{bmatrix} \boldsymbol{\phi}_1 & \ldots & \boldsymbol{\phi}_i & \ldots & \boldsymbol{\phi}_s \end{bmatrix}, \quad \boldsymbol{\Phi}^{\mathrm{T}} \overline{\mathbf{M}}_{22}(\mathbf{q}^*) \boldsymbol{\Phi} = \mathbf{I}, \quad \boldsymbol{\Phi}^{\mathrm{T}} \overline{\mathbf{K}}_{22}(\mathbf{q}^*) \boldsymbol{\Phi} = \boldsymbol{\Omega}$$

$\boldsymbol{\Omega}$ is a diagonal matrix whose entries are the squared angular eigenfrequencies of the constrained system.

Although under the hypothesis of small deformations, which is the same on which the ERLS formulation is based, the system eigenvectors change

very slowly (i.e. they are almost the same for different system configurations) matrix $\mathbf{\Phi}$ has only a local validity, since during any motion the mass and stiffness matrices vary. Therefore, the interior modes computed at the configuration cannot be used in other configurations, this means that they should be recomputed for each system configuration, which is a computationally expensive operation.

This apparent incongruence is due to the definition of the elastic variables, indeed, they are expressed with reference to an ERLS, which is an equivalent mechanism that follows the rigid motion of the flexible-link MBSs, so when the system moves, the ERLS moves too, and the elastic coordinates are redefined in the new ERLS.

In order to use the interior modes computed at a reference configuration in a large configuration space, they have to be projected onto the actual ERLS-based coordinates.

Let $\mathbf{R} \in \mathbb{R}^{sxs}$ be a block-diagonal matrix expressing the transformation of the slave dofs from the local reference frames of each finite element to the global one, the new configuration-dependent interior mode matrix $\mathbf{\Psi}$ has the following expression:

$$\mathbf{\Psi}(\mathbf{q}) = \mathbf{R}^{\mathrm{T}}(\mathbf{q})\mathbf{R}(\mathbf{q}^*)\mathbf{\Phi}(\mathbf{q^*}) = \mathbf{R}(\mathbf{q}-\mathbf{q}^*)\mathbf{\Phi}(\mathbf{q^*}) \tag{5.48}$$

where $\mathbf{q}$ is the current system configuration and $\mathbf{q}^*$ the reference one, at which $\mathbf{\Phi}$ has been computed.

In order to reduce model dimension, the set of interior modes should be truncated. To this end the most important interior modes, $\widetilde{\mathbf{\Psi}} \in \mathbb{R}^{sx\tau}$, $\tau << s$, at reference configuration are selected according to the ranking method that best meets the specific design requirements in the use of models, among the ones presented in Section 5.2.

Therefore, a configuration-dependent CB reduction matrix can be synthesized and the model reduced as shown below:

$$\mathbf{H}(\mathbf{q}) = \begin{bmatrix} \mathbf{I} & \mathbf{0} \\ \mathbf{B}(\mathbf{q}) & \widetilde{\mathbf{\Psi}}(\mathbf{q}) \end{bmatrix} \tag{5.49}$$

$$\mathbf{H}^{\mathrm{T}}(\mathbf{q})\overline{\mathbf{M}}(\mathbf{q})\mathbf{H}(\mathbf{q})\begin{Bmatrix}\ddot{\mathbf{x}}_1\\ \ddot{\boldsymbol{\eta}}\end{Bmatrix}+\mathbf{H}^{\mathrm{T}}(\mathbf{q})\overline{\mathbf{C}}(\mathbf{q},\dot{\mathbf{q}})\mathbf{H}(\mathbf{q})\begin{Bmatrix}\dot{\mathbf{x}}_1\\ \dot{\boldsymbol{\eta}}\end{Bmatrix}+$$
$$+\mathbf{H}^{\mathrm{T}}(\mathbf{q})\overline{\mathbf{K}}(\mathbf{q})\mathbf{H}(\mathbf{q})\begin{Bmatrix}\mathbf{x}_1\\ \boldsymbol{\eta}\end{Bmatrix}=\mathbf{H}^{\mathrm{T}}(\mathbf{q})\overline{\mathbf{L}}(\mathbf{q})\begin{Bmatrix}\mathbf{f}_1\\ \mathbf{g}_1\end{Bmatrix} \tag{5.50}$$

where vector $\boldsymbol{\eta}\in\mathbb{R}^{\tau}$ collects the modal coordinates associated to the retained interior modes. The resulting reduced-order model is able to represent the nonlinearities of the full-order model, its dependence on configuration, and to capture correctly the system dynamics in a neighborhood of the reference configuration.

In order to verify the accuracy of the reduced model far from the reference configuration, a simple analysis can be made. In particular, since the interior modes have been normalized with respect to the mass matrix (see Eq. 5.47), straightforward od the model consistency may be based on verifying that the projected interior modes are still $\overline{\mathbf{M}}_{22}$-orthogonal:

$$\widetilde{\boldsymbol{\Phi}}^{\mathrm{T}}\mathbf{R}^{\mathrm{T}}(\mathbf{q}-\mathbf{q}^{*})\overline{\mathbf{M}}_{22}(\mathbf{q})\mathbf{R}^{\mathrm{T}}(\mathbf{q}-\mathbf{q}^{*})\widetilde{\boldsymbol{\Phi}}\cong\mathbf{I} \tag{5.51}$$

When the verification in Eq. 5.51 fails, the matrix of interior modes $\boldsymbol{\Phi}$ must be calculated in a new reference configuration. The switch from a matrix to another can be regulated through switching model methods.

## 5.4 Reduction of ERLS-based dynamic models: validation and assessment

The new reduction strategy, based on a modified formulation of the CB method and on the ranking methods presented in Section 5.2, has been validated by applying it to the reduction of the model of the planar manipulator with flexible links and driven by three motors, already discussed in in Section 4.2.

In this Chapter and in the next one, the system will however be considered lying in the horizontal plane, therefore neglecting gravity and the elastic forces exerted by the contrast springs, which only marginally affect the system dynamics. The marginality of the neglected contributions on

Table 5.5: System eigenfrequenies in ascending order

| | | | |
|---|---|---|---|
| RIGID | 1 | 0 | [Hz] |
| MODES | 2 | 0 | [Hz] |
| | 3 | 0 | [Hz] |
| | 1 | 14.2 | [Hz] |
| | 2 | 43.5 | [Hz] |
| | 3 | 67.0 | [Hz] |
| ELASTIC | 4 | 129.1 | [Hz] |
| MODES | 5 | 147.3 | [Hz] |
| | 6 | 170.0 | [Hz] |
| | 7 | 205.0 | [Hz] |
| | 8 | 267.5 | [Hz] |
| | ... | ... | ... |

manipulator dynamics is evident by comparing the eigenfrequencies listed in Tab. 5.5 (referred to a horizontal plane) with the ones computed in the previous Chapter (referred to a vertical plane).

The full-order dynamic model synthesized for such a manipulator has 30 dofs, of which 3 are rigid and 27 elastic. The aim is to get a reduced model capable to represent correctly the system dynamics in the frequency range 0-180 Hz, basically, corresponding to motor bandwidth and to the range within which active vibration control could be reasonably achieved.

This requirement leads to chose the IMR method (see Section 5.2.1) to select an adequate subset of interior modes. Indeed, this method allows representing accurately the system dynamics in a given frequency range. In particular, it selects the interior modes with the highest contribution to the system vibration modes in the frequency range of interest.

First of all, let us identify how many and which modes should be represented correctly in order to meet the requirement. Table 5.5 shows the system eigenfrequencies sorted by increasing values. In the frequency range of interest there are 3 rigid modes and 6 elastic modes. As far as the rigid modes are concerned, they are always represented correctly, since the rigid body variables are all collected in the master dofs. Therefore, in order to

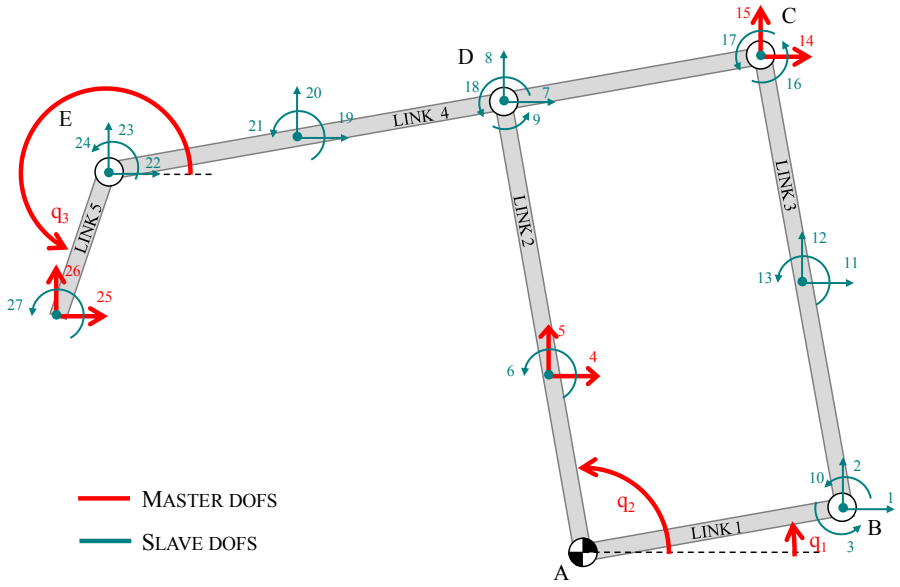


Figure 5.10: Division into master and slave degrees of freedom

satisfy the test aim, the first 6 elastic eigenvectors of the system must be properly approximated by the chosen subset of interior modes.

Figure 5.10 shows the master dofs selected, which are the three angular positions of the cranks; the linear deformations of the tip; and other four elastic coordinates, which will be useful in the next state estimation stage (see Chapter 6). Therefore the 30 dofs are split into 9 master dofs and 21 slave dofs.

After the application of the proposed reduction strategy (modified CB and IMR) very good level of accuracy has been achieved with a model with just 13 dofs, i.e. 4 out of 21 slave dofs. As a consequence the model dimension has been reduced by 56%, while guaranteeing a perfect match between the dynamics of interest represented by the full-order model and the reduced one. This can be inferred by Figs. from 5.11 to 5.16. Such figures show for each mode in the frequency range of interest the two evaluation parameters defined in Section 5.2.2.1: the NCO between the eigenvectors of the full and the reduced models, on the left; the frequency error between the eigenfrequencies of the full-order model and the reduced-order one, on the right. For

clarity of representation, the indices are plotted vs just two coordinates, ($q_3$ is constant), however, very similar results have been obtained when all the coordinates vary.

An example of reduced model has been synthesized at reference configuration $\mathbf{q} = \{1.0821 \;\; 2.6354 \;\; 4.7123\}^{\mathrm{T}}$ [rad], indicated by a red point in each plot. Then, the model has been evaluated in a neighborhood of such a configuration. It is worth noticing that in each plot both the coordinates $q_1$ and $q_2$ have been varied from the values at the reference configuration of $\pm 0.5$ rad. Apparently such changes do not affect evaluation indices considerably: they keep a values very close to their target values.

Therefore, it is proved that the 13-dof reduced model represents correctly the dynamics of interest in a wide configuration space.

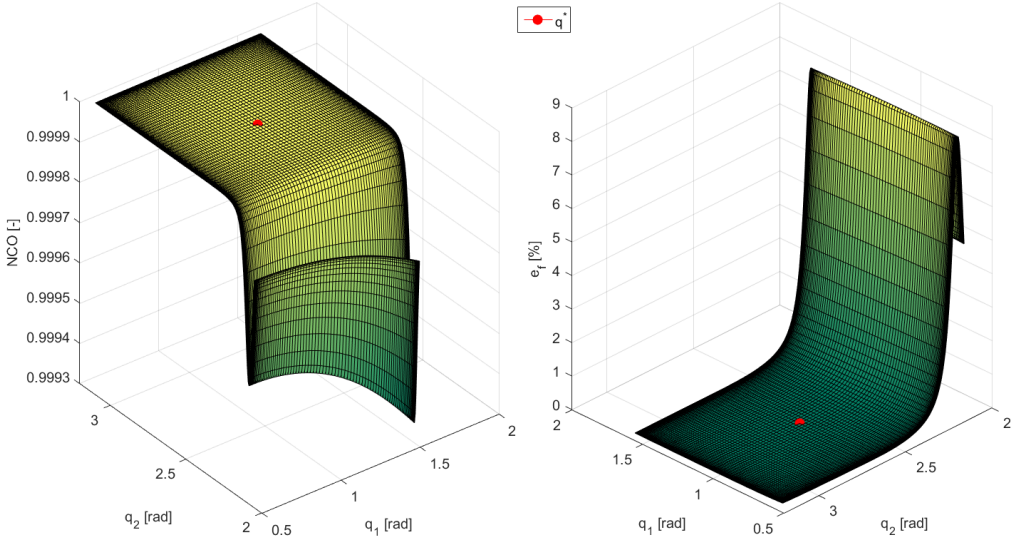


Figure 5.11: 1st vibration mode: NCO (left), $e_f$ (right)

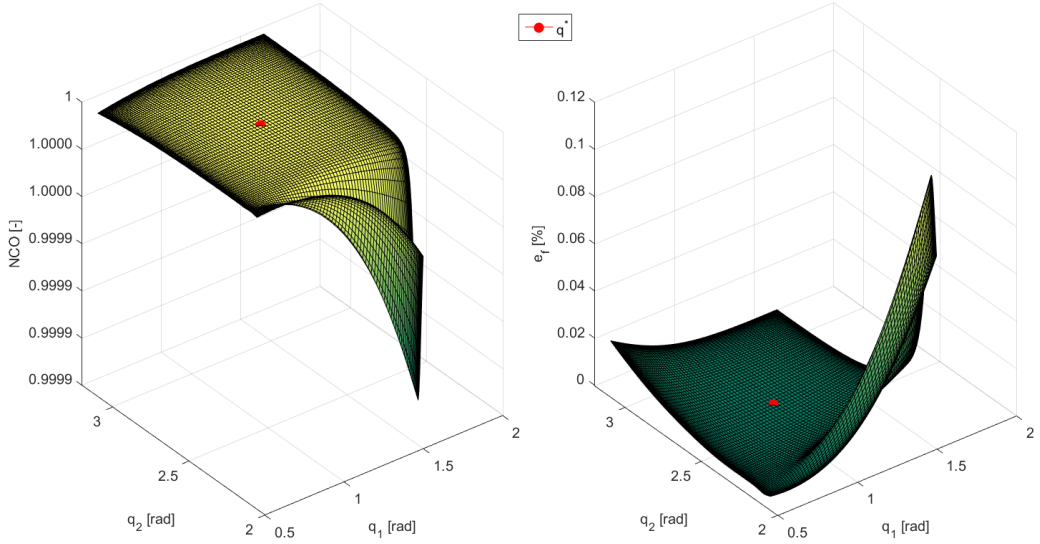


Figure 5.12: 2nd vibration mode: NCO (left), $e_f$ (right)

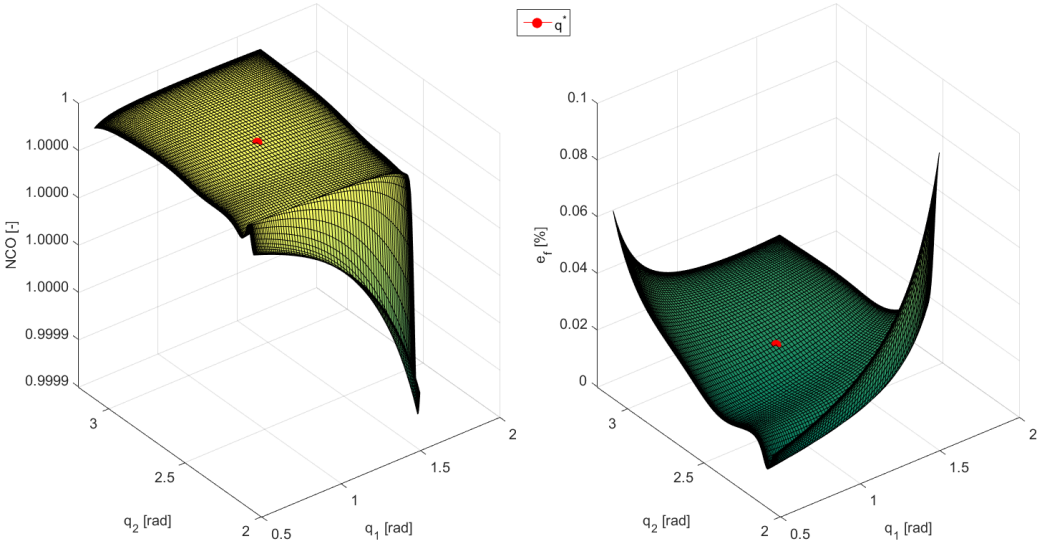


Figure 5.13: 3rd vibration mode: NCO (left), $e_f$ (right)

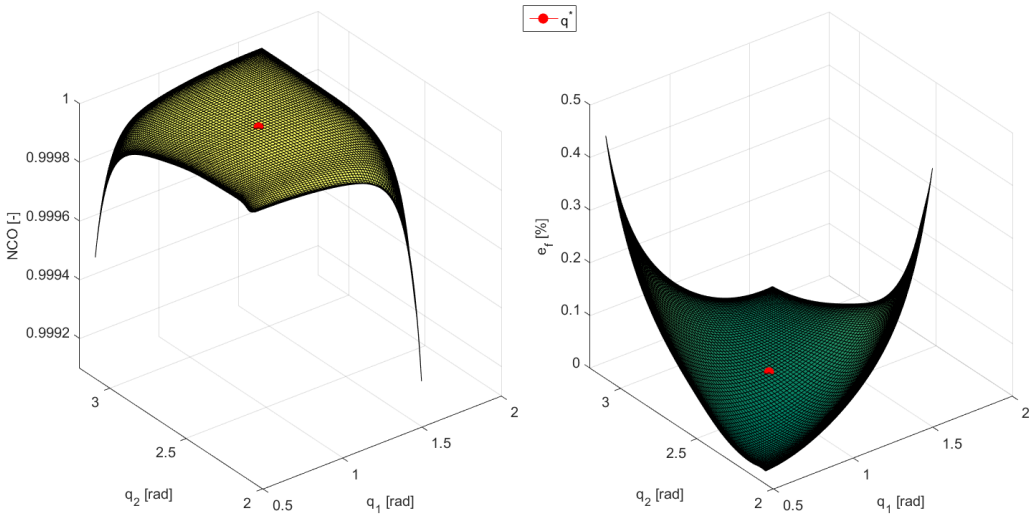


Figure 5.14: $4^{\text{th}}$ vibration mode: NCO (left), $e_f$ (right)

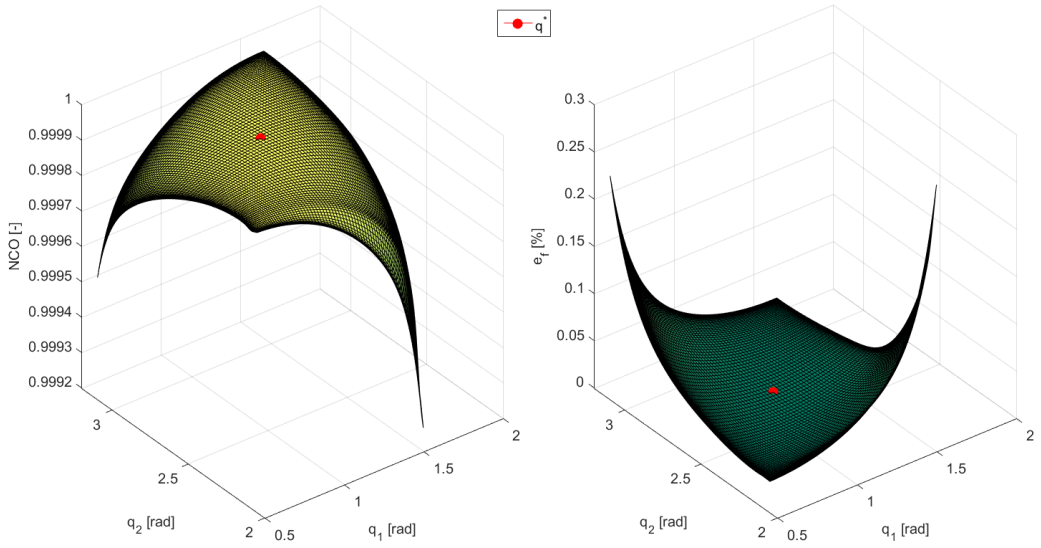


Figure 5.15: $5^{\text{th}}$ vibration mode: NCO (left), $e_f$ (right)

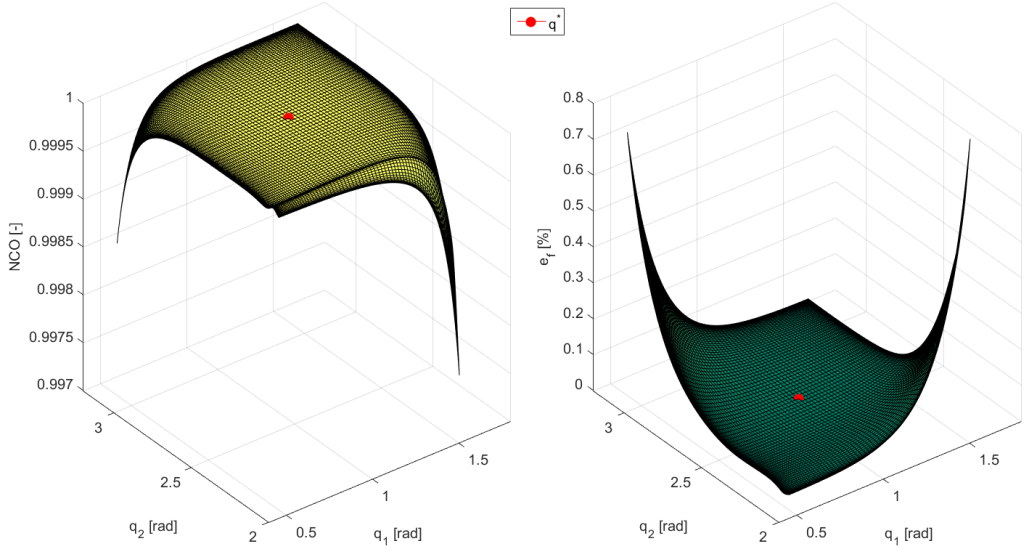


Figure 5.16: $6^{\text{th}}$ vibration mode: NCO (left), $e_f$ (right)

## 5.5 Chapter summary

Two new ranking methods, IMR and EBR, are introduced for the ranking and selection of the interior modes to be retained in a model reduction strategy based on the CB technique. The methods address two different goals:

- The IMR method aims at accurately describing the dynamics of a linear vibrating system at a specific frequency or in a frequency range of interest.

- The EBR method aims at providing a reliable description of the forced response of a linear vibrating system in the presence of a periodic force whose frequency content and spatial distribution are known, as it is often the case in vibrating systems of industrial interest.

Both the methods are based on some newly and analytically defined indices, which provide comparative evaluation of the interior modes relevance, based on:

- IMR: the contributions of each interior mode to the shape and frequency of each vibrational mode of interest of the full-order system.
- EBR: the contribution of each interior mode to the mean mechanical energy stored by the full-order system in a period of the external force.

The effectiveness of these methods has been proved by applying them to different devices. It has been shown that such methods ensure very effective model reduction. Additionally method effectiveness has been also corroborated through the comparison with other "general purpose" ranking techniques available in literature. It has been proved that, in all the cases investigated, the proposed raking methods achieve the desired levels of accuracy with minimal sets of interior modes, always considerably smaller than the ones of the other benchmark methods.

The Chapter presents also a new strategy to perform the reduction at system level of dynamic models based on the ERLS. In particular, such a new strategy makes use of the well-known CB method suitably modified (in order to cope with nonlinearities of flexible MB models) and of the developed ranking methods.

The new strategy leads to the formulation of a configuration-dependent reduction transformation capable of representing the nonlinearities of the full-order model, and its dependence on configuration. The proposed strategy has been validated by applying it to the reduction of the model of the planar manipulator with flexible links and driven by three motors presented in Chapter 4. Once again, the results obtained are fully satisfactory, since it was possible to demonstrate that the developed technique, in the case taken into consideration, leads to a significant reduction in the size of the models and an appropriate representation of the system dynamics in the frequency range of interest.

Hence a suitable strategy to reduce the dimensions of MBS dynamic models has been developed. This pones the way to efficient state estimation, which is addressed in the next Chapter.

# Chapter 6

# State estimation in Flexible-link MBSs

In this Chapter the implementation of a state observer, for the nonlinear flexible-link MBS presented in Chapter 4, is performed. The observer is synthesized adopting the EKF algorithm discussed in Chapter 1 and the reduced order model obtained by applying the method suggested in Chapter 5. The validation of the observer is carried out by means of a simulated test in Matlab. Nonetheless, it has been simulated the motion of the real manipulator through the full-order model but the observer is based on the reduced-order manipulator model and the magnitudes that correspond to sensor data are passed to the observer with their respective noises and sample rates. Such a test allows a more accurate assessment of observer outcomes. Indeed, simulation provides all the manipulator state variables, including the elastic ones, which cannot be measured experimentally.

## 6.1 State-space representation

In Chapter 5 the manipulator model has been reduced from 30 to 13 dofs. In particular, the new coordinate vector $\mathbf{z} = \{\mathbf{x}_1^{\mathrm{T}} \ \boldsymbol{\eta}^{\mathrm{T}}\}^{\mathrm{T}}$ contains 9 physical dofs and 4 interior modal coordinates. The physical dofs retained in the reduced model, i.e. the master dofs, are the following ones, also shown in Fig. 6.1 :

$$\mathbf{x}_1 = \begin{Bmatrix} \mathrm{q}_1 & \mathrm{q}_2 & \mathrm{q}_3 & \mathrm{x}_4 & \mathrm{y}_5 & \mathrm{x}_{14} & \mathrm{y}_{15} & \mathrm{x}_{25} & \mathrm{x}_{26} \end{Bmatrix}^{\mathrm{T}} \tag{6.1}$$

The state of such a system is defined as:

$$\mathbf{w} = \begin{Bmatrix} \mathbf{z} \\ \dot{\mathbf{z}} \end{Bmatrix} = \begin{Bmatrix} \dot{\mathbf{x}}_1 \\ \dot{\boldsymbol{\eta}} \\ \ddot{\mathbf{x}}_1 \\ \ddot{\boldsymbol{\eta}} \end{Bmatrix} \tag{6.2}$$

Consequently, the first-order formulation of the reduce-order motion equation in Eq. 5.50 takes the following form:

$$\begin{Bmatrix} \dot{\mathbf{z}} \\ \ddot{\mathbf{z}} \end{Bmatrix} = \begin{bmatrix} \mathbf{0} & \mathbf{I} \\ -\widetilde{\mathbf{M}}^{-1}(\mathbf{q})\widetilde{\mathbf{K}}(\mathbf{q}) & -\widetilde{\mathbf{M}}^{-1}(\mathbf{q})\widetilde{\mathbf{C}}(\mathbf{q},\dot{\mathbf{q}}) \end{bmatrix} \begin{Bmatrix} \mathbf{z} \\ \dot{\mathbf{z}} \end{Bmatrix} + \begin{bmatrix} \mathbf{0} \\ \widetilde{\mathbf{M}}^{-1}(\mathbf{q})\widetilde{\mathbf{L}}(\mathbf{q}) \end{bmatrix} \{\mathbf{F}\} \tag{6.3}$$

where the over-posed tilde denotes the reduced-order matrices:

$$\begin{aligned} \widetilde{\mathbf{M}}(\mathbf{q}) &:= \mathbf{H}^{\mathrm{T}}(\mathbf{q})\overline{\mathbf{M}}(\mathbf{q})\mathbf{H}(\mathbf{q}) \qquad & \widetilde{\mathbf{C}}(\mathbf{q},\dot{\mathbf{q}}) &:= \mathbf{H}^{\mathrm{T}}(\mathbf{q})\overline{\mathbf{C}}(\mathbf{q},\dot{\mathbf{q}})\mathbf{H}(\mathbf{q}) \\ \widetilde{\mathbf{K}}(\mathbf{q}) &:= \mathbf{H}^{\mathrm{T}}(\mathbf{q})\overline{\mathbf{K}}(\mathbf{q})\mathbf{H}(\mathbf{q}) \qquad & \widetilde{\mathbf{L}}(\mathbf{q}) &:= \mathbf{H}^{\mathrm{T}}(\mathbf{q})\overline{\mathbf{L}}(\mathbf{q}) \end{aligned} \tag{6.4}$$

In Eq. 6.3 the gravity forces and the elastic ones exerted by the contrast spring have been neglected, since the manipulator is considered lying in the horizontal plane. The continuous-time system equation in 6.3 has been discretized by using the fourth-order Runge-Kutta method and an integration step of 0.1 ms.

The inputs of the model in Eq. 6.3 are all the forces acting on the system, collected in the vector $\mathbf{F}$. With reference to the manipulator studied, the inputs are the torques exerted by the three motors:

$$\mathbf{F} = \begin{Bmatrix} \mathrm{T}_1 & \mathrm{T}_2 & \mathrm{T}_3 & 0_4 & \dots & 0_{13} \end{Bmatrix}^{\mathrm{T}} \tag{6.5}$$

Finally, to represent the system in a state space formulation also the outputs, and hence the measurement equations should be defined. Six sensed outputs have been employed, i.e. the angular positions of the three actuated links and the curvature of the midpoints of links 1, 2 and 4:

$$\mathbf{y} = \begin{Bmatrix} \mathrm{q}_1 & \mathrm{q}_2 & \mathrm{q}_3 & \gamma_1 & \gamma_2 & \gamma_4 \end{Bmatrix}^{\mathrm{T}} \tag{6.6}$$

From such a choice of the output variables it is evident that the measurement equations result in a nonlinear function of the state variables ($\mathbf{y} = \mathbf{g}(\mathbf{z})$), indeed, only $q_1$, $q_2$, and $q_3$, are a linear combination of the state variables.

A thorough observability analysis for such a system has been computed in [125] employing a linearized observability analysis in the whole manipulator workspace. In such an analysis has been proved that the aforementioned set of output variables guarantees system observability.

Figure 6.1 schematically represents all the physical variables involved in the state space representation, and hence in the estimation process.

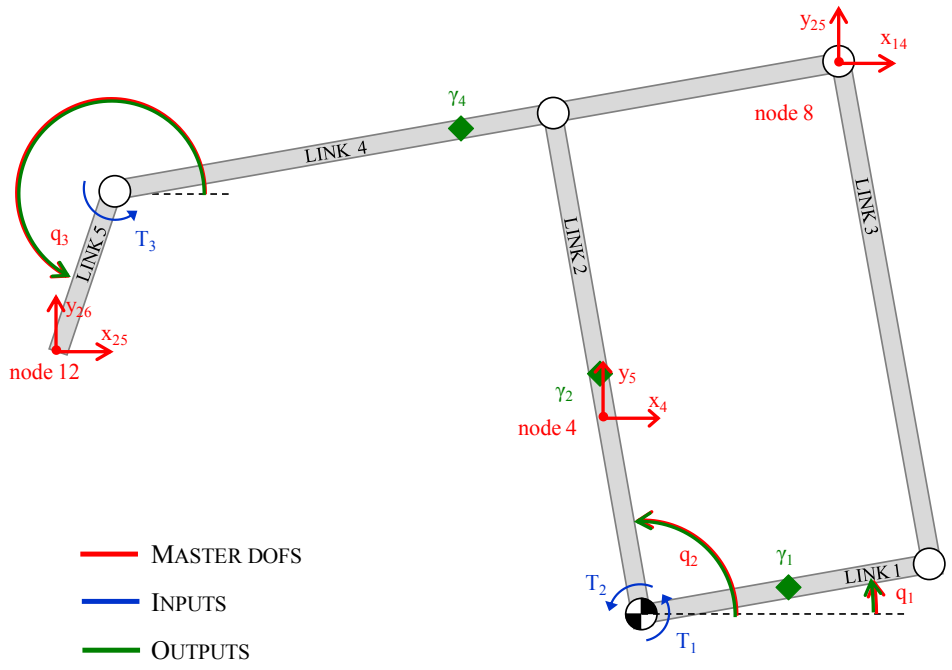


Figure 6.1: Variables involved in the estimation process

## 6.2 Observer validation

A simulation lasting 3 seconds has been tested, which highlights that no drift affect the estimates, i.e the observer is stable. In particular, three sinusoidal

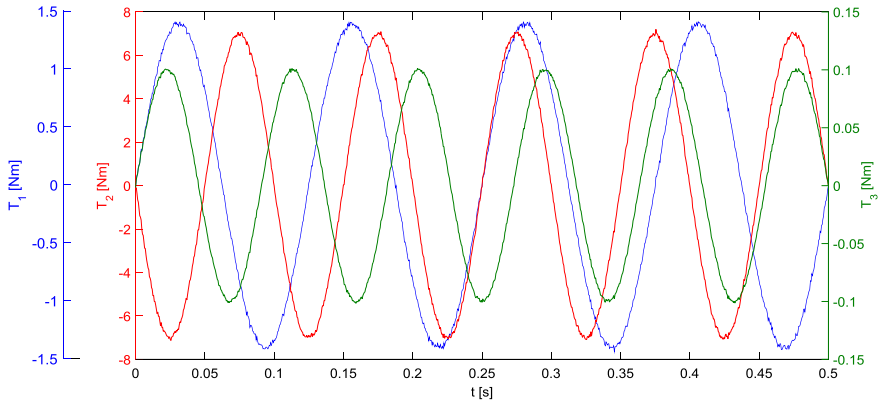


Figure 6.2: Actuation torques feed as inputs to the observer

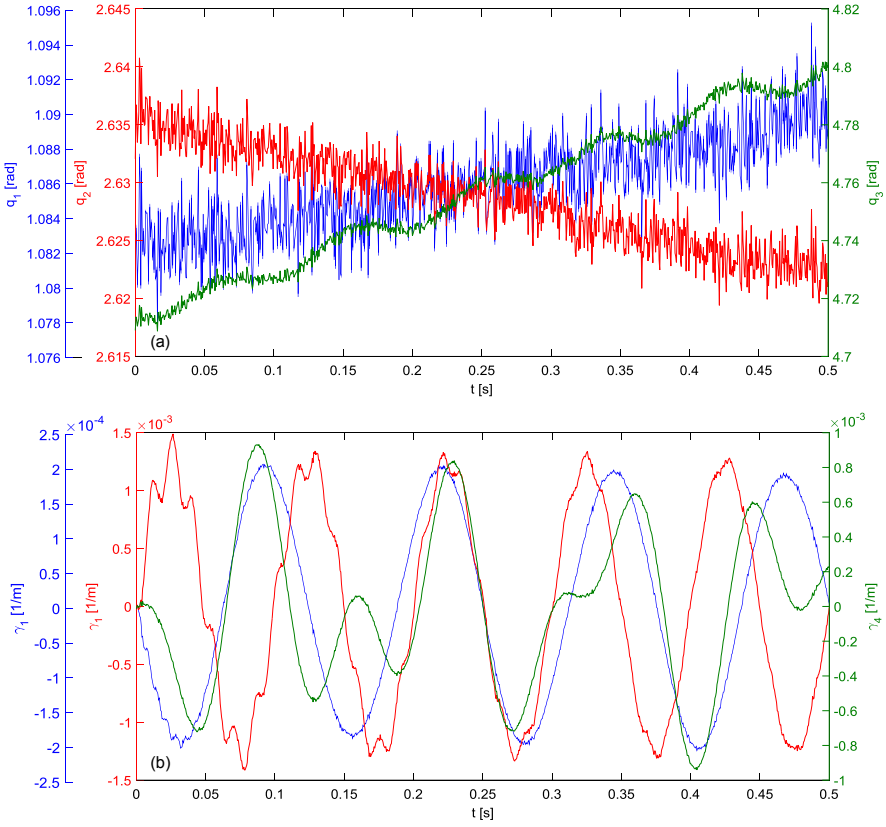


Figure 6.3: Observer outputs: angular positions of the actuated links (a); curvatures of link 1, 2 and 4 (b)

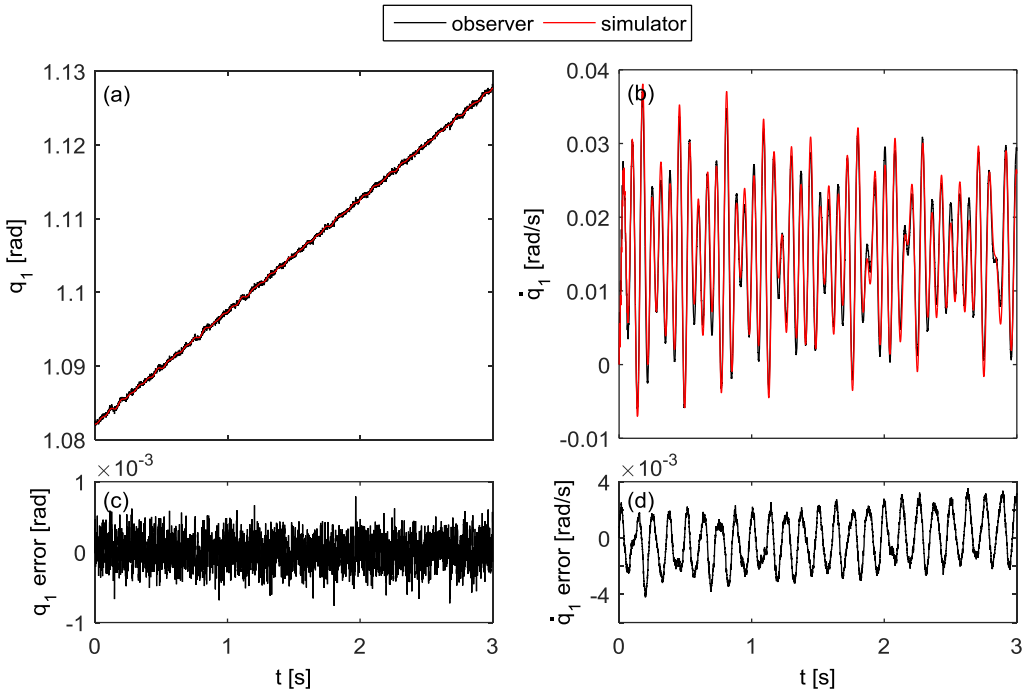


Figure 6.4: Estimated angular position (a) and velocity (b) of link 1. Position (c) and velocity (c) estimation error.

torques have been simulated to drive the actuated links:

$$\mathrm{T}_1 = 1.4\sin(2\pi 8t) \quad \mathrm{T}_2 = 7\sin(2\pi 10t) \quad \mathrm{T}_3 = 0.1\sin(2\pi 11t) \tag{6.7}$$

Gaussian noises have been added on all the three simulated torques with amplitudes of 0.20% of the full scale of, respectively, 15 Nm, 60 Nm, and 2 Nm torque meters. Successively, the signals have been digitized trough a 24-bit ADC with input range ± 10 V. Portions of the simulated input and output signals are shown, respectively, in Figs. 6.2 and 6.3.

The estimates of the angular positions and velocities of the three actuated links are plotted in Figs. 6.4-6.6. The same figures also show the time-histories of the error between the actual variables (computed through the full-order model and free measurement error signals) and the estimated ones. Error diagrams clearly show that the observer is able to deliver accurate estimates of the manipulator gross motion.

The observer capability of providing accurate estimates of the elastic state

variables is proved by Figs. 6.7-6.12. These figures refer to displacements and velocities of the master elastic dofs. Good agreement is confirmed to exist between the actual and the estimated variables, both in terms of amplitude and frequency content of the time-histories. In particular, further evidences of the observer effectiveness come from the fast Fourier transforms (FFT) of some of its estimates, which are shown in Fig. 6.13. Indeed, the FFTs of the estimated elastic displacement variables are almost perfectly overlapped to the actual ones. Such a result also confirms the capability of the reduced-order model to represent correctly the dynamics of the manipulator, since not only are the excitation frequencies (8, 10, 11 Hz) matched correctly, which is rather intuitive and simple to achieve, but also the exact amplitudes of the harmonic components at the system natural frequencies 14.2 Hz and 67.0 Hz.

Therefore, a very satisfactory agreement is proved to exist among both the estimated variables and the actual ones, as well as the reduced-order model and the full-order one.

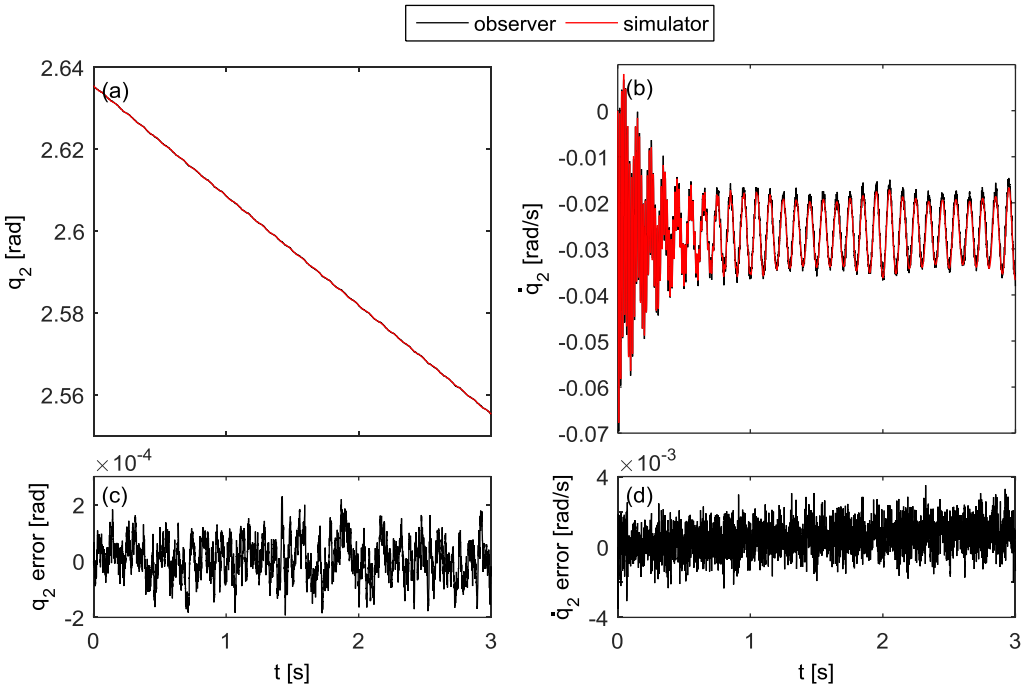


Figure 6.5: Estimated angular position (a) and velocity (b) of link 2. Position (c) and velocity (c) estimation error

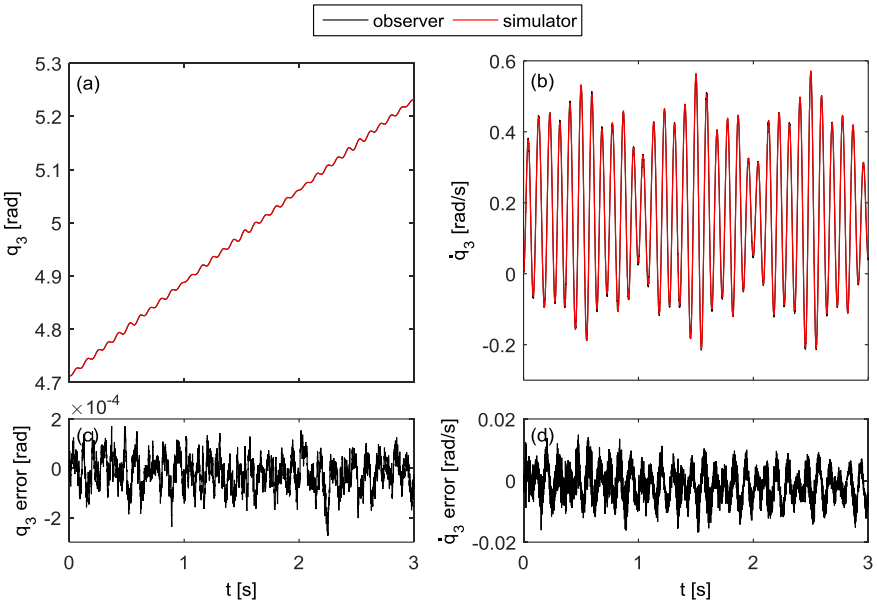


Figure 6.6: Estimated angular position (a) and velocity (b) of link 5. Position (c) and velocity (c) estimation error

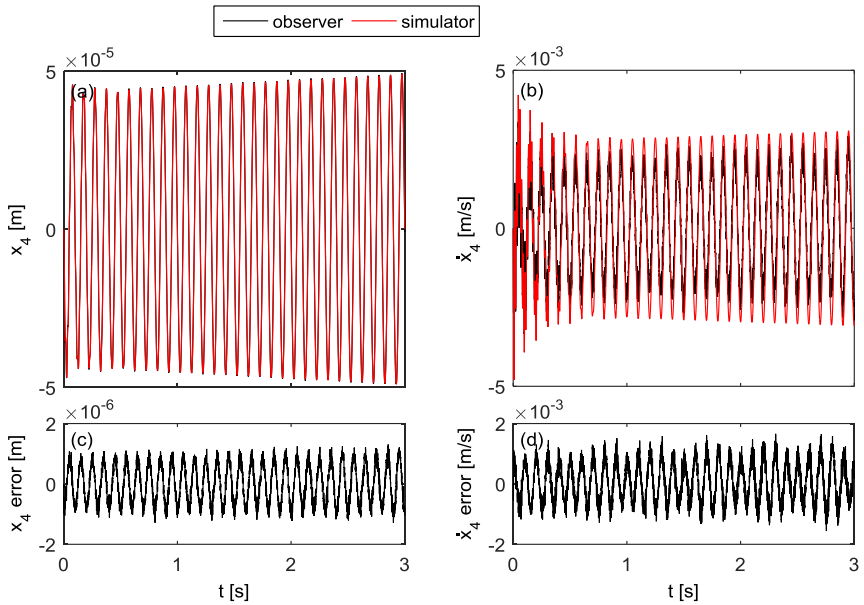


Figure 6.7: Estimated linear displacement (a) and velocity (b) of node 4 in x direction. Position (c) and velocity (c) estimation error

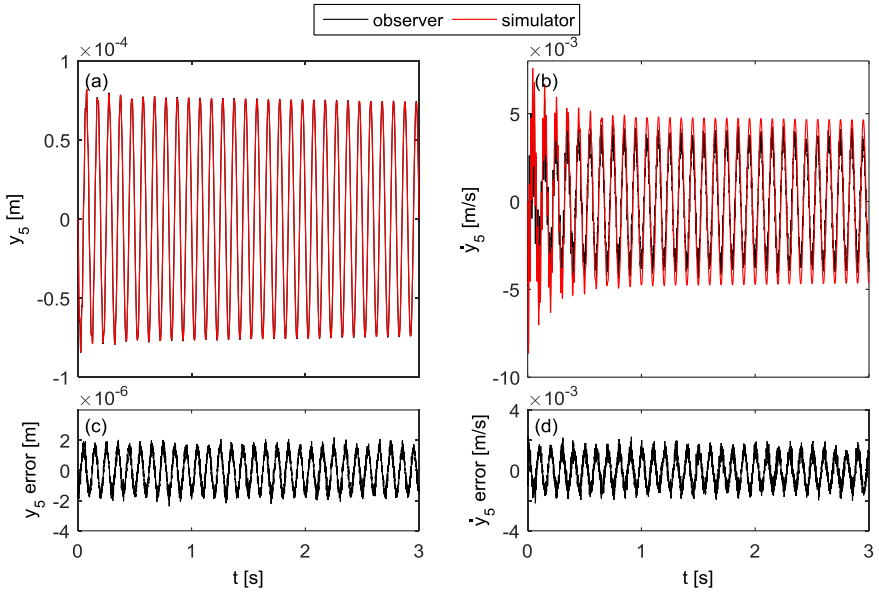


Figure 6.8: Estimated linear displacement (a) and velocity (b) of node 4 in y direction. Position (c) and velocity (c) estimation error

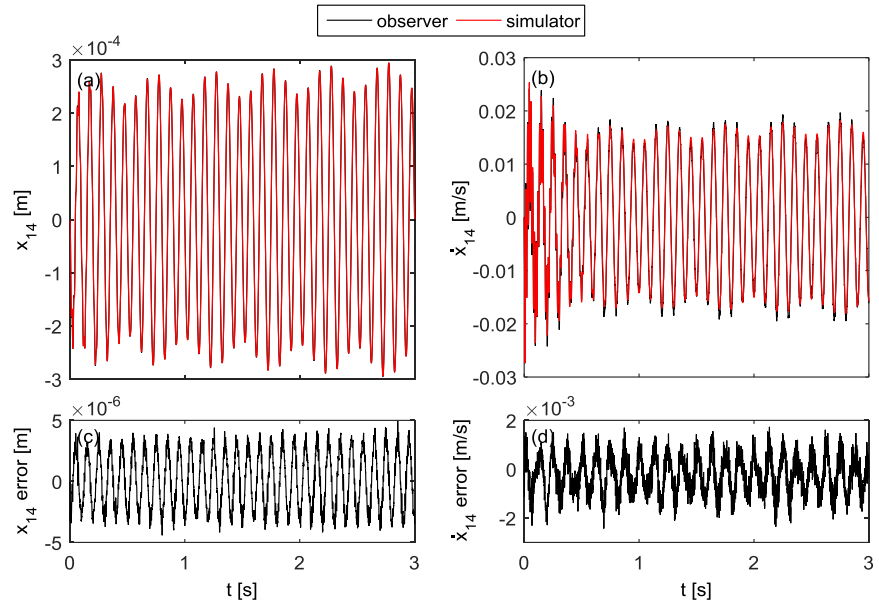


Figure 6.9: Estimated linear displacement (a) and velocity (b) of node 8 in x direction. Position (c) and velocity (c) estimation error

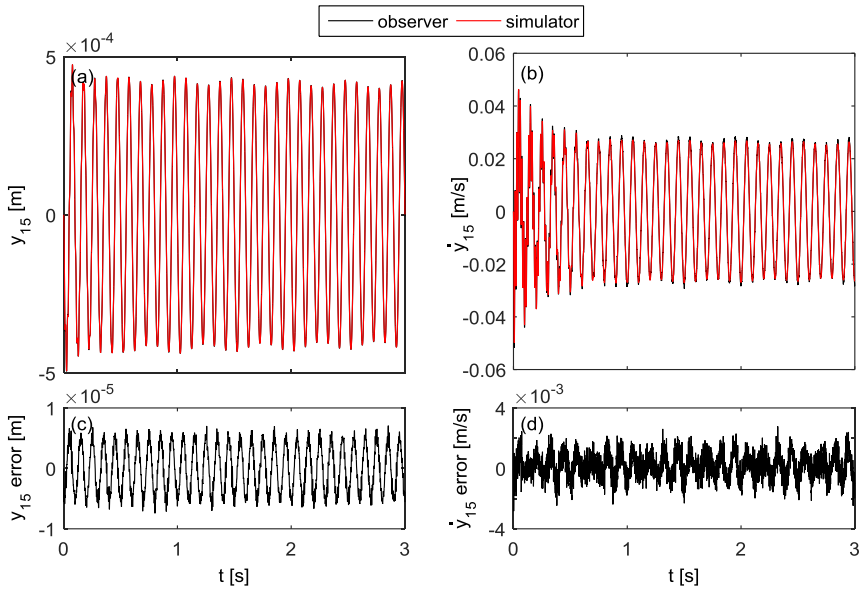


Figure 6.10: Estimated linear displacement (a) and velocity (b) of node 8 in y direction . Position (c) and velocity (c) estimation error

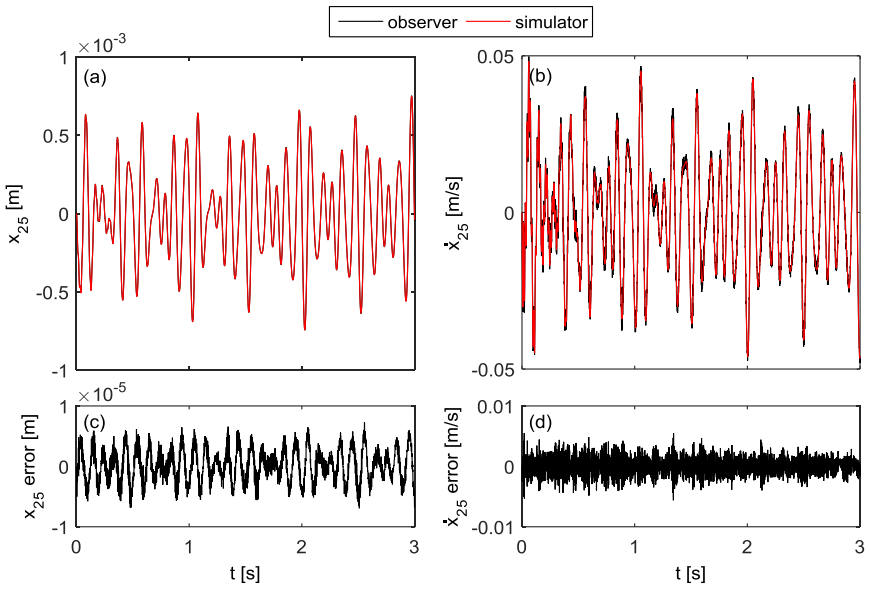


Figure 6.11: Estimated linear displacement (a) and velocity (b) of node 12 in x direction . Position (c) and velocity (c) estimation error

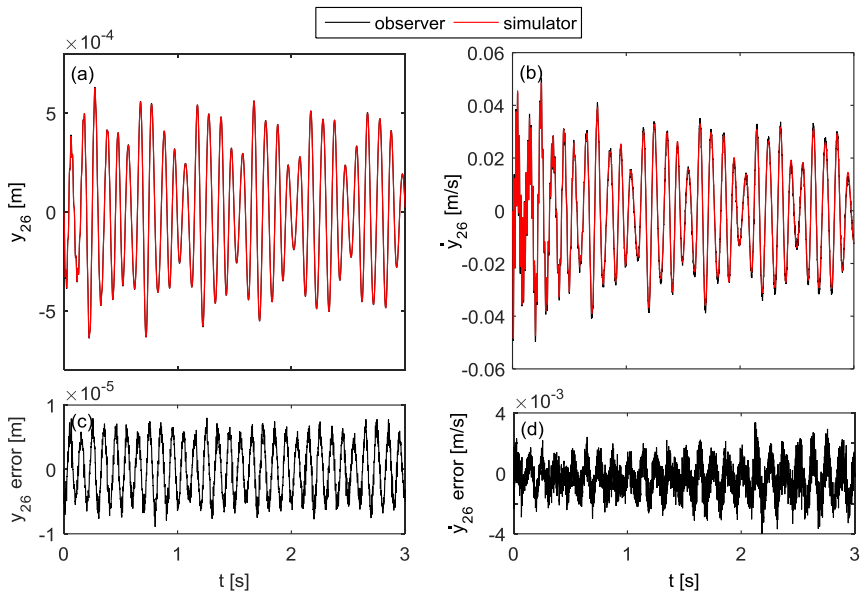


Figure 6.12: Estimated linear displacement (a) and velocity (b) of node 12 in y direction . Position (c) and velocity (c) estimation error

## 6.3 Computational complexity evaluation

This section does not claim to provide a complete analysis of the computational complexity of either of the estimation process or of the synthesis of reduced models, but rather it provides guidelines to evaluate the possible adoption of the reduction technique proposed in Chapter 5 in the state estimation in flexible-link MBSs.

Equation 6.3 clearly shows that to compute state prediction, i.e. the a-priori estimates of the state based on the model, some expensive matrix operations must be handled at any system configuration. Among these, the more expensive ones are the matrix multiplication and matrix inversion, which typically have $O(n^3)$ complexity, with $n$ matrix dimension.

It is indubitable that whenever it is possible to achieve an analytical formulation of the reduction matrix $\mathbf{H}$ (see Section 5.3), and hence of the reduced-order model, the use of such a model leads to several advantages from a computational view point. Indeed, whenever a full-order model is used, its first-order representation takes the same form shown in Eq. 6.3, hence the

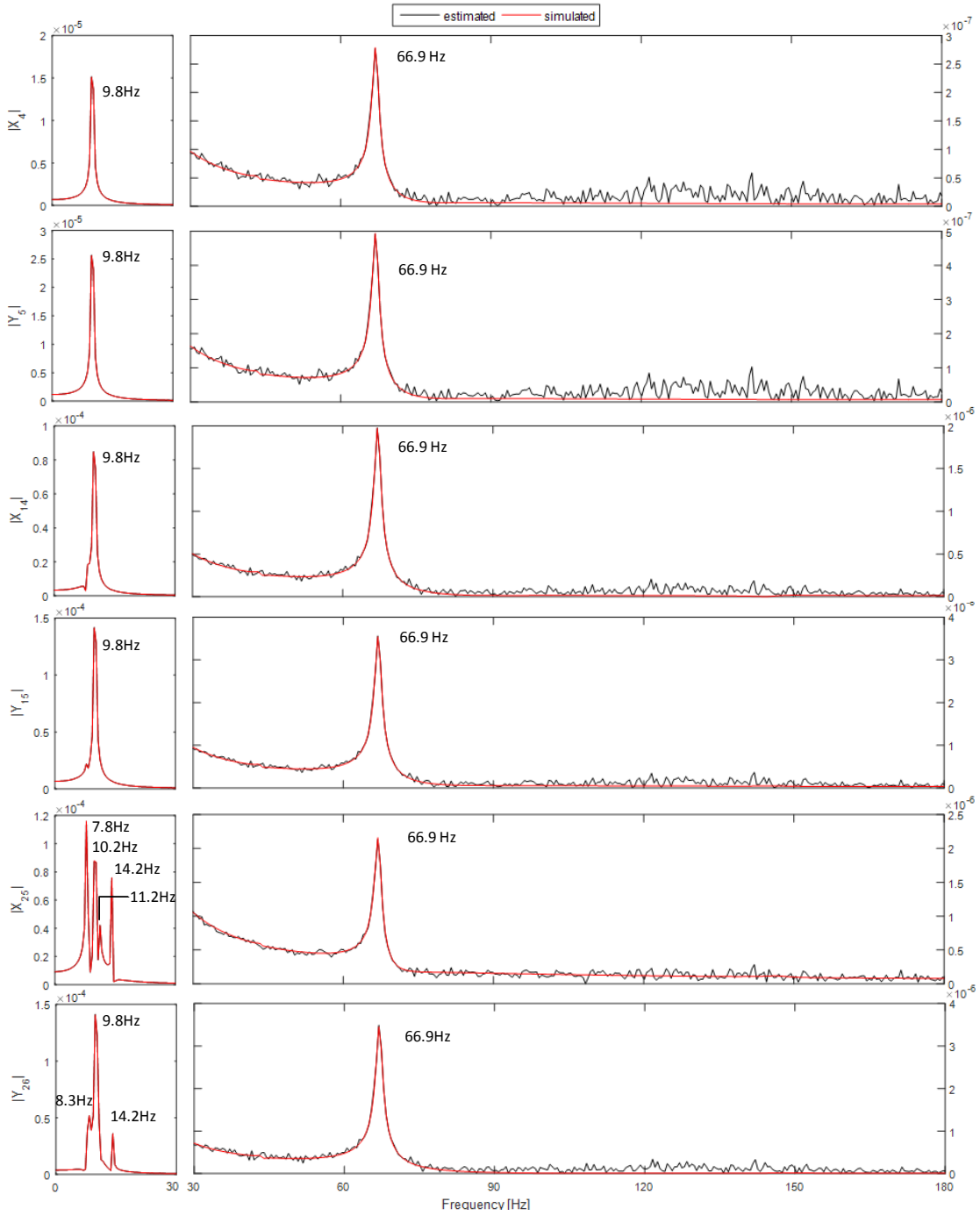


Figure 6.13: FFT of master elastic displacements

full-order model and the reduced one require the same number and kind of matrix operations, but are related to very different computational costs, being typically their dimensions very different.

Conversely, if the reduction matrix must be numerically computed it is not possible to a-priori assert the computational convenience of the reduced-order model proposed.

As discussed in Section 5.3, the critical issue for obtaining an analytical formulation of $\mathbf{H}$ relies in the computation of just a portion of the reduction matrix, i.e. the inverse of $\mathbf{K}_{ss}$. Therefore, it is possible and convenient to compute analytically in advance (pre-process) all the entries of the reduced model matrices, apart from the ones multiplied by $\mathbf{B}$:

$$\begin{aligned}
\widetilde{\mathbf{M}}(\mathbf{q}) &:= \begin{bmatrix} \left[\overline{\mathbf{M}}_{11} + \mathbf{B}^{\mathrm{T}}(\overline{\mathbf{M}}_{21} + \overline{\mathbf{M}}_{22}\mathbf{B}) + \overline{\mathbf{M}}_{12}\mathbf{B}\right](\mathbf{q}) & \widetilde{\mathbf{M}}_{12}(\mathbf{q}) \\ \widetilde{\mathbf{M}}_{21}(\mathbf{q}) & \widetilde{\mathbf{M}}_{22}(\mathbf{q}) \end{bmatrix} \\
\widetilde{\mathbf{C}}(\mathbf{q},\dot{\mathbf{q}}) &:= \begin{bmatrix} \left[\overline{\mathbf{C}}_{11} + \mathbf{B}^{\mathrm{T}}(\overline{\mathbf{C}}_{21} + \overline{\mathbf{C}}_{22}\mathbf{B}) + \overline{\mathbf{C}}_{12}\mathbf{B}\right](\mathbf{q},\dot{\mathbf{q}}) & \widetilde{\mathbf{C}}_{12}(\mathbf{q},\dot{\mathbf{q}}) \\ \widetilde{\mathbf{C}}_{21}(\mathbf{q},\dot{\mathbf{q}}) & \widetilde{\mathbf{C}}_{22}(\mathbf{q},\dot{\mathbf{q}}) \end{bmatrix} \\
\widetilde{\mathbf{K}}(\mathbf{q}) &:= \begin{bmatrix} \left[\overline{\mathbf{K}}_{11} + \overline{\mathbf{K}}_{12}\mathbf{B}\right](\mathbf{q}) & \widetilde{\mathbf{K}}_{12}(\mathbf{q}) \\ \widetilde{\mathbf{K}}_{21}(\mathbf{q}) & \widetilde{\mathbf{K}}_{22}(\mathbf{q}) \end{bmatrix} \\
\widetilde{\mathbf{L}}(\mathbf{q}) &:= \begin{bmatrix} \left[\overline{\mathbf{L}}_{11} + \mathbf{B}^{\mathrm{T}}\overline{\mathbf{L}}_{21}\right](\mathbf{q}) \\ \widetilde{\mathbf{L}}_{21}(\mathbf{q}) \end{bmatrix}
\end{aligned} \tag{6.8}$$

All the sub-matrices denoted by tilde have been defined in Eq. 6.4, and are explicit function of the actual configuration, all the other symbols make reference to the notation adopted in Section 5.3. In this case, the computation of the a priori estimates requires additional matrix operations.

An estimation of the computational cost can be made considering the complexity of the more expensive matrix operations (i.e. matrix multiplication and inversion). In particular, it will be consider that the multiplication of a matrix $n_1 \times n_2$ by a matrix $n_2 \times n_3$ has $O(n_1 \cdot n_2 \cdot n_3)$ complexity, and that the inversion of a matrix $n_1 \times n_1$ has $O(n_1^3)$ complexity.

Table 6.1 shows a list of all the matrix operations needed to compute state predictions by means of the reduced-order model. For each operation

the computational complexity has been indicated with reference to the dimension of the full order-model $n$, the number of master dofs $\mu$ and slave ones $s(s = n - \mu)$, and the number of retained interior modes $\tau$. An analogous list, referred to the full-order model, is shown in Tab. 6.2. By comparing the results stated in Tabs. 6.1 and 6.2 it is clear that as long as the following inequality holds true, a reduced-order model is more computationally efficient

Table 6.1: Computational complexity to compute state prediction by means of reduced-order model

| Operation | Dimension | Complexity |
|---|---|---|
| $\mathbf{K}_{22}^{-1}$ | $\mathbb{R}^{s\times s}$ | $s^3$ |
| $\mathbf{B} = \mathbf{K}_{22}^{-1}\mathbf{K}_{21}$ | | |
| $\overline{\mathbf{M}}_{22}\mathbf{B}$ | $\mathbb{R}^{s\times s} \times \mathbb{R}^{s\times\mu}$ | $3 \cdot (s^2\mu)$ |
| $\overline{\mathbf{C}}_{22}\mathbf{B}$ | | |
| $\mathbf{B}^{\mathrm{T}}(\overline{\mathbf{M}}_{21} + \overline{\mathbf{M}}_{22}\mathbf{B})$ | | |
| $\mathbf{B}^{\mathrm{T}}(\overline{\mathbf{C}}_{21} + \overline{\mathbf{C}}_{22}\mathbf{B})$ | | |
| $\overline{\mathbf{M}}_{12}\mathbf{B}$ | $\mathbb{R}^{\mu\times s} \times \mathbb{R}^{s\times\mu}$ | $5 \cdot (s\mu^2)$ |
| $\overline{\mathbf{C}}_{12}\mathbf{B}$ | | |
| $\mathbf{B}^{\mathrm{T}}\overline{\mathbf{L}}_{21}$ | | |
| $\widetilde{\mathbf{M}}^{-1}$ | | |
| $\widetilde{\mathbf{M}}^{-1}\widetilde{\mathbf{C}}$ | $\mathbb{R}^{(\mu+\tau)\times(\mu+\tau)}$ | $4 \cdot (\mu + \tau)^3$ |
| $\widetilde{\mathbf{M}}^{-1}\widetilde{\mathbf{K}}$ | | |
| $\widetilde{\mathbf{M}}^{-1}\widetilde{\mathbf{L}}$ | | |
| Complexity | $n^3 + 4(\mu + \tau)^3 + 2n\mu^2 - 3\mu^3$ | |

than the full-order one:

$$3n^3 > 4(\mu + \tau)^3 + 2n\mu^2 - 3\mu^3 \tag{6.9}$$

With reference to the test analyzed in this chapter, for which $n = 30$, $\mu = 9$, $s = 21$, and $\tau = 4$, the inequality in Eq. 6.9 holds true: $81,000 > 11,461$. This implies that the adoption of a reduced order model reduces the computation complexity by about 85%.

It is worth noticing that whenever Eq. 6.9 is false, it might be convenient the use of state observers based on reduced-models all the same. Indeed,

Table 6.2: Computational complexity to compute state prediction by means of full-order model

| Operation | Dimension | Complexity |
|---|---|---|
| $\overline{\mathbf{M}}^{-1}$ | | |
| $\overline{\mathbf{M}}^{-1}\overline{\mathbf{C}}$ | $\mathbb{R}^{n\times n}$ | $4\cdot n^3$ |
| $\overline{\mathbf{M}}^{-1}\overline{\mathbf{K}}$ | | |
| $\overline{\mathbf{M}}^{-1}\overline{\mathbf{L}}$ | | |
| Complexity | | $4n^3$ |

once the computation of $\mathbf{H}$ has been performed, the reduced model is much smaller than the full-order one, as a consequence all the operations required by the estimation algorithm (see for example Figs. 1.2 and 1.3) take shorter time. However, the complexity of such operations is strictly related to the chosen algorithm and its implementation, hence it is not possible to provide general guidelines, and an exhaustive analysis on computational complexity goes beyond the aims of this thesis.

## 6.4 Chapter summary

In this Chapter a state observer based on nonlinear reduced-order dynamic model for a representative flexible-link manipulator has been successfully synthesized. It has been proved that such an observer is able to deliver accurate estimates of both the rigid and elastic variables characterizing the motion of a rather complex flexible-link MBS. The test also confirmed reduced model capability to match correctly the MBS dynamics in a given frequency range.

# Chapter 7

# Conclusions

This thesis has been focused on state estimation in multibody systems (MBSs) with either rigid or flexible links. Its main aim has been to synthesize state observers with improved accuracy and efficiency. To this end the main aspects concerning estimation have been addressed, namely the investigation of estimation algorithms able to cope with model nonlinearities and the development of MB models suitable to state estimation, i.e. accurate and computationally efficient.

In order to obtained the best results, it has been necessary to develop different approaches for rigid-link and flexible-link MBSs.

In the case of rigid-link MBSs, two preliminary considerations have driven the development of the estimation strategy: the state of a MBS just includes kinematic variables; and it is well-known that, kinematic constraint equations can be easily written and solved irrespective of the forces that produce the motion under the assumptions that the links are rigid and joint clearance is negligible. As a consequence, a new approach has been presented for the design of nonlinear state observers for MBSs, which is based on kinematic constraint equations. The approach is general, in the sense that it can be applied to both open-chain and closed-chain MBSs complying with the assumptions that links are rigid and clearance in joint is negligible. Basically, the new approach is based on estimating the kinematic state variables exploiting kinematic constraint equations and the measurements of kinematic quantities (e.g. positions and accelerations), additionally, it copes with the nonlinearities of kinematic models through the use of nonlinear state ob-

servers, belonging to the family of sigma point Kalman filters.

The use of filters based on kinematic constraint equations is advantageous since such equations are much less affected by uncertainty (they depend on just geometric parameters) than the dynamic equations of motion, usually employed in state observers. Therefore the impact of model uncertainty in the estimation accuracy is drastically reduced.

The choice of performing kinematic estimation has implied developing state-space first-order formulation of the kinematic constraint equations in both continuous-time and discrete-time, and providing a suitable definition of system inputs and outputs. Additionally, issues like state derivative estimation with discrete-time schemes and the estimation in model singularity have been tacked and overcome.

The soundness of the proposed theory has been proved through numerical and experimental tests on both open-chain and closed-chain MBSs, with very satisfactory results.

In this thesis it is also proved that, though kinematics-based observers do not require force and torque measurements (often difficult to gather) as inputs, they can be successfully employed for estimating unknown forces. In particular, a novel approach, named two-stage approach, has been finalized to address the so-called problem of "unknown inputs", i.e. the concurrent estimation of both the kinematic state and the unknown forces acting on a system. Terms "unknown inputs" make implicit reference to the use of dynamic models in state estimations: the standard Kalman filter-based approaches require that all the forces acting on the system are known and used as inputs to dynamic models. But in conditions of "unknown inputs" the traditional approaches are no longer useful. In order to estimate such inputs, the state is typically augmented with the unknown forces, modeled through random walk models (i.e. through a constant value plus white noise). Nevertheless adopting a random walk model, which is an approximate model, may negatively affect the estimation of the kinematic state variables.

By taking advantage of the independence of kinematics from dynamics in rigid-link MBSs, a "two-stage" approach has been proposed, which allows estimating the unknown forces and the kinematic state separately. The estimation process is split into two estimations running concurrently, and car-

ried out by, respectively a first kinematic observer estimating the kinematic state regardless of the unknown forces, and a second observer estimating the unknown forces using as inputs the kinematic estimates. This approach, together with the use of innovative nonlinear observers, allowed obtaining accurate estimates of the state by decoupling the estimation of the kinematic variables from that of the dynamic variables.

The approach has been validated successfully, by applying it to the estimation of the force acting on the slider of a slider-crank mechanism and the estimation of the contact force between the ground and the bucket of an excavator. The comparison between the results obtained with the two-stage approach and the traditional one corroborates all the theoretical considerations, and highlights that more accurate estimates of both the state and the unknown input forces can be obtained through the two-stage approach.

The synthesis of state observers for flexible-link MBSs required a rather different approach reflecting two peculiarities of flexible-link MBSs. Firstly, the total motion of such systems is typically modeled as the superposition of a large amplitude rigid-body motion and a small-amplitude elastic deformation, mutually influenced. Since it is not possible to decouple the elastic displacements from the forces that have generated them, it is not possible to adopt a kinematic approach for estimating state variables in MBSs with flexible-links (although the state comprises just kinematic variables). Additionally, an accurate representation of the fine motion requires to employ several elastic coordinates, which lead to high dimension models, which, in turns, are not suitable to synthesize efficient state observers.

Therefore, a considerable effort has been devoted to the development of effective model reduction strategies which allow keeping to a minimum the size of the nonlinear dynamic model of a flexible-link MBS, in order to use them in the synthesis of more efficient state observers.

By initially referring to linear systems, a reduction strategy has been developed. It consists in using of the CB method together with new ranking methods suitably developed to meet specific design requirements in the use of reduced models. Indeed, reduced model capability to represent correctly the dynamics of interest of a mechanical system is strictly related to the selection of the interior modes of the CB method to be retained. Two ranking

method have been developed: the interior mode ranking (IMR) and the energy-based ranking (EBR). They allow ranking and selecting the interior vibrational modes of the Craig-Bampton method that guarantee obtaining an accurate and minimum-size reduced model. In particular, the IMR ensures that reduced models accurately describe the dynamics of the system at a specific frequency or in a frequency range of interest. The EBR method instead ensures that reduced models correctly represent the forced response of a system to periodic inputs. Both the methods provide a ranking of the interior vibrational modes on the basis of analytically defined coefficients, describing the relation between each interior mode and either the frequencies and shapes of the vibration modes of interest, in the case of IMR, or the forced response, in case of EBR. The application of the proposed ranking methods to different mechanical structures and the comparison with other ranking techniques available in literature have allowed verifying their effectiveness, also experimentally.

Subsequently, the proposed reduction strategy had been extended to flexible-link MB models. In particular, it allows performing the reduction at system level of dynamic models based on the equivalent rigid link system (ERLS). The new strategy leads to the formulation of a configuration-dependent reduction transformation capable of representing the nonlinearities of the full-order model, and its dependence on configuration.

The proposed strategy has been validated by applying it to the reduction of the model of a planar manipulator with flexible links and driven by three motors. Once again, the results obtained are fully satisfactory, since it was possible to demonstrate that the developed technique, in the case taken into consideration, leads to a significant reduction in the size of the models and an appropriate representation of the system dynamics.

Finally, the research activity has been completed by the implementation of state observers for nonlinear flexible-link MBSs, based on reduced-order dynamic models. Such observers proved to be very effective though prone to improvement in terms of computational efficiency, which, however, is beyond the scope of the research.

# References


[1] R. Caracciolo, D. Richiedei, and A. Trevisani, "Robust piecewise-linear state observers for flexible link mechanisms," *Journal of Dynamic Systems, Measurement, and Control*, vol. 130, no. 3, p. 031011, 2008.

[2] X. Wei, H. Liu, and L. Jia, "Fault detection of urban rail vehicle suspension system based on acceleration measurements," in *Advanced Intelligent Mechatronics (AIM), 2012 IEEE/ASME International Conference on*, pp. 1129–1134, IEEE, 2012.

[3] M. Jesussek and K. Ellermann, "Fault detection and isolation for a railway vehicle by evaluating estimation residuals," *Procedia IUTAM*, vol. 13, pp. 14–23, 2015.

[4] T. Wenzel, K. Burnham, M. Blundell, and R. Williams, "Kalman filter as a virtual sensor: applied to automotive stability systems," *Transactions of the Institute of Measurement and Control*, vol. 29, no. 2, pp. 95–115, 2007.

[5] M. C. Best, A. P. Newton, and S. Tuplin, "The identifying extended kalman filter: parametric system identification of a vehicle handling model," *Proceedings of the Institution of Mechanical Engineers, Part K: Journal of Multi-body Dynamics*, vol. 221, no. 1, pp. 87–98, 2007.

[6] E. D. Blanchard, A. Sandu, and C. Sandu, "Parameter estimation method using an extended kalman filter," in *Proceedings of the Joint North America, Asia-Pacific ISTVS Conference and Annual Meeting of Japanese Society for Terramechanics.*

[7] O. A. Bauchau and J. Wang, "Stability evaluation and system identification of flexible multibody systems," *Multibody System Dynamics*, vol. 18, no. 1, pp. 95–106, 2007.

[8] R. E. Kalman, "A new approach to linear filtering and prediction problems," *Journal of Fluids Engineering*, vol. 82, no. 1, pp. 35–45, 1960.

[9] A. J. Haug, *Bayesian Estimation and Tracking: A Practical Guide.* John Wiley & Sons, 2012.

[10] S. F. Schmidt, "Applications of state space methods to navigation problems," *Advances in Control Systems*, vol. 3, pp. 293–340, 1966.

[11] M. S. Grewal and A. P. Andrews, *Kalman filtering: Theory and Practice with MATLAB.* John Wiley & Sons, 2014.

[12] D. Simon, *Optimal state estimation: Kalman, H infinity, and nonlinear approaches.* John Wiley & Sons, 2006.

[13] R. Pastorino, D. Richiedei, J. Cuadrado, and A. Trevisani, "State estimation using multibody models and non-linear kalman filters," *International Journal of Non-Linear Mechanics*, vol. 53, pp. 83–90, 2013.

[14] J. Cuadrado, D. Dopico, A. Barreiro, and E. Delgado, "Real-time state observers based on multibody models and the extended kalman filter," *Journal of mechanical science and technology*, vol. 23, no. 4, pp. 894–900, 2009.

[15] J. Cuadrado, D. Dopico, J. A. Perez, and R. Pastorino, "Automotive observers based on multibody models and the extended kalman filter," *Multibody System Dynamics*, vol. 27, no. 1, pp. 3–19, 2012.

[16] R. Dhaouadi, N. Mohan, and L. Norum, "Design and implementation of an extended kalman filter for the state estimation of a permanent magnet synchronous motor," *Power Electronics, IEEE Transactions on*, vol. 6, no. 3, pp. 491–497, 1991.

[17] Y. Wang and M. Papageorgiou, "Real-time freeway traffic state estimation based on extended kalman filter: a general approach," *Transportation Research Part B: Methodological*, vol. 39, no. 2, pp. 141–167, 2005.

[18] M. Hoshiya and E. Saito, "Structural identification by extended kalman filter," *Journal of Engineering Mechanics*, vol. 110, no. 12, pp. 1757–1770, 1984.

[19] T. A. Wenzel, K. Burnham, M. Blundell, and R. Williams, "Dual extended kalman filter for vehicle state and parameter estimation," *Vehicle System Dynamics*, vol. 44, no. 2, pp. 153–171, 2006.

[20] K. Ito and K. Xiong, "Gaussian filters for nonlinear filtering problems," *Automatic Control, IEEE Transactions on*, vol. 45, no. 5, pp. 910–927, 2000.

[21] M. NøRgaard, N. K. Poulsen, and O. Ravn, "New developments in state estimation for nonlinear systems," *Automatica*, vol. 36, no. 11, pp. 1627–1638, 2000.

[22] S. J. Julier, J. K. Uhlmann, and H. F. Durrant-Whyte, "A new approach for filtering nonlinear systems," in *American Control Conference, Proceedings of the 1995*, vol. 3, pp. 1628–1632, IEEE, 1995.

[23] S. J. Julier and J. K. Uhlmann, "New extension of the kalman filter to nonlinear systems," in *AeroSense'97*, pp. 182–193, International Society for Optics and Photonics, 1997.

[24] S. J. Julier, "Skewed approach to filtering," in *Aerospace/Defense Sensing and Controls*, pp. 271–282, International Society for Optics and Photonics, 1998.

[25] S. J. Julier, "The scaled unscented transformation," in *American Control Conference, 2002. Proceedings of the 2002*, vol. 6, pp. 4555–4559, IEEE, 2002.

[26] S. J. Julier and J. K. Uhlmann, "Reduced sigma point filters for the propagation of means and covariances through nonlinear transformations," in *American Control Conference, 2002. Proceedings of the 2002*, vol. 2, pp. 887–892, IEEE, 2002.

[27] S. J. Julier, "The spherical simplex unscented transformation," in *American Control Conference, 2003. Proceedings of the 2003*, vol. 3, pp. 2430–2434, IEEE, 2003.

[28] R. Van Der Merwe, E. A. Wan, S. Julier, *et al.*, "Sigma-point kalman filters for nonlinear estimation and sensor-fusion: Applications to integrated navigation," in *Proceedings of the AIAA Guidance, Navigation & Control Conference*, pp. 16–19, 2004.

[29] R. Van Der Merwe, E. A. Wan, S. Julier, *et al.*, "Sigma-point kalman filters for nonlinear estimation and sensor-fusion: Applications to integrated navigation," in *Proceedings of the AIAA Guidance, Navigation & Control Conference*, pp. 16–19, 2004.

[30] R. Van Der Merwe and E. A. Wan, "Efficient derivative-free kalman filters for online learning.," in *ESANN*, pp. 205–210, Citeseer, 2001.

[31] R. Van Der Merwe, E. Wan, *et al.*, "The square-root unscented kalman filter for state and parameter-estimation," in *Acoustics, Speech, and Signal Processing, 2001. Proceedings.(ICASSP'01). 2001 IEEE International Conference on*, vol. 6, pp. 3461–3464, IEEE, 2001.

[32] M. Saura, J. Cuadrado, D. Dopico, and A. I. Celdran, "Computational kinematics of multibody systems: The advantages of a topological method based on its kinematic structure," *Proceedings of ECCOMAS Multibody Dynamics*, pp. 1–4, 2013.

[33] S. Jeon, M. Tomizuka, and T. Katou, "Kinematic kalman filter (kkf) for robot end-effector sensing," *Journal of dynamic systems, measurement, and control*, vol. 131, no. 2, p. 021010, 2009.

[34] S. Jeon, "State estimation based on kinematic models considering characteristics of sensors," in *American Control Conference (ACC), 2010*, pp. 640–645, IEEE, 2010.

[35] C. Wang, W. Chen, and M. Tomizuka, "Robot end-effector sensing with position sensitive detector and inertial sensors," in *Robotics and Automation (ICRA), 2012 IEEE International Conference on*, pp. 5252–5257, IEEE, 2012.

[36] J. Žumer, J. Slavič, and M. Boltežar, "Minimization of the positional errors for an accurate determination of the kinematic parameters of a rigid-body system with miniature inertial sensors," *Mechanism and Machine Theory*, vol. 81, pp. 193–208, 2014.

[37] R. Hermann and A. J. Krener, "Nonlinear controllability and observability," *IEEE Transactions on automatic control*, vol. 22, no. 5, pp. 728–740, 1977.

[38] K. Reif, S. Günther, E. Yaz, and R. Unbehauen, "Stochastic stability of the discrete-time extended kalman filter," *IEEE Transactions on Automatic Control*, vol. 44, no. 4, pp. 714–728, 1999.

[39] J. G. De Jalon and E. Bayo, *Kinematic and dynamic simulation of multibody systems: the real-time challenge*. Springer Science & Business Media, 2012.

[40] D. Richiedei and A. Trevisani, "Vibration confinement in lightly damped multibody systems: An hybrid active-passive approach.," in *Thematic Conference on Multibody Dynamics,ECCOMAS 2013*, 2013.

[41] C. Lanczos, *Applied analysis*. Courier Corporation, 1988.

[42] I. Palomba, D. Richiedei, and A. Trevisani, "Nonlinear kinematic state estimation in rigid-link multibody systems by spherical simplex sigma point unscented kalman filters," in *Proceedings of ISMA 2014 - International Conference on Noise and Vibration Engineering and USD 2014 - International Conference on Uncertainty in Structural Dynamics*, pp. 2899–2914, 2014.

[43] E. Lourens, C. Papadimitriou, S. Gillijns, E. Reynders, G. De Roeck, and G. Lombaert, "Joint input-response estimation for structural systems based on reduced-order models and vibration data from a limited number of sensors," *Mechanical Systems and Signal Processing*, vol. 29, pp. 310–327, 2012.

[44] F. Naets, R. Pastorino, J. Cuadrado, and W. Desmet, "Online state and input force estimation for multibody models employing extended kalman filtering," *Multibody System Dynamics*, vol. 32, no. 3, pp. 317–336, 2014.

[45] I. Palomba, D. Richiedei, and A. Trevisani, "Simultaneous estimation of kinematic state and unknown input forces in rigid-link multibody systems," in *ECCOMAS Thematic Conference on Multibody Dynamics 2015*, pp. 229–240, June 29 – July 2, Barcelona, Spain 2015.

[46] A. Radke and Z. Gao, "A survey of state and disturbance observers for practitioners," in *American Control Conference, 2006*, pp. 6–pp, IEEE, 2006.

[47] E. Lourens, E. Reynders, G. De Roeck, G. Degrande, and G. Lombaert, "An augmented kalman filter for force identification in structural dynamics," *Mechanical Systems and Signal Processing*, vol. 27, pp. 446–460, 2012.

[48] M. González, A. Luaces, D. Dopico, and J. Cuadrado, "A 3d physics-based hydraulic excavator simulator," in *ASME-AFM 2009 world conference on innovative virtual reality*, pp. 75–80, 2009.

[49] S. K. Dwivedy and P. Eberhard, "Dynamic analysis of flexible manipulators, a literature review," *Mechanism and machine theory*, vol. 41, no. 7, pp. 749–777, 2006.

[50] A. A. Shabana, "Flexible multibody dynamics: review of past and recent developments," *Multibody system dynamics*, vol. 1, no. 2, pp. 189–222, 1997.

[51] G. Lowen and W. Jandrasits, "Survey of investigations into the dynamic behavior of mechanisms containing links with distributed mass and elasticity," *Mechanism and Machine theory*, vol. 7, no. 1, pp. 3–17, 1972.

[52] A. Erdman and G. Sandor, "Kineto–elastodynamics —a review of the state of the art and trends," *Mechanism and Machine Theory*, vol. 7, no. 1, pp. 19–33, 1972.

[53] G. Lowen and C. Chassapis, "The elastic behavior of linkages: An update," *Mechanism and Machine Theory*, vol. 21, no. 1, pp. 33–42, 1986.

[54] W. J. Book, "Modeling design, and control of flexible manipulator arms: A tutorial review," in *Proceedings of the 29th IEEE Conference on Decision and Control, Honolulu, Hawaii*, pp. 500–506, 1990.

[55] G. Zhu, S. S. Ge, and T. H. Lee, "Simulation studies of tip tracking control of a single-link flexible robot based on a lumped model," *Robotica*, vol. 17, no. 01, pp. 71–78, 1999.

[56] W. Khalil and M. Gautier, "Modeling of mechanical systems with lumped elasticity," in *Robotics and Automation, 2000. Proceedings. ICRA'00. IEEE International Conference on*, vol. 4, pp. 3964–3969, IEEE, 2000.

[57] R. H. Cannon and E. Schmitz, "Initial experiments on the end-point control of a flexible one-link robot," *The International Journal of Robotics Research*, vol. 3, no. 3, pp. 62–75, 1984.

[58] Y. Sakawa, F. Matsuno, and S. Fukushima, "Modeling and feedback control of a flexible arm," *Journal of Robotic Systems*, vol. 2, no. 4, pp. 453–472, 1985.

[59] R. J. Theodore and A. Ghosal, "Comparison of the assumed modes and finite element models for flexible multilink manipulators," *The International journal of robotics research*, vol. 14, no. 2, pp. 91–111, 1995.

[60] S. S. Ge, T. H. Lee, and G. Zhu, "A nonlinear feedback controller for a single-link flexible manipulator based on a finite element model," *Journal of Robotic Systems*, vol. 14, no. 3, pp. 165–178, 1997.

[61] P. Kalra and A. M. Sharan, "Accurate modelling of flexible manipulators using finite element analysis," *Mechanism and Machine Theory*, vol. 26, no. 3, pp. 299–313, 1991.

[62] S. Nagarajan and D. A. Turcic, "Lagrangian formulation of the equations of motion for elastic mechanisms with mutual dependence between rigid body and elastic motions. part i: element level equations," *Journal of Dynamic Systems, Measurement, and Control*, vol. 112, no. 2, pp. 203–214, 1990.

[63] S. Nagarajan and D. A. Turcic, "Lagrangian formulation of the equations of motion for elastic mechanisms with mutual dependence between rigid body and elastic motions. part ii: systems equations," *Journal of Dynamic Systems, Measurement, and Control*, vol. 112, no. 2, pp. 215–224, 1990.

[64] A. A. Shabana, *Dynamics of multibody systems*. Cambridge university press, 2013.

[65] M. Giovagnoni, "A numerical and experimental analysis of a chain of flexible bodies," *Journal of dynamic systems, measurement, and control*, vol. 116, no. 1, pp. 73–80, 1994.

[66] V. Renato, G. Alessandro, and G. Marco, "A method for modeling of three-dimensional flexible mechanisms based on an equivalent rigid-link system," *Journal of Vibration and Control*, p. 1077546312463745, 2012.

[67] R. Vidoni, A. Gasparetto, and M. Giovagnoni, "Design and implementation of an erls-based 3-d dynamic formulation for flexible-link robots," *Robotics and Computer-Integrated Manufacturing*, vol. 29, no. 2, pp. 273–282, 2013.

[68] L.-W. Chang and J. Hamilton, "The kinematics of robotic manipulators with flexible links using an equivalent rigid link system (erls) model," *Journal of dynamic systems, measurement, and control*, vol. 113, no. 1, pp. 48–53, 1991.

[69] D. A. Turcic, A. Midha, and J. Bosnik, "Dynamic analysis of elastic mechanism systems. part ii: Experimental results," *Journal of Dynamic Systems, Measurement, and Control*, vol. 106, no. 4, pp. 255–260, 1984.

[70] J. Mottershead and M. Friswell, "Model updating in structural dynamics: a survey," *Journal of sound and vibration*, vol. 167, no. 2, pp. 347–375, 1993.

[71] S. Sehgal and H. Kumar, "Structural dynamic model updating techniques: A state of the art review," *Archives of Computational Methods in Engineering*, pp. 1–19.

[72] G.-H. Kim and Y.-S. Park, "An improved updating parameter selection method and finite element model update using multiobjective optimisation technique," *Mechanical Systems and Signal Processing*, vol. 18, no. 1, pp. 59–78, 2004.

[73] S. Weng, Y. Xia, Y.-L. Xu, and H.-P. Zhu, "Substructure based approach to finite element model updating," *Computers & Structures*, vol. 89, no. 9, pp. 772–782, 2011.

[74] H. Ahmadian, J. Mottershead, and M. Friswell, "Regularisation methods for finite element model updating," *Mechanical Systems and Signal Processing*, vol. 12, no. 1, pp. 47–64, 1998.

[75] K. Ordaz-Hernandez and X. Fischer, "Fast reduced model of non-linear dynamic euler-bernoulli beam behaviour," *Int. J. Mech. Sci.*, vol. 50, no. 8, pp. 1237 – 1246, 2008.

[76] R. Vidoni, A. Gasparetto, and M. Giovagnoni, "Design and implementation of an ERLS-based 3-D dynamic formulation for flexible-link robots," *Robot. Cim-Int. Manuf.*, vol. 29, pp. 273 – 282, 2013.

[77] D. Richiedei, A. Trevisani, and G. Zanardo, "A constrained convex approach to modal design optimization of vibrating system," *J. Mech. Des-T. ASME*, vol. 133, no. 6, pp. 061011–1/9, 2011.

[78] H. Ouyang, D. Richiedei, A. Trevisani, and G. Zanardo, "Discrete mass and stiffness modifications for the inverse eigenstructure assignment in vibrating systems: Theory and experimental validation," *Int. J. Mech. Sci*, vol. 64, no. 1, pp. 211–220, 2012.

[79] T. Pumhössel and P. Hehenberger, "Model reduction of a parametrically excited drivetrain," in *Proc. ASME Design Engineering Technical Conference 1*, (Chicago, USA), August 2012.

[80] T. Pumhössel, P. Hehenberger, and S. Boschert, "On the advantages of using reduced system models in the model-based development of

mechatronic systems," in *Proc. of 2nd Workshop on Mechatronic Design, Paris, France*, 11 2013.

[81] R. Caracciolo, D. Richiedei, and A. Trevisani, "Design and experimental validation of piecewise-linear state observers for flexible link mechanisms," *Meccanica*, vol. 41, no. 6, pp. 623 – 637, 2006.

[82] A. Gasparetto and S. Miani, "Dynamic model of a rotating channel used in the steel industry and implementation of a controller," *JVC/Journal of Vibration and Control*, vol. 10, no. 3, pp. 423–445, 2004.

[83] F. Naets, R. Pastorino, J. Cuadrado, and W. Desmet, "Use of subsystem global modal parameterization models in extended kalman filtering for online coupled state/force," in *Proceeding of ECCOMAS Multibody Dynamics*, (University of Zagreb, Croatia), July 2013.

[84] C. Renzi, C. Pezerat, and J. Guyader, "Identification of vibration excitation using a regularized finite element operator and a deconvolution post-process," in *Proc. Acoustics*, (Nantes, France), April 2012.

[85] E. L. Blades, "A craig-bampton test-analysis model," in *Proceedings-SPIE the International Society for Optical Engineering*, pp. 1386–1391, SPIE the International Society for Optical Engineering, 1997.

[86] G. V. Des Roches, J.-P. Bianchi, E. Balmes, R. Lemaire, and T. Pasquet, "Using component modes in a system design process," in *Structural Dynamics, Volume 3*, pp. 617–625, Springer, 2011.

[87] B. Besselink, U. Tabak, A. Lutowska, N. van de Wouw, H. Nijmeijer, D. Rixen, M. Hochstenbach, and W. Schilders, "A comparison of model reduction techniques from structural dynamics, numerical mathematics and systems and control," *Journal of Sound and Vibration*, vol. 332, no. 19, pp. 4403–4422, 2013.

[88] B. Zhaojun, "Krylov subspace techniques for reduced-order modelling of large-scale dynamical systems," *Appl. Numer. Math.*, vol. 43, no. 1-2, pp. 9–44, 2002.

[89] S. Guercin and A. Antolaus, "A survey of model reduction by balanced truncation and some new results,"

[90] R. Craig and M. Bampton, "Coupling of substructures for dynamic analyses," *AIAA Journal*, vol. 6, no. 7, pp. 1313–1319, 1968.

[91] F. Matichard and L. Gaudiller, "Hybrid modal nodal method for multibody smart structure model reduction: application to modal feedback control," *Smart materials and structures*, vol. 15, no. 6, p. 1887, 2006.

[92] N. Zhang, "Dynamic condensation of mass and stiffness matrices," *J. Sound Vib.*, vol. 188, no. 4, pp. 601–615, 1995.

[93] M. Friswell, "The convergence of the iterated IRS method," *J. Sound Vib.*, vol. 211, no. 1, pp. 123–132, 1998.

[94] J. Guyan, "Reduction of stiffness and mass matrices," *AIAA Journal*, vol. 3, no. 2, pp. 380–380, 1965.

[95] C. Christopher, "Model reduction using Guyan, IRS and dynamic methods," in *Proc. IMAC XVI*, (Santa Barbara, USA), February 1998.

[96] W. Hurty, "Dynamic analysis of structural systems using component modes," *AIAA Journal*, vol. 3, no. 4, pp. 678–685, 1965.

[97] R. Goldman, L. Chen, and H. Sheu, "Vibration analysis by dynamic partitioning," *AIAA Journal*, vol. 7, no. 6, pp. 1152–1154, 1969.

[98] R. MacNeal, "A hybrid method of component mode synthesis," *Comput. Struct.*, vol. 1, no. 4, pp. 581–601, 1971.

[99] D. Rixen, "A dual Craig-Bampton method for dynamic substructuring," *J. Comput. Appl. Math.*, vol. 168, no. 1-2, pp. 383–391, 2004.

[100] S. Rubin, "Improved component-mode representation for structural dynamic analysis," *AIAA Journal*, vol. 13, no. 8, pp. 995–1006, 1975.

[101] W. Benfield and R. Hruda, "Vibration analysis of structures by component mode substitution," *AIAA Journal*, vol. 9, no. 7, pp. 1255–1261, 1971.

[102] A. A. Shabana and R. A. Wehage, "A coordinate reduction technique for dynamic analysis of spatial substructures with large angular rotations," *Journal of Structural Mechanics*, vol. 11, no. 3, pp. 401–431, 1983.

[103] O. A. Bauchau and J. Rodriguez, "Formulation of modal-based elements in nonlinear, flexible multibody dynamics," *International Journal for Multiscale Computational Engineering*, vol. 1, no. 2&3, 2003.

[104] M. Lehner and P. Eberhard, "On the use of moment-matching to build reduced order models in flexible multibody dynamics," *Multibody System Dynamics*, vol. 16, no. 2, pp. 191–211, 2006.

[105] A. Cardona, "Superelements modelling in flexible multibody dynamics," *Multibody System Dynamics*, vol. 4, no. 2-3, pp. 245–266, 2000.

[106] R. Vidoni, P. Gallina, P. Boscariol, A. Gasparetto, and M. Giovagnoni, "Modeling the vibration of spatial flexible mechanisms through an equivalent rigid-link system/component mode synthesis approach," *Journal of Vibration and Control*, p. 1077546315604495, 2015.

[107] S. T. W. Kadawathagedara and D. J. Rixen, "Model reduction in co-rotated multi-body dynamics based on the dual craig-bampton method," 2011.

[108] S. Boer, R. Aarts, J. Meijaard, D. Brouwer, and J. Jonker, "A two-node superelement description for modelling of flexible complex-shared beam-like components," (Brussels, Belgium), Proceeding of ECCOMAS Multibody Dynamics, July 2011.

[109] R. Aarts and J. Jonker, "Dynamic simulation of planar flexible link manipulators using adaptive modal integration," *Multibody system dynamics*, vol. 7, no. 1, pp. 31–50, 2002.

[110] A. Cardona and M. Geradin, "A beam finite element non-linear theory with finite rotations," *International journal for numerical methods in engineering*, vol. 26, no. 11, pp. 2403–2438, 1988.

[111] O. Bruls, P. Duysinx, and J.-C. Golinval, "The global modal parameterization for non-linear model-order reduction in flexible multibody dynamics," *International journal for numerical methods in engineering*, vol. 69, no. 5, pp. 948–977, 2007.

[112] R. Hintz, "Analytical method in component modal synthesis," *AIAA Journal*, vol. 13, no. 8, pp. 1007–1016, 1975.

[113] D. Kammer and M. Triller, "Ranking the dynamic importance of fixed interface modes using a generalization of effective mass," *Modal Anal.*, vol. 9, no. 2, pp. 77–98, 1994.

[114] D. Kammer and M. Triller, "Selection of component modes for Craig-Bampton substructure representations," *J. Vib. Acoust.*, vol. 118, no. 2, pp. 264–270, 1996.

[115] D. Givoli, P. Barbone, and I. Patlashenko, "Which are the important modes of a subsystem?," *Int. J. Numer. Meth. Eng.*, vol. 59, no. 12, pp. 1657–1678, 2004.

[116] P. Barbone, D. Givoli, and I. Patlashenko, "Optimal modal reduction of vibrating substructures," *Int. J. Numer. Meth. Eng.*, vol. 57, no. 3, pp. 341–369, 2003.

[117] B. Liao, Z. Bai, and W. Gao, "The important modes of subsystems: A moment-matching approach," *Int. J. Numer. Meth. Eng.*, vol. 70, no. 3, pp. 1581–1597, 2007.

[118] I. Palomba, D. Richiedei, and A. Trevisani, "A ranking method for the selection of the interior modes of reduced order resonant system models," in *ASME 2014 12th Biennial Conference on Engineering Systems Design and Analysis, ESDA 2014*, vol. 2, 2014.

[119] I. Palomba, D. Richiedei, and A. Trevisani, "Energy-based optimal ranking of the interior modes for reduced-order models under periodic excitation," *Shock and Vibration*, vol. 2015, 2015.

[120] R. Belotti, I. Palomba, D. Richiedei, and A. Trevisani, "Interior mode selection in the craig bampton reduction technique based on an energy approach," in *6th International Operational Modal Analysis Conference, IOMAC 2015*, 2015.

[121] I. Palomba, D. Richiedei, and A. Trevisani, "Energy-based interior mode selection for reduced-order models under harmonic excitation," in *Proceedings of ISMA 2014 - International Conference on Noise and Vibration Engineering and USD 2014 - International Conference on Uncertainty in Structural Dynamics*, pp. 2577–2586, 2014.

[122] N. Liev and T. Waters, "Error location using normalized orthogonality," in *Proc. IMAC XII*, Genuary 1994.

[123] S. Kim, J. Lee, C. Yoo, J. Song, and S. Lee, "Design of highly uniform spool and bar horns for ultrasonic bonding," *IEEE Trans. Ultrason., Ferroelectr., Freq. Control*, vol. 58, no. 10, pp. 2194–2201, 2011.

[124] L. Hogben, *Handbook of linear algebra*. CRC Press, 2006.

[125] S. De Luca, *Linearizzazione di modelli dinamici per il controllo di meccanismi a membri deformabili. Master Thesis*. Università degli Studi di Padova, 2012.